An Experimental Study of Ingress Through Gas-Turbine Rim Seals

Hualca-Tigsilema, Fabian Patricio

Award date:
2020

Awarding institution:
University of Bath

An Experimental Study of Ingress Through Gas-Turbine Rim Seals

Fabian Patricio Hualca-Tigsilema

A thesis submitted for the degree of Doctor of Philosophy

University of Bath
Department of Mechanical Engineering
September 2019

Signature: 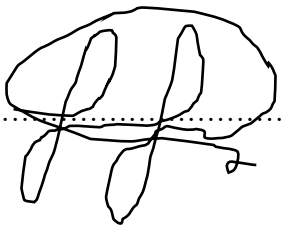

Abstract

The gas turbine has been widely used for mechanical drive, electric power generation and jet propulsion. Challenged by strict CO_2 emission regulations and competition between manufacturers, designers push the boundaries for an ever more efficient gas turbine. The cycle efficiency of the gas turbine is a crucial parameter that drives the engine performance and fuel burn. Improved cycle efficiency can be achieved by raising the turbine entry temperature, as well as the pressure ratio across the compressor. Today's gas turbine engines use bypass cooling air from the high-pressure compressor, to cool down the seal disc cavities and extend the life cycle of critical components in the stage. The cooling air (secondary system) can account for 25% of the total bypass air, approximately 5% of the total bypass air is used to seal the disc cavities. To further enhance the benefits of the sealing flow (cooling air), rim seals are fitted at the periphery of both, stationary and rotating discs. Rim seals help to further reduce the ingestion of hot mainstream gases (combustion chamber gases) that can cause damage to the discs and blade roots. The cause of hot gas ingestion is principally due to the circumferential pressure asymmetry in the mainstream flow, furthermore, the mixing between the sealing flow and mainstream gas, results in a deterioration of aerodynamic performance.

The first part of this thesis concerns experiments using a 1.5-stage turbine rig, from which the flow physics associated with ingestion could be studied. This thesis presents experimental results using the turbine test rig with wheel-spaces, upstream and downstream of a rotor disc. Ingress and egress were quantified using a CO_2 concentration probe. The probe measurements have identified an outer region in the wheel-space and showed a flow structure consistent with Batchelor-type flow. This is the first time asymmetric variations of concentration have been shown to penetrate through the seal clearance and the outer portion of the wheel-space. For a given flow coefficient in the annulus, the concentration profiles were invariant with rotational Reynolds number. The measurements reveal that egress flow provides a film-cooling benefit, on the vane and rotor platforms.

The second part of this thesis investigates the effects of ingress through a double radial rim seal. The effect of the vanes and blades on ingress was investigated by a series of carefully controlled experiments: firstly, the position of the vane relative to the rim seal was varied; secondly, the effect of the rotor blades was isolated using a disc with and without blades. Measurements of steady pressure in the annulus show a strong influence of the vane position. The relationship between sealing effectiveness and purge flow rate, exhibited a pronounced inflexion for intermediate levels of purge; an inflexion did not occur for the experiments with a bladeless rotor. Shifting the vane closer to the rim seal, and therefore the blade, caused a

local increase in ingress, at the inflexion region; again, this effect was not observed in the bladeless experiments. Unsteady pressure measurements revealed the existence of large-scale flow structures (flow instabilities) which depended weakly on the vane position but strongly on the sealing flow rate. Unsteady pressure was measured with and without the blades on the rotor disc. In all cases, the flow structures rotated close to the disc speed.

The third part of this thesis involves, experiments and computations of flow through a gas turbine chute seal. The study investigates ingress and the phenomena of flow instabilities. The aim of this study is to investigate the steady and unsteady flow features, near the rim seal mixing plane, for a geometrically scaled stage with a chute seal. The work presented here forms part of a future partnership with the KTH Royal Institute of Technology, to study the effect of engine scaling on ingress. Experiments and computations for; pressure, swirl and sealing effectiveness, were done at an engine representative turbulent flow (λ_T) condition. Under this condition, an engine representative wheel-space flow structure exists. CFD results suggest that flow instabilities influence ingress, instabilities caused by a shear interaction between the egress and mainstream. This supports the hypothesis of flow instabilities being driven by shear gradients.

The final part of this thesis investigates re-ingestion. A mixture of upstream egress flow and mainstream, gets re-ingested in the downstream wheel-space. Re-ingestion was experimentally measured and evaluated using a model developed by Prof. Mike Owen. To the author's knowledge, it is the first time this methodology has been applied to quantify re-ingested fluid in downstream wheel-space. The results showed that the upstream egress does not influence the fluid dynamics, downstream of the rotor blades. The experiments were conducted at incompressible flow conditions. Probe concentration measurements demonstrated that, an interaction occurs between the re-ingested fluid and the downstream egress flow, at the rim seal mixing region. Re-ingestion was evaluated for a range of sealing flow rates. It was shown that the mass fraction of re-ingestion increases with increasing downstream seeded sealing flow rate.

This Doctoral thesis is dedicated to my beloved mother who gave me the support to get this far and encouraged me to always aim for the stars…

…Thank you for giving me life, I love you mom.

Acknowledgements

Firstly, I would like to thank my lead supervisor Dr. Carl Sangan, for encouraging me and always keeping an optimistic attitude. Secondly, I would like to express my sincere gratitude to Professor. Gary Lock, for his creative approach to research, supervision and support.

A special thanks to my second supervisor Dr. James Scobie, who has pushed me to my limits, so I could become a better experimental research engineer, and who shared all his knowledge and knowhow experience on gas-turbines.

Finally, I would like to thank my colleagues and friends Dr. Marios Patinios and Dr. GeonHwan Cho, for their great advice and helping me from day one, and for being an absolute pleasure to work with.

Contents

List of Figures

List of Tables

Nomenclature

Symbols

a	speed of sound (m/s)
A_p	amplitude of unsteady pressure (Pa)
BPF	blade passing frequency (Hz)
b	radius of seal (m)
CFD	computational fluid dynamics
CFL	Courant–Friedrichs–Lewy
C	axial chord (m)
C_p	pressure coefficient (= A_p / $(0.5\ \rho\Omega^2 b^2)$)
$C_{p,s}$	static pressure coefficient (= $(p\text{-}p_{inf})/½\rho_{LE}\Omega^2 b^2$)
$C_{w,0}$	nondimensional sealing flow rate (= $\dot{m}/\mu b$)
c	concentration of tracer gas
$C_{d,e}$	discharge coefficient for egress
$C_{d,i}$	discharge coefficient for ingress
C_F	flow coefficient ($W/\Omega b$)
$C_{p,a}$	pressure coefficient in annulus (= $p_a\text{-}\bar{p}_a / ½\rho\Omega^2 b^2$)
$\tilde{c}$	mixed-out concentration
DLR	Deutsches Zentrum für Luft- und Raumfahrt
FFT	fast Fourier transform
f	measured frequency (Hz)
f_d	frequency of disk rotations (Hz)
G_c	seal-clearance ratio (= $s_{c,ax}/b$)
h	height of annulus (m)
LES	large eddy simulation
$\dot{m}$	mass flow rate (kg/s)

M Mach number

PCD pitch circle diameter

p static pressure (Pa)

p_T total pressure (Pa)

r radius (m)

Re_b blade Reynolds number ($= \rho W C_b/\mu$)

Re_v vane Reynolds number ($= \rho W C_v/\mu$)

Re_w axial Reynolds number in annulus based on radius ($= \rho W b/\mu$)

Re_ϕ rotational Reynolds number ($= \rho \Omega b^2/\mu$)

S axial clearance between rotor and stator (m), and Entropy (J/K)

s_c seal clearance (m)

SST shear stress transport

TET turbine entry temperature

TRACE Turbomachinery Research Aerodynamics Computational Environment

URANS unsteady Reynolds-averaged Navier–Stokes

V velocity relative to blades (m/s)

U bulk mean radial seal velocity ($= \dot{m}_0/2\pi\rho b s_c$)

V_ϕ tangential velocity (m/s)

W axial velocity in annulus (m/s)

z axial co-ordinate (m)

Γ_c ratio of discharge coefficients ($= C_{d,i}/C_{d,e}$)

$\Delta C_{p,a}$ pressure coefficient in annulus ($= \Delta p_a / \frac{1}{2}\rho\Omega^2 b^2$)

Δp_a peak-to-trough pressure difference in annulus ($= p_{a,max} - p_{a,min}$)

α angle between unsteady pressure transducers (rad)

β swirl ratio ($= V_\phi/(\Omega r)$)

Δt_α time for large scale structure to move through angle α (s)

λ_T	turbulent flow parameter (= $C_{w,0}\mathrm{Re}_\phi^{-0.8}$)
Ω	angular speed of rotating disc (rad/s)
Θ_0	sealing flow ratio (= Φ_0/Φ_{min})
Θ_e	egress flow ratio (= Φ_e/Φ_{min})
Θ_i	ingress flow ratio (= Φ_i/Φ_{min})
μ	dynamic viscosity (kg/ms)
ρ	density (kg/m^3)
Φ_0	non-dimensional sealing parameter (= $U/\Omega b$)
Φ_e	non-dimensional egress parameter
Φ_i	non-dimensional ingress parameter
Φ_{min}	minimum value of Φ_0 to seal wheel-space
x_1	axial distance from vane trailing edge (mm)
x_2	axial distance from rim seal leading edge (mm)
α_2	vane exit angle (deg)
β_2	relative blade inlet angle (deg)
β_3	relative blade exit angle (deg)
ε	effectiveness
ε_c	concentration effectiveness
θ	non-dimensional vane pitch
Λ	degree of reaction
ψ	blade loading coefficient
ω	angular speed of large scale structures (rad/s)
χ	re-ingestion mass fraction

Subscripts

a	annulus
ax	axial
A	value for axial-clearance seal
b	blade
d	downstream
e	egress
inf	infinite
i	ingress
LE	leading edge
min	minimum
0	sealing flow
R	value for radial-clearance seal
rad	radial
ref	reference
s	stator wall
u	upstream
v	vane

Superscripts

*	value for upstream-unseeded case
′	value re-ingested

Chapter 1: Introduction

1.1 A Brief History of Industrial Gas Turbines

The gas turbine engine is regarded as one of the most important technologies, in the power generation industry. Applications for the gas turbine range from: aero-engines, ships and power plants. The fundamental principle of the gas turbine is simple and can be described as, the conversion of thermal energy from a combustion gas into mechanical energy. In the early 1900s, the industrial gas turbine became vastly attractive to many engineers and entrepreneurs, due to its great capabilities, high power-to-weight ratio, simple configuration and operating mechanisms.

From 1913 to 1928, Hans Holzwarth developed the first experimental gas turbine to test out its advantages. Then the company Brown Boveri, directed by Hans Holzwarth, updated the experimental turbine to build the first industrial gas turbine engine (Meyer (1939)). Although the updated engine did not have compressor stages, it produced a reasonable power output of 200 HP. Further upgrades and improvements made by Brown Boveri, lead to the final version of the engine, and in 1933 it was installed in a German steel plant (Figure 1.1)

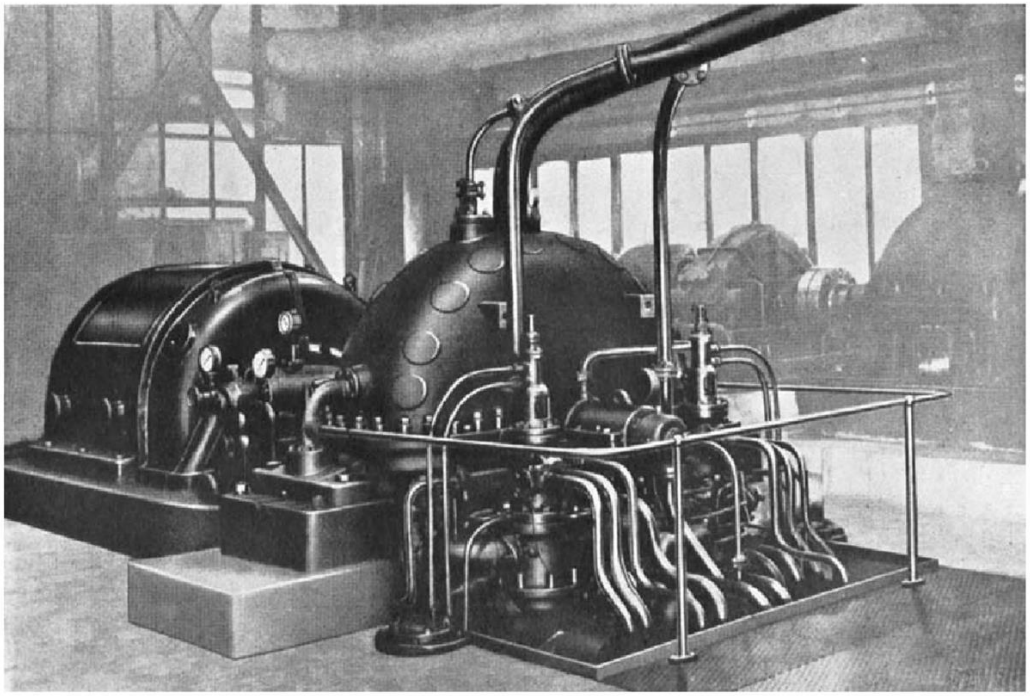

Figure 1-1: The first Holzwarth industrial gas turbine engine, Meyer (1939)

In 1937, Dr. Adolf Meyer was appointed as the new director of the Swiss company, Brown Boveri & Cie (BBC), and introduced the first commercial gas turbine for electrical power generation, in 1939. The first gas turbine was commercialised in Neuchâtel, Switzerland, and is now known as the Neuchâtel gas turbine. It produced a power output of 4 MW, making it the first turbine to exhibit engine characteristics of today's modern gas turbines (Figure 1-2). It operated at a TET (Turbine Inlet Temperature) of 550°C (823 K) and had a thermal cycle efficiency of 17.4%. The Neuchâtel engine comprised three fundamental components, an axial compressor connected to an axial turbine by a principal shaft, and a single combustion chamber placed in between the two. Other assisting components included a starting motor and a power generator.

This magnificent gas turbine remained functional for more than 60 years, producing useful energy until 2002. In 2002 a damaged generator unit found in the engine pushed it to the end of its life, and due to financial reasons, the Neuchâtel industrial gas turbine was withdrawn from service. The fundamental components and design arrangement used in the Neuchâtel engine can still be found in today's modern gas turbines. This concept was so revolutionary that in 1988, the American Society of Mechanical Engineers (ASME), made it a global mechanical engineering landmark. The Neuchâtel gas turbine engine now rests in Birr, Switzerland, where the Anglo-French company ALSTOM built a home for it (Figure 1-2). The Neuchâtel gas turbine is now owed by GE (General Electric).

Figure 1-2: Neuchâtel gas turbine engine in its resting place (Alstom (2007)).

Nowadays, the industrial gas turbine has become a common selection for the generation of high-power output. It is an efficient and reliable source of electrical power for many industries. The high power output and cycle efficiency of the industrial gas turbine provides several advantages in comparison to other power generating turbines, however, this huge achievement required tremendous contributions and effort from the engineering community, man-hours and

investors. These contributions made significant scientific and engineering breakthroughs possible. The evolution of the gas turbine is well documented. A timeline graph is provided in Figure 1-3, demonstrating the electrical power output evolution and the maturity of gas turbine technology. The electrical power output is the result of energy conversion, from mechanical energy to electrical energy, by means of a generator.

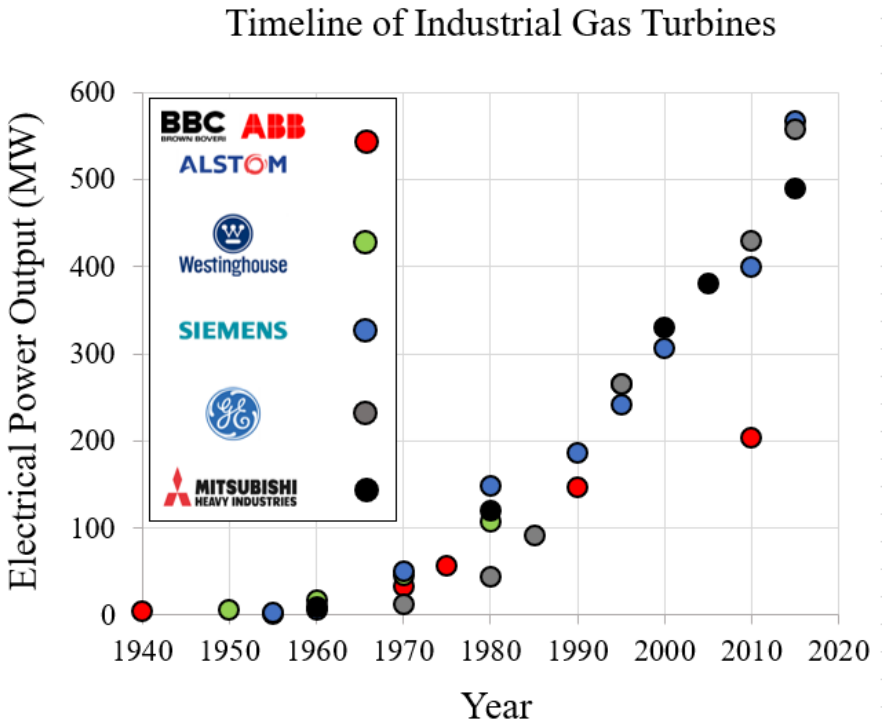

Figure 1-3: Variant of power output with time, for major gas turbine manufacturers.

In contrast to a steam turbine, the gas turbine doesn't need a huge source of water supply, it can reach full load operation faster and possesses a high power-to-weight ratio. From 1980 to 2010 the increase in electrical power output has risen exponentially, which was no coincidence. It was in the early 1980s that a huge amount of research was performed on materials and cooling systems for gas turbines. This led to higher turbine entry temperatures and consequently higher cycle efficiency. However, elevated temperatures can cause severe thermal damage to the turbine stage, hence cooling systems are needed. Astonishingly over the last decade, Siemens, GE and Mitsubishi Heavy Industries, have dominated the gas turbine market. Specifications for the latest gas turbines can be found in Figure 1-4.

(a)

Company:	Siemens
Model:	SGT5-9000HL
Simple Power Output:	567 MW
Combined Cycle Efficiency	65%

(b)

Company:	General Electric
Model:	9HA.02
Simple Power Output:	557 MW
Combined Cycle Efficiency	64%

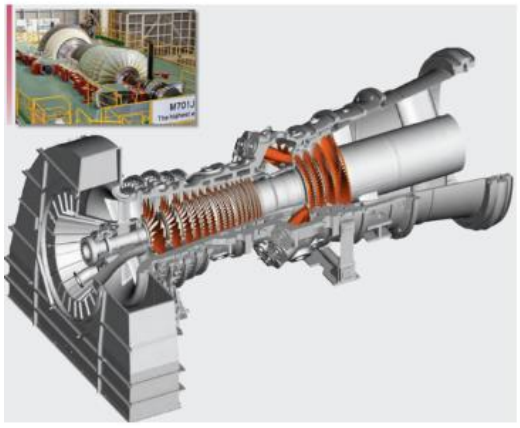

(c)

	Mitsubishi Heavy Industries
Model:	M501J
Simple Power Output:	490 MW
Combined Cycle Efficiency	64%

Figure 1-4: Data for current Industrial gas turbines, the latest engines include: Siemens SGT5-9000HL (a), GE 9HA-02 (b), Mitsubishi Heavy Industries M501J (c).

Figure 1-4 demonstrates the size and complexity of these engines. With almost identical combined cycle efficiency and similar simple power output, there are not many technical differences between these three gas turbines. Siemens, GE and Mitsubishi Heavy Industries are competing head to head in the industrial gas turbine market. The question is, what will be the next generation of gas turbines and, more importantly, who will build it first?

1.2 Industries for the Gas Turbine

The gas turbine industry can be divided into three categories: air, land and sea. The marine gas turbine can be used in oil and gas platforms but also in marine propulsion (Figure 1-5). This type of gas turbine is typically used for pipeline pumping and compression applications. With a high-power density, it is light and small compared to land gas turbines. This facilitates transportation, handling and maintenance. The cycle efficiency for this type of gas turbine can range from 35% to 40%, but this depends on the type of engine and manufacturer. For oil and gas applications, efficiency is not a critical factor since crude fuel sources are usually abundant onsite. Critical factors for this industry are transportability, availability and endurance. During the late 60s, powerful and reliable marine propulsion was on demand. The Royal Navy decided that all their new warships would be gas turbine propelled. The Queen Elizabeth-class aircraft carrier was commissioned in 2014 and is powered by two Rolls-Royce Marine gas turbine generators and four Wartsila 38 diesel engines, with a power capacity of 36 MW and 46 MW, respectively.

Figure 1-5: Offshore oil and gas platform, Soares (2015).

The power generation industry is heavily assisted by the land gas turbine. This type of gas turbine is generally combined with a steam turbine, to produce maximum power. It is typically slightly more efficient than the sea gas turbine, but large and heavy, due to its size and complexity. Maintenance can be costly. This is an ideal engine when space and weight restrictions are not a problem. Power capacity ranges from 50 MW to 567 MW, with efficiencies of 40% to 64% , in a combined cycle. The national grid is assisted by base load power plants. They are utilised almost 100% of the time, to supply the never-ending demand for electrical power. With the introduction of tougher CO_2 emission regulations, the land gas turbine competes with coal and nuclear steam plants.

The aero gas turbine (Figure 1-6) is built to produce thrust, which mainly derives from the fan. Approximately 75% of the thrust is produced by the inlet fan and 25% by the core engine. This type of engine possesses a high thrust-to-weight ratio. It is transportable and small. Maintenance is relatively cheap compared to sea and land gas turbines, but operating life is low. Weight and fuel consumption are critical factors in the aviation industry. These factors dictate the design and manufacturing of the aero gas turbine. To reduce emissions, they generally run on premium fuels. This engine possesses the ability to start-up, shut down and handle thrust variations faster than any other gas turbine engine.

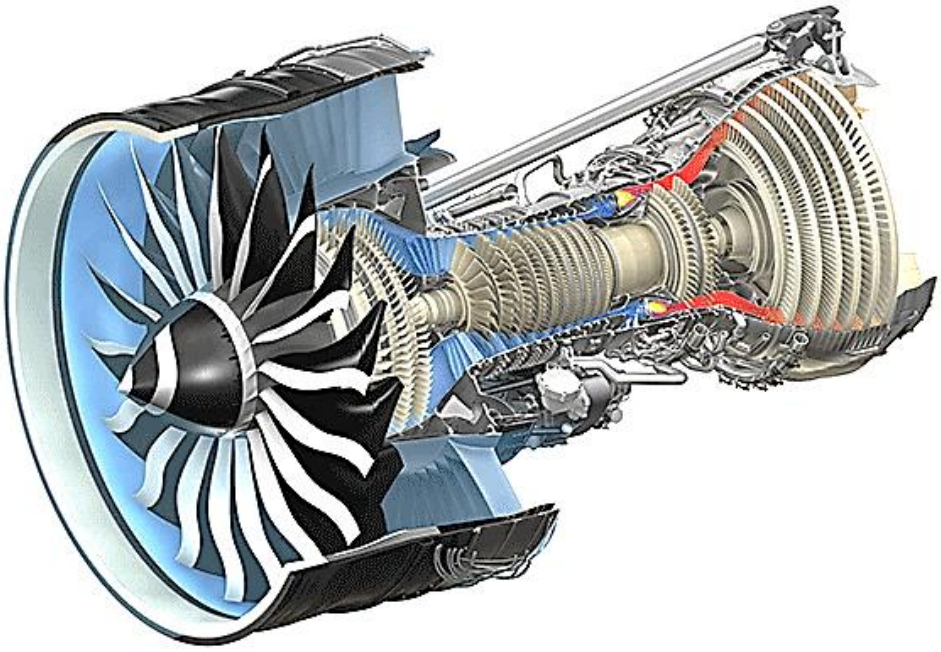

Figure 1-6: GEnx-1B turbofan engine Soares (2015).

1.3 Fundamentals of Industrial Gas Turbines

1.3.1 The Brayton Cycle for Gas Turbines

The gas turbine engine operates on a thermodynamic cycle that constantly draws ambient air into the compressor. The Brayton cycle can be used to describe the working principles of the gas turbine. The cycle begins with the compressor drawing in atmospheric air and ends with the turbine exhausting gas. The exhaust fumes generally exit at atmospheric pressure, but not atmospheric temperature. Consider the Brayton cycle shown in Figure 1-7, where *T* is temperature and *S* is entropy. Assuming there is no heat transfer to the surroundings, in the compression and expansion stage, the compression and expansion undergoes an adiabatic reversible process, therefore isentropic (solid black lines), from 1-2' and 3-4' respectively. A real gas turbine exhibits a non-isentropic process (generates entropy, *S*), this follows the compression and expansion stages, 1-2 and 3-4, respectively (dashed grey lines).

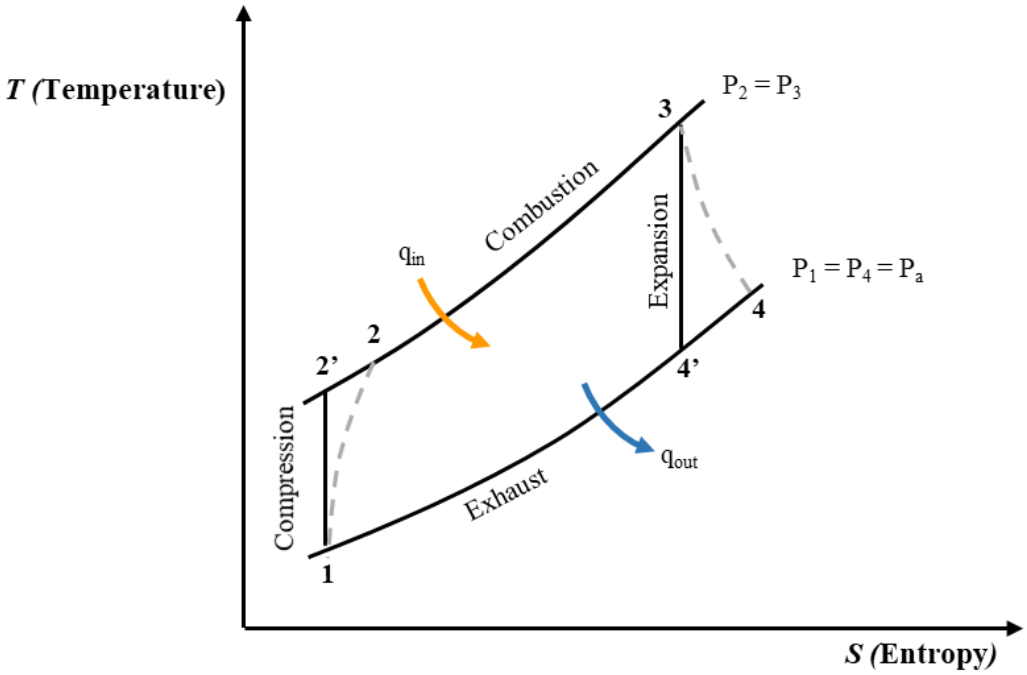

Figure 1-7: Brayton cycle, isentropic (solid black lines) and non-isentropic process (grey dashed lines).

The core components of a land gas turbine include: the compressor stages, the combustor and the turbine stages. This engine can be turned into an electrical power generating engine by adding an alternator. Consider Figure 1-8, at the entry to the compressor, temperature T_1 and pressure P_1 are both atmospheric. The compressor does work on the flow in an adiabatic

reversible process, and consequently increases the pressure and temperature to P_2 and T_2 without entropy changes. The flow then enters the combustor and undergoes a chemical reaction that increases the temperature to T_3, at constant pressure ($P_3 = P_2$) but with an increase in entropy. The chemical reaction adds energy to the flow, in the form of heat. In a real engine $P_3 < P_2$, however this change is relatively small and can be neglected. The hot flow then exits the combustor and enters the turbine. Across the high and low-pressure turbine, the hot gas expands adiabatically to conditions P_4, T_4 and P_5, T_5, respectively. The thermal energy from the hot gas is converted to mechanical, this drives the compressor stages and the alternator. The alternator then converts a portion of the mechanical energy into electrical energy, in the form of AC power.

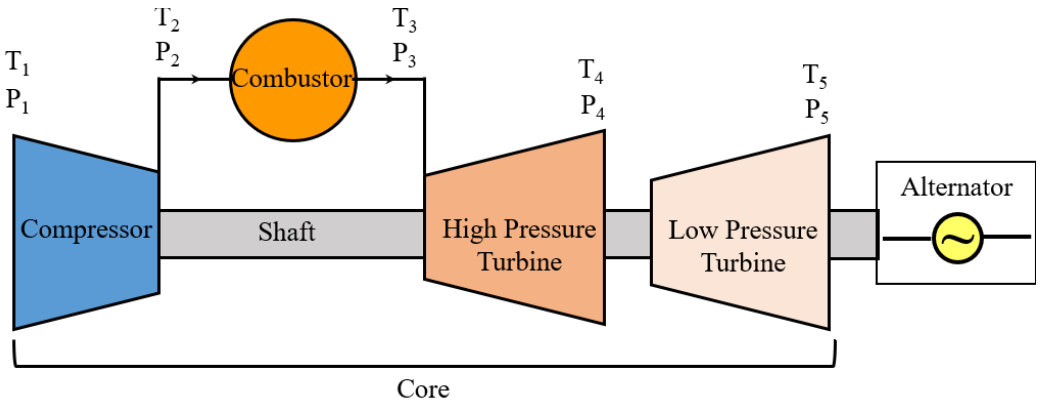

Figure 1-8: Gas turbine with an alternator to produce electricity.

The cycle efficiency of the gas turbine is a function of the pressure ratio, PR $=P_2/P_1$ and the temperature ratio, TR= T_3/T_1, for a non-isentropic process. For an ideal case (isentropic process), the cycle efficiency is just a function of the pressure ratio. For a realistic case (non-isentropic process), an increase in pressure ratio results in an increase in temperature ratio, consequently this produces a better cycle efficiency. However, the temperature ratio must be kept within the metallurgic limit of the turbine, to prevent it from melting. Over the last two decades, four companies have achieved significant breakthroughs in industrial gas turbine technology, Rolls-Royce, Siemens, GE and Mitsubishi Heavy Industries. These four companies have been pushing the boundaries on thermal efficiency by increasing the pressure and temperature ratio to limits where the engine could possibly melt!

1.4 Secondary Air System and Rim Seals

Modern gas turbines operate at elevated turbine entry temperatures, above the melting point of turbine components. A typical turbine stage comprises of nozzle guide vanes (stator discs), rotor blades (rotor discs) and wheel-spaces that exist between the stator and rotor discs. Upstream of the rotor disc is the upstream wheel-space and downstream of the rotor disc is the downstream wheel-space. Internal sealing flow (cooling air) is supplied to the wheel-spaces, to prevent ingestion of hot gas, and to thermally protect the rotor and stator discs. Hot gas ingestion occurs due to a pressure difference (pressure asymmetry) between the hot gas mainstream and the wheel-space. This pressure difference is caused by the presence of the nozzle guide vanes.

The wheel-space is an important feature of a turbine stage. Sealing (pressurising) this wheel-space is critical because, too little sealing flow or superfluous sealing flow, can both result in a negative impact. With no sealing flow, overheating and thermal loads occur, this puts the integrity and life cycle of the stage at risk. On the other hand, excessive use of sealing flow can diminish the thermal efficiency. Bleeding superfluous sealing flow results in less compressed air available for combustion, but also higher quantities of egress flow leaving the wheel-space. Egress flow is the mixture of ingested gas and sealing flow.

Hot gas ingestion can deteriorate the life cycle of the turbine discs and the efficiency of the engine, but recent studies now suggest that the interaction of egress and mainstream (annulus flow) also contributes to ingestion and secondary losses. Researchers have concluded that hot gas ingestion occurs due to the presence of the nozzle guide vanes, however, new research suggests that Kelvin Helmholtz instabilities also play a role. Kelvin Helmholtz instabilities are caused by the tangential shear between the annulus and egress flow leaving the wheel-space, consequently large-scale structures form.

For illustration purposes only, a section of the S6001-B gas turbine, and a section of a rim seal from a different engine has been combined to highlight a typical gas turbine rim seal, Figure 1-9 (a-b). The annulus flow is illustrated in orange and the flow-path of cooling air in white arrows. The supply of cooling air usually originates from the high-pressure compressor (HPC). This cooling (or sealing) air is called the secondary air system (SAS). There are two common methods of tackling the ingestion problem; one is to use a secondary air system, and another is to use a rim seal, to further reduce the degree of hot gas ingestion.

Hot gas ingestion is one of the most important problems of the secondary air system. Nowadays, complex 3D unsteady CFD codes are commonly used to address this problem. However, the CFD needs to be validated by experimental data. There is no doubt that CFD

and experimental research will continue to work in parallel for many years to come, to address the problem of hot gas ingestion.

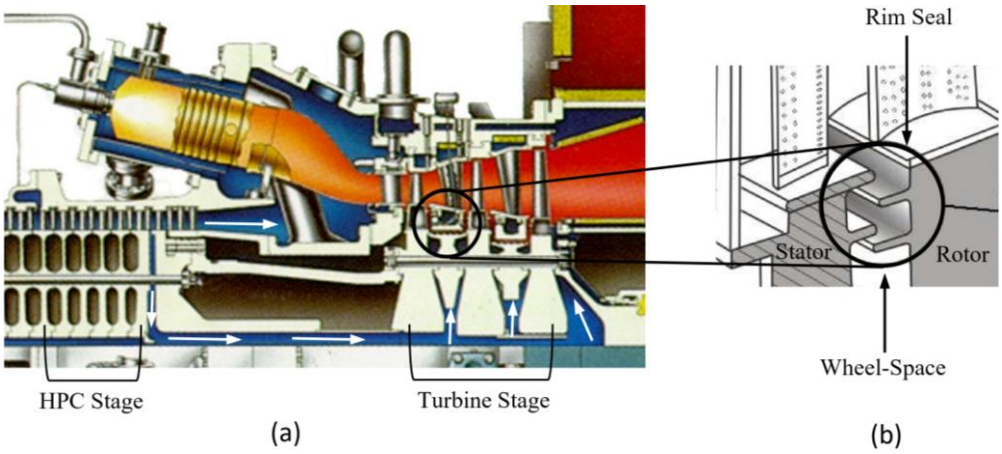

Figure 1-9: Secondary air system flow path of the S6001-B gas turbine (a), courtesy of GE, and a detailed section of typical gas turbine rim seal (b), by Sangan *et al.*(2012)

1.5 Flow Structure in the Upstream and Downstream Wheel-Spaces

The flow structure for a 1.5-stage configuration is illustrated by Figure 1-10. For upstream and downstream wheel-spaces, separate boundary layers are formed on the surface of the stationary and rotating discs, originating at $r = a$. In both upstream and downstream wheel-spaces there is radial outward flow in the rotor boundary layer and an inward flow in the stator boundary layer. The central core between the boundary layers in both the upstream and the downstream wheel-spaces acts as a medium for fluid to move axially from the stator to the rotor boundary layer. Sealing air is introduced to the wheel-spaces through an inner region. The sealing air gets pumped up the rotor and into the outer region; some fluid flows back to the stator boundary layer and the remainder leaves through the seal clearance. The flow structure in the downstream wheel-space shown in Figure 1-10 is virtually a mirror-image of the upstream wheel-space, with the only difference being that the egress flow must cross-over the ingress curtain first before flowing out into the mainstream. Figure 1-10 also shows re-ingestion occurring in the downstream wheel-space. The egress from the upstream wheel-space exits through the rim seal and propagates through the rotor blade passage. After entering the blade passage the egress splits with a proportion being entrained into the passage vortex (Langston (2001)) and diffusing radially in the annulus, and the rest being re-ingested as ingress into the downstream wheel-space. The theory behind the flow structure will be expanded in the literature section (Chapter 2).

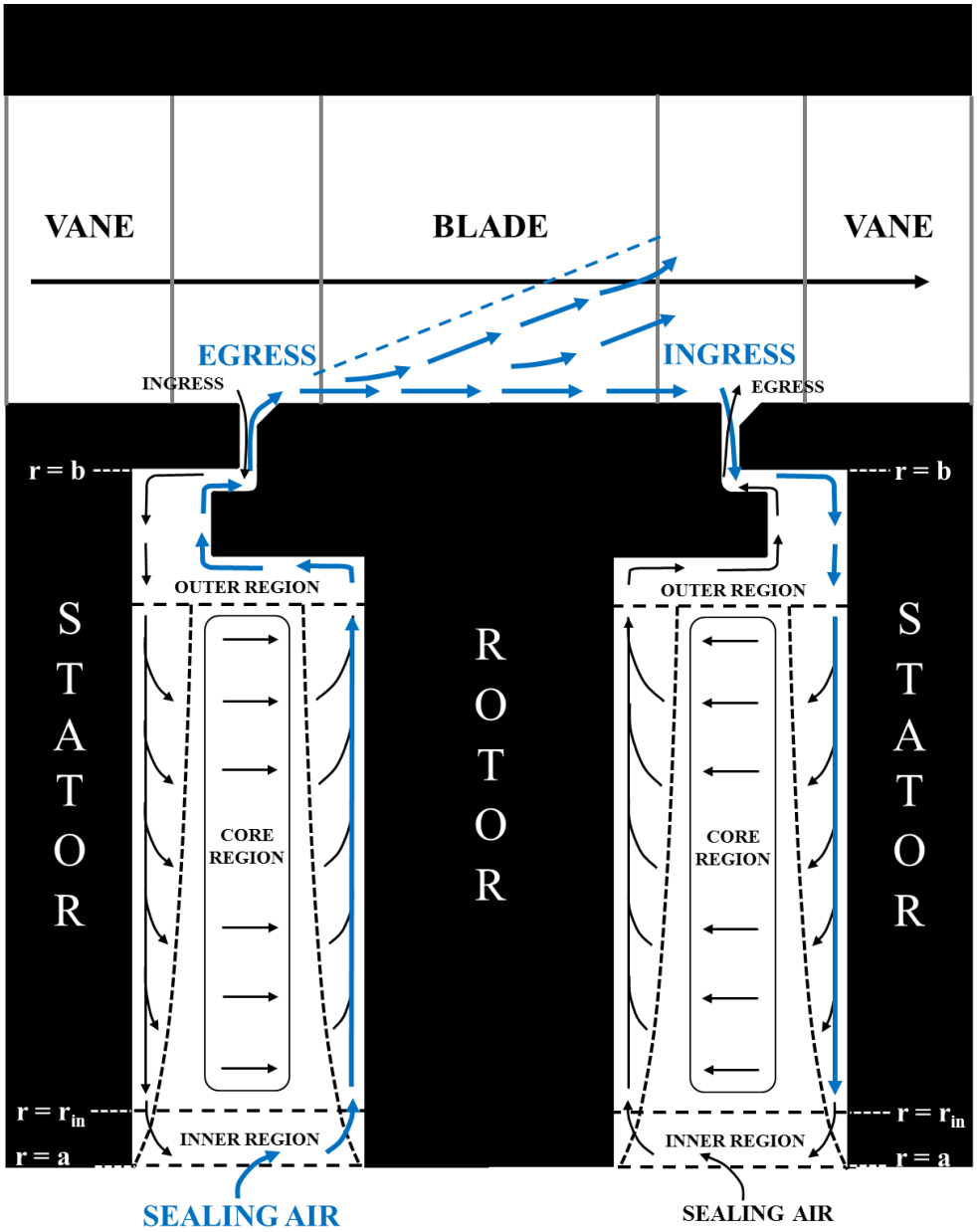

Figure 1-10: Silhouette of a 1.5-stage turbine with ingress, egress and re-ingestion (blue arrows) and an illustration the flow structure in the upstream and downstream wheel-spaces (Scobie *et al*, 2017)

1.6 Thesis Outline

A brief introduction on industrial gas turbines is provided in Chapter 1, emphasising the evolution of the gas turbine and its efficacy. Industry applications for the gas turbine are compared and discussed. The fundamental theory of gas turbines is explained, focusing on realistic working principles that include entropy. Major components of the gas turbine are described, and the hot gas ingestion problem is introduced, along with methods on how to tackle this problem. Lastly a list of conference and journal publications are provided.

Chapter 2 includes a detailed literature review related to the fundamentals of rotor-stator systems, hot gas ingestion and Kelvin-Helmholtz instabilities. The chapter concludes with a summary of the literature review and gap in the research, as well as the aim and objectives of this thesis.

Chapter 3 describes the operating capabilities of a new 1.5-stage turbine rig and its instrumentation. The 1.5-stage turbine rig is an experimental facility that was designed, built and commissioned at the University of Bath. This chapter also provides uncertainty analysis of the important experimental parameters.

Chapter 4 discusses the experimental results of the interaction between annulus and egress flow. CO_2 concentration and pressure measurements were taken in the upstream and downstream wheel-spaces for a single radial-clearance rim seal. Furthermore, the Bath orifice model is applied and discussed.

Chapter 5 discusses experiments conducted to investigate the effect of blades and vanes on hot gas ingestion. CO_2 concentration, steady and unsteady pressure measurements were taken in the upstream wheel-space for a double radial-clearance rim seal. Fast Fourier Transforms and spectral analysis were applied, to identify distinct frequencies related to large-scale structures (Kelvin-Helmholtz instabilities).

Chapter 6 provides experimental results for an engine-realistic stage with a chute seal. The rotor disc geometry is based on a Siemens engine. The experiments were conducted with a geometrically scaled stage, at relatively low Reynolds numbers but with an engine representative wheel-space flow structure. CO_2 concentration, steady and unsteady pressure measurements were taken in the upstream wheel-space for a double radial-clearance rim seal. Distinct frequencies not related to the blade passing frequency are scrutinised and discussed.

Chapter 7 presents unique findings on re-ingestion and discusses the potential cooling benefits re-ingestion could have on the downstream turbine stages. Gas concentration measurements were made, with seeded and unseeded upstream and downstream sealing flows. Probe measurements were taken across the annulus and through the seal clearance. A

theoretical model was developed (by Prof. Mike Owen) to evaluate the mass fraction of the re-ingested fluid.

Chapter 8 concludes the findings of this research and discusses how the results can benefit the gas turbine industry and engine designers. This chapter also suggests future experimental investigations that could lead to a better understanding of the hot gas ingestion problem in rotor-stator systems.

1.7 Publications

Over the course of this thesis the author has contributed to produce five ASME Turbo Expo conference papers [1, 2, 3, 4 and 5], and was lead author in one of them [4]. All of which were accepted and archived in the ASME Journal of Engineering for Gas Turbines and Power journal papers. In the first and second paper [1,2] the author conducted all the experiments, made the results figures and wrote the introduction and conclusions. For the third and fifth paper [3,5] the author conducted all the experiments, produced the results figures and wrote the discussion and conclusions. The fourth paper [4] was independently produced and written by the author.

Journal publications:

[1] Scobie, J., Hualca Tigsilema, F. P., Sangan, C., & Lock, G. (2017). Egress Interaction through Turbine Rim Seals. *Journal of Engineering for Gas Turbines and Power: Transactions of the ASME*, *140*(7), [072504].

[2] Scobie, J., Hualca Tigsilema, F. P., Patinios, M., Sangan, C., Owen, J., & Lock, G. (2017). Re-Ingestion of Upstream Egress in a 1.5-Stage Gas Turbine Rig. *Journal of Engineering for Gas Turbines and Power: Transactions of the ASME*, *140*(7), [072507].

[3] Horwood, J., Hualca Tigsilema, F. P., Scobie, J., Wilson, M., Sangan, C., & Lock, G. (2019). Experimental and Computational Investigation of Flow Instabilities in Turbine Rim Seals. *Journal of Engineering for Gas Turbines and Power: Transactions of the ASME*, *141*(1), [011028].

[4] Hualca Tigsilema, F. P., Horwood, J., Sangan, C., Lock, G., & Scobie, J. (2019). The Effect of Vanes and Blades on Ingress in Gas Turbines. In *Proceedings of ASME Turbo Expo, 2019.* GT2019-90987. *To appear in Journal of Engineering for Gas Turbines and Power: Transactions of the ASME 2020.*

[5] Horwood, J., Hualca Tigsilema, F. P., Wilson, M., Scobie, J., Sangan, C., Lock, G., Dahlqvist, J., & Fridh. J. (2019). Flow instabilities in Gas Turbine Chute Seals. In *Proceedings of ASME Turbo Expo, 2019.* GT2019-90982. *To appear in Journal of Engineering for Gas Turbines and Power: Transactions of the ASME 2020.*

Chapter 2: Literature Review

This chapter provides a detailed literature review regarding ingress into the wheel-spaces of rotor–stator systems, especially in gas turbine rigs. The first part of this chapter reviews the fundamental concepts of rotating flows, starting with free disc theory and rotor-stator systems. The second part of this chapter provides a review of experimental, computational and numerical research, focusing on EI (Externally-Induced) ingress, the dominant driving mechanism for ingress, in realistic gas turbine engines. Externally-induced ingress is primarily driven by the unsteady 3-D variation in pressure, created by the nozzle guide vanes and blades. The last part of this chapter summarises the literature review, identifies of the gap in the research and provides the aim and objectives that will address the gap in literature.

2.1 Free Disc Theory

To understand the complex flow interaction that occurs inside a rotor-stator system, it is important to first consider the fundamentals of a simple disc spinning in free air. Consider the disc is of radius *b*, spinning with constant angular velocity Ω and tangential velocity $V_\phi = \Omega r$, (Figure 2-1). As the disk spins, boundary layers form on both sides of the disk with zero tangential velocity (V_ϕ) at the free stream outside the boundary layers, and maximum tangential velocity at the surface of the disc, (Childs (2011)). The disc-pumping effect occurs due to the centrifugal forces acting on the fluid; this effect causes the flow inside the boundary layers to flow radially outward with velocity, V_r, to satisfy conservation of mass, surrounding fluid is entrained axially into the boundary layers, with velocity, V_z, this facilitates a continuous radial fluid flow. A study performed by Gregory *et al.* (1955), with a 15cm disc that rotated at 3200 RPM, found that the flow in the boundary layers transition to fully turbulent once it exceeds the critical rotational Reynolds number, , $Re_{\Phi,\,critical} \approx 2.8 \times 10^5$ (Schlichting (1955)). The flow state inside the boundary layer can be laminar or transition to turbulent, and is dependent on the rotational Reynolds number, Re_Φ, as shown by Equation 2.1, where ρ, Ω, r and μ are the density of air, rotational speed, local radius of disc and viscosity of air, respectively. The fluid is usually laminar near the rotation axis but can transition to fully turbulent for large values of Ω and radii (r).

$$\mathbf{Re_\Phi} = \frac{\boldsymbol{\rho \Omega r^2}}{\boldsymbol{\mu}} \qquad \textbf{Equation 2-1}$$

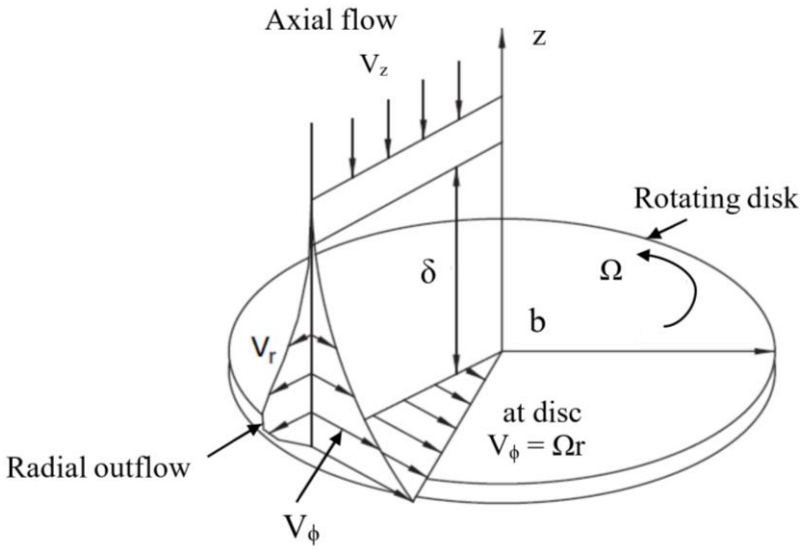

Figure 2-1: Velocity profiles of a simple disc, spinning in free air (adapted from Childs (2011))

2.2 A Stationary Disc in a Rotating Fluid

Having understood the fundamental flow physics related with the free disc case, it is now important to understand the fluid dynamics of a stationary disc with rotating air. Velocity profiles for this case can be found in Figure 2-2. Consider air rotating with tangential velocity, V_ϕ, at the free stream the tangential velocity is maximum, and minimum at the surface of the disc. From the centre of the rotating flow, the angular velocity varies outwards and since at the surface of the disc the angular velocity is zero, a radial pressure gradient is formed. The radial pressure gradient encourages the surrounding fluid to penetrate the boundary layer and flow radially inward towards the centre axis of the disc. In this case the flow moves radially inwards (opposite to the disc pumping effect), therefore flow builds up at the centre of the disc and in order to conserve continuity, air flows axially with velocity, (V_z), perpendicular to the surface of the stationary disc and into the mainstream. Consequentially, the angular momentum of the inward flow encourages the tangential velocity to be fractionally higher than the free-stream rotational speed, with a boundary layer thickness of, $z^* = 1.5\delta$, (Childs (2011)).

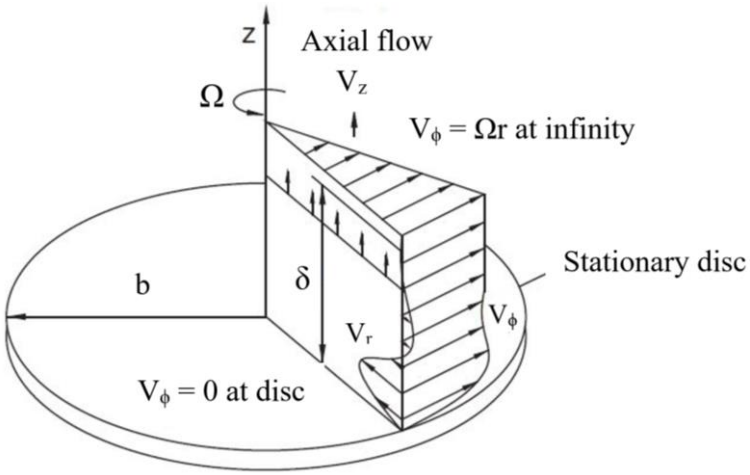

Figure 2-2: Velocity profiles of a stationary disc adjacent to a rotating fluid (adapted from Childs (2011))

2.2.1 Flow in a Rotor–Stator System

A rotor-stator system consists of stationary and rotating disc, with a wheel-space formed in between. Figure 2-3 demonstrates a typical configuration of a rotor-stator system. The configuration is a combination of the 'free disc' and 'stationary disc' cases, however, when the two simple cases are combined the fluid mechanics change. Consider the rotor and stator discs in Figure 2-3. The discs have radius, *b*, and are separated by an axial distance, *S*, which forms the wheel-space. At the periphery of the discs there are shrouds that create an axial clearance, $S_{c,ax}$. In a rotor-stator system, the fluid mechanics and flow structure are affected by shroud geometry, wheel-space aspect ratio and the addition of superposed flow.

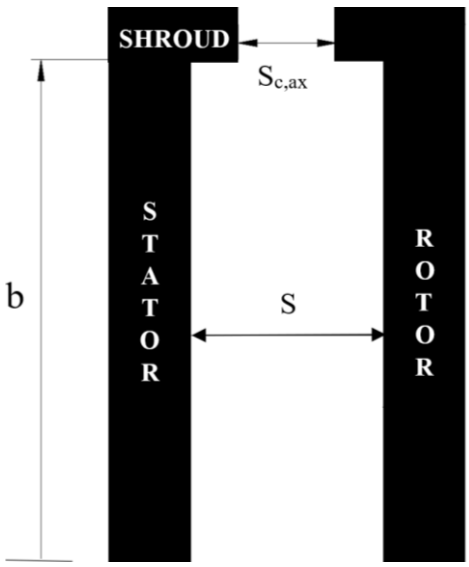

Figure 2-3: A silhouette of a generic rotor–stator system

In 1951, Batchelor conducted a rotating flow test, and proposed that the flow structure in a rotor-stator system (Figure 2-4), or wheel-space, consisted of an inviscid rotating core. The core fluid would rotate with angular velocity, V_ϕ, at a fraction of the disc speed. This flow behaviour indirectly suggested that Ekman boundary layers (Friedunder (1980)) would form on both the rotor and stator discs, separated an inviscid core of fluid. The core fluid acts as an intermediate for the conservation of mass, by entraining fluid; from the stator disc boundary layer to the core fluid, and from the core fluid to the rotor disc boundary layer (Figure 2-4).

The flow structure in the wheel-space forms when the rotor spins and boundary layers form on the face of the rotor adjacent to the stator disc, the disc pumping-effect then initiates a flow that enters through the shroud lip and crosses into the boundary layer of the stator surface and moves radially inwards. In order to satisfy conservation of mass, the core supplies fluid to the rotor's boundary layer, the fluid then moves along the surface of the rotor and is pumped radially outwards. Figure 2-5 shows a schematic of Batchelor-type flow.

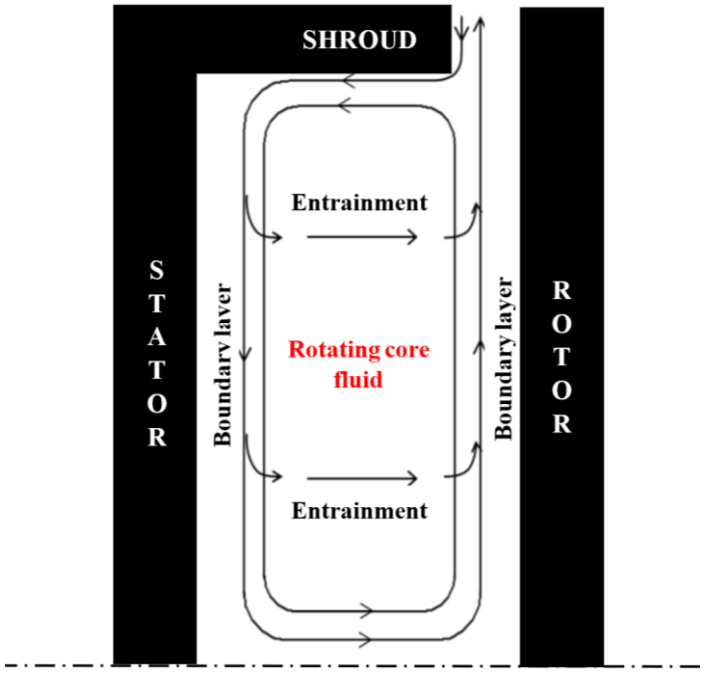

Figure 2-4: Flow structure of Batchelor-type flow in a rotor-stator system

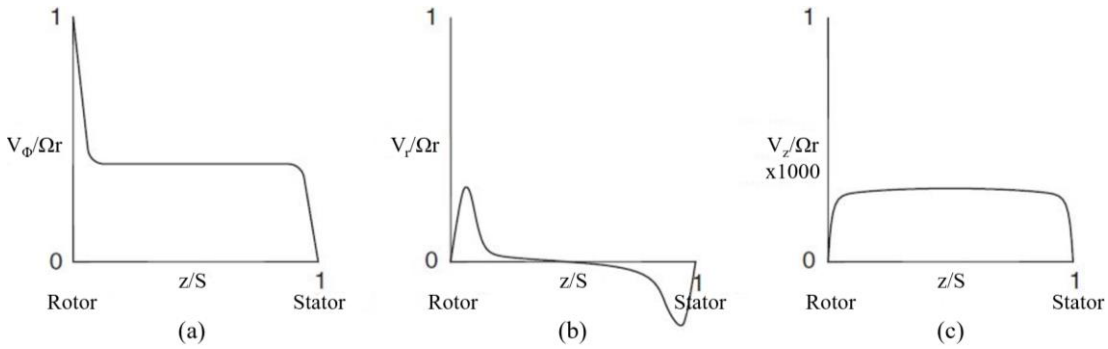

Figure 2-5: Batchelor-type flow, velocity profiles for a stator-rotor system: (a) tangential velocity, (b) radial velocity, and (c) axial velocity (Batchelor (1951))

A controversy arose in 1953, when Stewartson (1953) proposed a different flow structure, for the rotor-stator system. Stewartson (1953) conducted several computations and basic experiments that resulted in a contradiction to Batchelor's model. The results obtained by Stewartson suggested that, the tangential velocity component reduces from $V_\Phi = Or$ on the rotor disc surface, to $V_\Phi = 0$, at the stator disc surface. Figure 2-6 illustrates velocity profiles for Stewartson type flow.

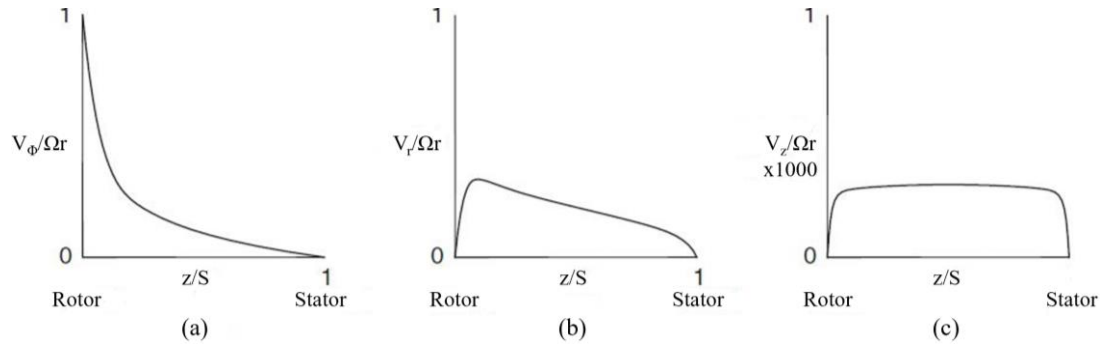

Figure 2-6: Stewardson type flow, velocity profiles for a rotor–stator system: (a) tangential velocity profile, (b) radial velocity profile, (c) axial velocity profile (adapted Stewartson (1953))

Pichai and Eckert (1958) demonstrated that a rotating core fluid did exist in a rotor-stator system, along with separate Ekman boundary layers. The rotor-stator system they tested had shrouds fitted at the periphery of both the stator and rotor discs. Further to Pecha and Eckert's research, Daily and Nece (1960) experimented on a rotor-stator system and carried out a theoretical study, that enabled them to categorise the rotor-stator flow structure into distinct regimes. Using the gap-ratio, G, as shown by Equation 2.2, and the rotational Reynolds number, Re_ϕ, as shown in Figure 2-7, four regimes were found. The gap-ratio, G, can be defined as,

$$G = \frac{S}{b}$$ **Equation 2-2**

where, S is the wheel-space gap, and b is the radius of the disc. The four regimes can be defined as follows:

- Regime 1: Narrow rotor-stator clearance, laminar flow with merged boundary layers (Couette flow) on both, stator and rotor disc.
- Regime 2: Large rotor-stator clearance, laminar flow with separated boundary layers and a rotating core in between.
- Regime 3: Small rotor-stator clearance, turbulent flow with merged boundary layers on both discs. Possesses natural similarities of regime 1.
- Regime 4: This regime involves a large rotor-stator clearance, turbulent flow with separated boundary layers, and a rotating core of inviscid fluid in between.

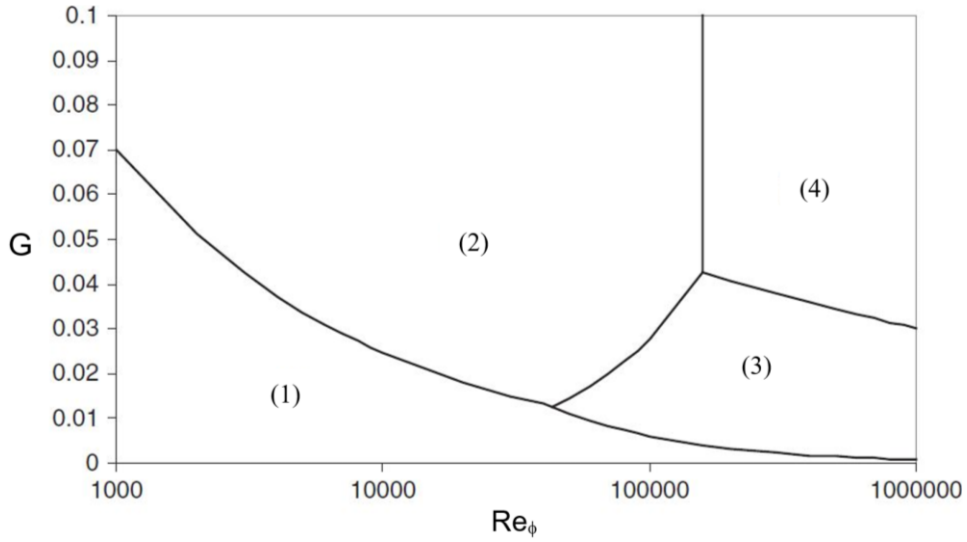

Figure 2-7: Proposed flow regimes for a rotor–stator system (Daily and Nece (1960))

Furthermore, Owen and Rogers (1989) conducted experiments in a rotor-stator system with superposed flow. It was found that there is a critical level of entrainment rate that if surpassed the rotating core will no longer hold its structure. The flow structure in the wheel-space can exhibit Batchelor type flow, in the absence or limited superposed flow, and based on the work of Owen (1988) it was found that a rotor-stator system with no sealing flow, or λ_T =0, produces a swirl value of β=0.43 in the core. However, an increase in superposed flow, above the critical level, would diminish the core rotation (hence $\beta \rightarrow 0$), transforming the flow structure from

Batchelor type flow to Stewartson type flow. Owen and Rogers (1989) evaluated the critical entrainment rate as $\lambda_{T,crit}$=0.22, where, λ_T is the turbulent flow parameter and is defined as:

$$\boldsymbol{\lambda_T = C_{w,0} Re_\phi^{-0.8}} \qquad \textbf{Equation 2-3}$$

where $C_{w,o}$ is the non-dimensional axial flow rate, and is defined as:

$$\boldsymbol{C_{w,0} = \frac{\dot{m}}{\mu b}} \qquad \textbf{Equation 2-4}$$

2.3 Ingress in Gas Turbines

In this section, a brief review on Rotationally-Induced ingress (RI ingress) is presented, followed by a comprehensive examination on Externally-Induced ingress (EI ingress), the dominant driver for ingress in real gas turbines. Ingress can be divided into three categories, RI ingress, EI ingress and combined ingress. In a gas turbine both RI and EI ingress mechanisms can occur simultaneously.

2.3.1 Rotationally Induced Ingress

Pioneering research on RI ingress began at University of Sussex, where, Bayley and Owen (1970) experimented on an air-cooled a rotor-stator stage. The addition of superposed flow to the wheel-space made RI ingress occur, the disc pumping effect created a pressure gradient, and this made the pressure in the wheel-space sub-atmospheric. To conserve mass, external fluid moved radially down into the wheel-space. Bayley and Owen noticed that an increase in superposed flow rate resulted in an increase in pressure in the wheel-space. As the pressure differential with respect to the gas path reduced, so did the level of ingestion. The authors developed a correlation to obtain the minimum superposed flow-rate, $C_{w,min}$, as shown by Equation 2.5, required to seal the system. The correlation was proportional to the seal clearance ratio, G_c, and rotational Reynolds number, Re_ϕ:

$$\boldsymbol{C_{w,min} = 0.61 G_c Re_\phi} \qquad \textbf{Equation 2-5}$$

Phadke and Owen (1983), conducted experiments, using radial-clearance rim seals. The results did not meet the authors expectations and showed that pressure in the wheel-space increased rather than decrease with increasing Re_ϕ. The authors called this behaviour the

'pressure-inversion effect'. Consequently, the pressure inversion effect resulted beneficial for $C_{w,min}$, and proved even more beneficial, in terms of seal performance, when a larger shroud overlap was used. The authors suggested that the free disc pumping effect was not the cause of the pressure-inversion effect and suggested further research to be done.

In 1988 three research papers regarding RI ingress were produced, Phadke and Owen (1988 a-c), that built on their previous work. Taking inspiration from Graber *et al.* (1987), the authors implemented CO_2 gas concentration measurements to their investigation, the results showed that the concentration in the core varied insignificantly in the axial direction. Furthermore, flow visualisation answered an unexplained ingress effect, the results demonstrated that the impingement of the radially pumped flow on the rotor platform created a film of air that acted as a protective curtain which in turn reduced ingress.

The work of Phadke and Owen (1983) was further examined by Chew (1991). The author had doubts over the results obtained for small seal clearances. Chew (1991) analysed the pressure difference across the seal and found that the discharge coefficients were greater than unity. The author attributed these errors to variation in the seal gap, G_c. The author then developed a simple orifice model and used it to evaluate $C_{w,min}$. Chew (1991) used the empirical constant, $k = 0.65$, from Phadke and Owen (1983), and the theory agreed, as well as with the results of Graber *et al.* (1987).

Chew (1992) extended the theory model of Chew (1991), by using experimental data from Daniels *et al.* (1992). Comparisons were made using seal geometries such as radial-clearance seals. These seals were tested under the influence of external flow by Dadkhah *et al.* (1992). The author recognised that the pressure of external flow in the annulus was important for modelling ingestion. A review of EI ingress is presented in the next section.

2.3.2 Externally-Induced Ingress

Abe *et al.* (1979) conducted the first study that identified ingress to be driven by the external flow rather than the rotational speed of the disc. The experimental test rig included a stator disc with vanes and a disc without blades . External (mainstream) flow was supplied to the stage in the absence of rotor blades. The authors found that testing in atmospheric conditions resulted in an underprediction of ingress. The findings encouraged the authors to conduct investigations into the effects of external flow. It was concluded that the rim-seal clearance, geometry of the rim-seal and the ratio of sealing to annulus flow were major factors that affected ingress.

Phadke and Owen (1988c) developed Abe's *et al*. (1979) work by investigating external flow through rim-seals. The results of this study showed $C_{w,min}$ to be proportional to Re_{ϕ}, for low mainstream flow rates, however, it was independent of Re_{ϕ}, for high mainstream flow rates. In addition for low flow coefficient values, C_F (see nomenclature), $C_{w,min}$ decreased with increasing Re_w, however high flow coefficient values $C_{w,min}$ become proportional to Re_w. The authors concluded that external effects were the dominant driver for ingestion.

In 1992, an experimental turbine rig was built at the university of Sussex (Dadkhah *et al*. (1992)). Two rim-seal configurations were tested, one in the upstream and one in the downstream wheel-space, as shown in Figure 2-8. The turbine stage comprised of shrouded discs but no vanes and blades in the annulus. The test rig could achieve a rotational Reynolds number of, $Re_{\phi} = 3 \times 10^6$. The flow was conditioned to achieve axisymmetric flow properties and be EI dominated for the purpose of the experiment.

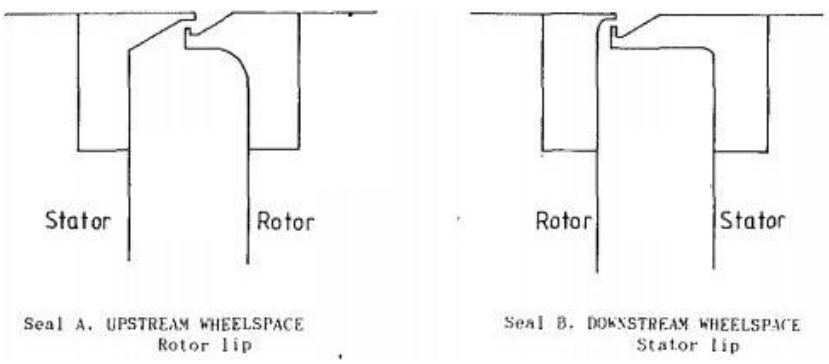

Figure 2-8: Rim-seals tested by Dadkhah *et al.* (1992)

Measurements of pressure and concentration were used to show that external flow mixes with sealing flow at a region near the rim-seal clearance before moving radially inwards down the stator. After fully mixing on the stator side, the flow moved axially into the rotating core towards the rotor side. In this study the authors noted for the first time that a cooling effect could exist, as the concentration near the rotor was higher than on the stator wall.

Chew *et al.* (1994) conducted an experimental and computational study of EI ingress through rim-seals. For the experimental phase of the study the authors added 18 stator vanes to the rig of Dadkhah *et al*. (1992). The effect of Re_w and vane axial position on the circumferential pressure was investigated. The experimental results showed that the amplitude of the circumferential pressure increased with Re_w and decreased with axial distance relative to the vane trailing edge. The authors concluded that ingress increased as the vane trailing edge gets closer to the upstream edge of the seal. The computations demonstrated encouraging

agreement with the experimental measurements and showed that the concentration on the rotor disc is much higher than the one on the stator disc and correlated with the findings of Dadkhah *et al*. (1992).

Green and Turner (1994) modified the Chew *et al.* (1994) rig, creating and a single turbine stage rig, to investigate ingestion of external flow. The new rig included engine representative features such as: an axial seal, a stator disc with vanes and a rotor disc with blades. Measurements of N_2O concentration conducted in the upstream wheel-space showed that, the addition of rotor blades reduced the level of ingress into the wheel-space. The authors suggested that the rotor blades weakened the pressure asymmetry in the annulus, resulting in reduced ingestion.

Bohn *et al.* (1995) used a new 1-stage turbine test rig to investigate ingress. The rig included a stator disc and a bladeless rotor, capable of reaching a maximum rotational Reynolds number of $Re_\phi = 2 \times 10^6$. Using Laser Doppler Velocimetry (LDV), velocity data were collected, inside the wheel-space. The data showed that at certain conditions ingress occurred on both the stator and rotor side of the wheel-space. Furthermore, annulus pressure measurements downstream of the vane trailing edge confirmed the axial decay of pressure identified by Chew *et al.* (1994).

Hills *et* al. (1997) conducted an experimental and a computational fluid dynamic (CFD) study on ingress, in an updated version of the test rig used by Dadkhah *et al*. (1992). The facility included 29 stator vanes and 16 rotor pegs. Computations and experiments demonstrated good agreement at low sealing flow rates, however, at high sealing flow rates there was significant disagreement between the results. The authors attributed the lack of agreement to the inability of the CFD to capture the strong interaction between the purge and external flows. It was concluded that more sophisticated CFD codes would be needed in future studies, capable of capturing complex flow interactions.

Bohn *et al.* (1999) experimented on a 1.5-stage turbine and conducted experiments to validate CFD data. The new test rig included 62 twisted rotor blades. Measurements of CO_2 concentration were conducted, and the effects of Re_w and Re_ϕ on the sealing effectiveness were analysed. The experimental results showed an increased pressure asymmetry increased with increasing Re_w which resulted in a reduction on sealing performance. The 3D CFD results showed that, without blades, large-scale structures formed near the rotating disc.

Bohn *et al.* (2000) contrasted their previous findings to results obtained without rotor blades. The authors found that, for a simple axial gap, the rotor blades have a significant effect on the pressure asymmetry downstream of the vane trailing edge, resulting in an adverse effect on sealing effectiveness. However, for a shrouded rim seal, the blades had a positive effect; and 3D unsteady CFD results confirmed this increase in sealing effectiveness.

Feiereisen *et al*. (2000) conducted experimental measurements to study the effects of rim cavity purge flow on the pressure and cooling effectiveness distributions near the rim cavity and on the rotor blade platform. The test rig comprised a full-scale, half-span, engine representative first stage. The authors found two unsteady structures linked to the eccentricity of the disc and 24-34 large-scale structures rotating at speeds below the disc speed.

Hills *et* al. (2002) extended the computations presented in Hills *et* al. (1997). The authors found that the pressure asymmetry in the rotor side was smaller compared to the one in the stator side. Furthermore, unsteadiness of pressure due to the rotor disc had a significant adverse effect on ingestion. This finding contradicts earlier conclusion of the work by Bohn *et al.* (2000).

Bohn *et al.* (2003) experimented on a 1.5-stage test rig. The external flow was heated to a temperature of 75^{o}C and the sealing flow was introduced at ambient conditions. unsteady velocity data in the upstream wheel-space were obtained using laser doppler velocimetry. The results suggested that the vanes and blades had a significant effect on ingress. The authors also investigated the effect of egress at high purge flow-rates finding that ingress occurred at regions of high pressure (near the rotor blades), even at high purge flow rates.

Gentilhomme *et al.* (2003) investigated ingress using a single axial-clearance seal. The test facility included a 1-stage test rig with 26 vanes and 59 twisted blades. Measurements of CO_2 and N_2O concentration were used to showed that the effectiveness increases with purge flow rate and is independent of Re_{Φ}. Some concentration curves exhibited inflexion points, but the authors did not provide an explanation. Furthermore, the authors used CFD to study the circumferential pressure asymmetry in the annulus. An improved orifice model was used to predict ingress although the model consistently underestimated ingress.

Jakoby *et al.* (2004) conducted a 3D unsteady CFD study to develop a reliable way of capturing the flow physics attributed to ingress. The results showed that the CFD disagreed with the experiments, for the radial distribution of pressure at low purge flow-rates. However, high purge flow-rates resulted in a better agreement between CFD and experimental data. In a second part of the study the authors conducted unsteady pressure measurements in the 1.5-stage rig Bohn *et al.* (2003) conducted his experiments, the unsteady data were presented in the form of FFTs, shown in Figure 2-9. For the low purge flow rate, the FFT results showed a distinct frequency of 406 Hz, significantly higher than the blade passing frequency, however, for the high purge flow rate this distinct frequency disappeared.

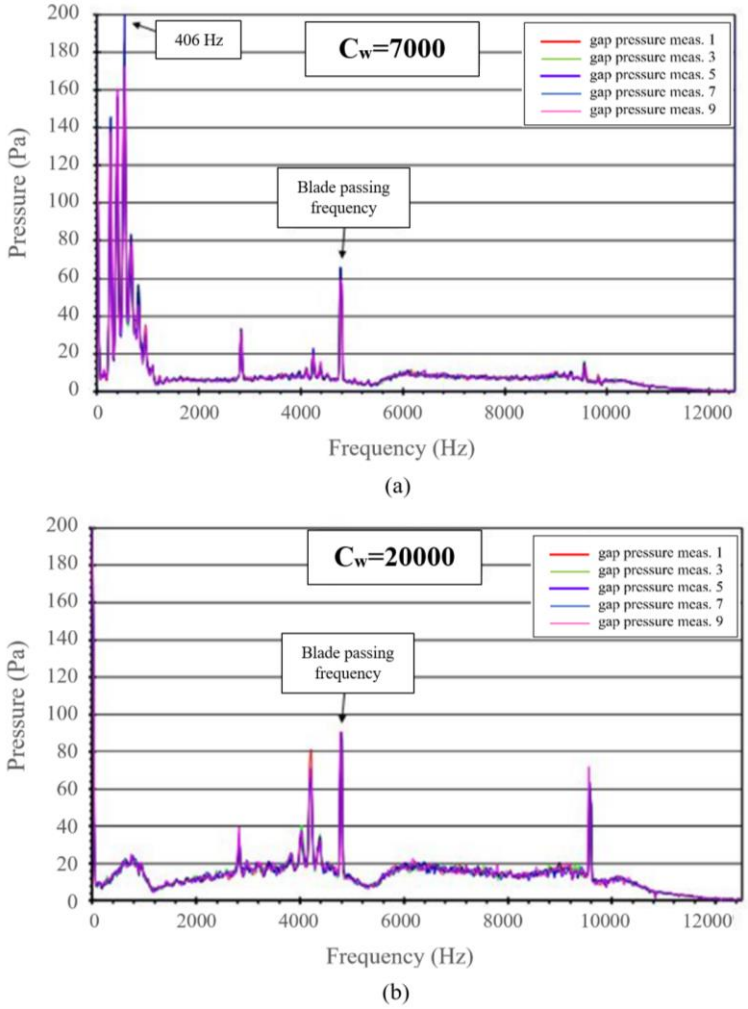

Figure 2-9: Unsteady pressure measurements in the upstream wheel-space at measurement locations 1, 3, 5, 7, for two sealing flow rates – (a) low sealing flow rate; (b) high sealing flow rate, at (Jakoby *et al*, 2004)

Roy *et al.* (2005) conducted unsteady pressure and CO_2 concentration measurements in the wheel-space of a modified test facility comprising of a stator disc with 22 vanes and a rotor disc with 28 blades. For two vane pitch locations, the results revealed that an unsteady blade-related component exists near the rim seal region and is highly sensitive to the amount of egress flow leaving the wheel-space. Furthermore, FFTs of the unsteady pressure data revealed distinct frequencies unrelated to the blade passing frequency, although it was noted that the blade passing frequency was dominant for all the cases. The authors suggested that the distinct frequencies were connected to large scale structures, similar to those found by Jakoby *et al.* (2004).

Boudet *et al.* (2005) conducted experiments and CFD computations in order to study the influence of flow instabilities, main annulus pressure asymmetries and rim seal geometry on sealing performance. The experimental results showed that, the unsteadiness near the rim seal

is dampened by the presence of mainstream flow. However, the CFD results showed that similar unsteady phenomena can occur at engine conditions and for different seal configurations. Furthermore, it was found that pressure asymmetries in the annulus, created by the interaction of vanes and blades, have a major influence on ingestion. CFD results for engine realistic conditions, showed that, the rotor blades significantly influenced the pressure field near the rim seal region, furthermore sealing effectiveness curves revealed inflexion points, similarly found by Gentilhomme *et al.* (2003), though the authors do not present an explanation for the cause of these inflexions.

A further study by Boudet *et al.* (2006), presented CFD results of unsteady flow for a 1-stage turbine rig, that included vanes, blades and a chute seal. The CFD results were compared with existing experimental data. The unsteady data results revealed a band of low magnitude frequencies not attributed to large scale structures and the blade passing frequency with a distinct peak. The authors concluded that a more sophisticated CFD model is needed, to fully capture the flow physics attributed to ingress.

Bohn *et al.* (2006) studied ingress using an axial and a radial clearance rim seal, in the upstream wheel-space of a 1.5-stage test rig. The experiments comprised of measurements of static pressure and CO_2 concentration. The authors found that, for both minimum and maximum levels ingress into the wheel-space, the radial-clearance rim seal performed significantly better than the axial-clearance rim seal.

Wang *et al*. (2007) performed CFD computations with the aim of generating insight regarding the physical mechanisms governing ingestion. Calculations were carried out for three seal and wheel-space configurations. The results revealed that the blade bow wave is the dominant driver for ingestion in all cases investigated. Figure 2-10 shows the different seal configurations tested. It was found that the ingestion rate for configuration C was approximately half that for configurations A and B. Radial contours of velocity revealed that ingress flowed radially inward down the stator wall. The authors concluded that the blade pressure field was responsible for influencing the rate of ingestion, rather than the vane pressure field.

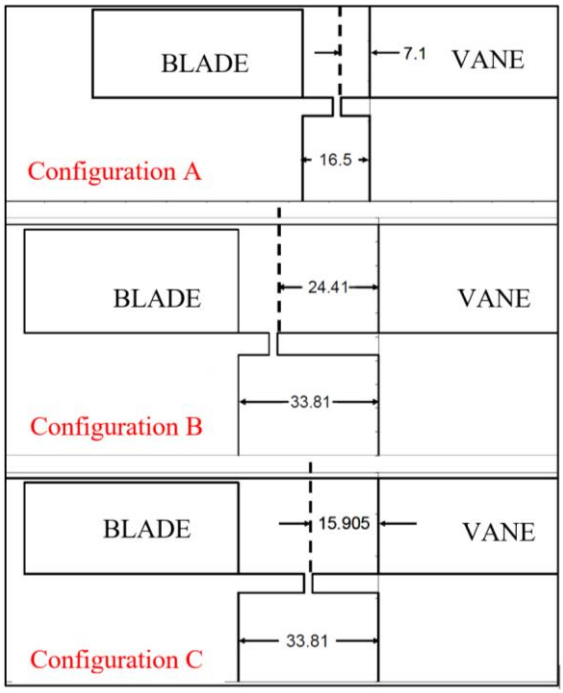

Figure 2-10: Seal and wheel-space configurations; note: all dimensions in mm (Wang *et al*, 2007)

Rabs *et al*. (2009) presented a paper regarding the development of Kelvin-Helmholtz instabilities in a 1.5-stage gas turbine rig based on the test facility at the Technical University of Aachen, that included vanes and blades. The results showed that for high purge flow rates Kelvin-Helmholtz Instabilities occurred near the rim seal region. For a simplified stage build, without vanes and blades, it was found that the development of Kelvin-Helmholtz instabilities is dependent on the magnitude of swirl in the annulus flow. For the engine representative stage, the authors found that high purge flow-rates produced more distinctive Kelvin-Helmholtz instabilities; these instabilities were suppressed by the presence of the vanes and the blades.

Zhou *et al*. (2010) made measurements of pressure, CO_2 concentration and velocity using Particle Image Velocimetry (PIV). The experiments were conducted in the Arizona State University rig, for three different rim-seal geometries, a single clearance radial seal and two double clearance radial seals. The authors found that the double clearance radial seals performed better than the single clearance radial seal. The PIV data revealed distinct circumferential regions of ingress and egress within the seal clearance. The authors concluded that the concentration and PIV results were in agreement with previously published data by Bohn *et al.* (2006).

Owen (2011a) developed an orifice model for the prediction of sealing effectiveness. Ingress and egress were assumed to cross an orifice ring through control volumes, δA_i and

δA_e, shown by Figure 2-11, and when added together they equalled the area of the seal clearance.

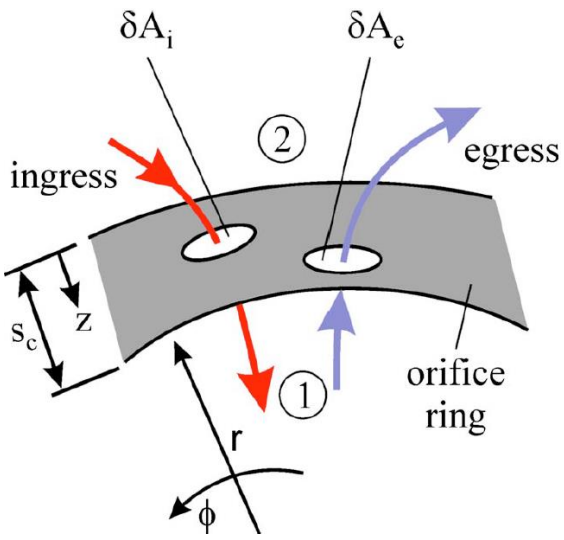

Figure 2-11: Orifice ring (Owen (2011a))

The three main assumptions of the model were continuity of mass and energy inside the separate stream tubes of ingress and egress, conservation of angular momentum so that free vortex occurs and of inviscid flow. Two discharge coefficients were used to approximate viscous losses; a discharge coefficient for egress, $C_{d,e}$, and a discharge coefficient for ingress, $C_{d,i}$. The author noted that $C_{d,e}$, and $C_{d,i}$ can only be empirically determined and can change for different seal geometries.

Owen (2011b) developed a theoretical model for EI ingress. A 'saw-tooth' model, was derived to approximate the circumferential peak-to-trough pressure distribution, ΔCp in the annulus; the driving potential for ingress. Owen *et al*. (2012) showed the saw-tooth model was able successfully approximate, ΔCp, using the pressure criterion. The orifice equations were solved analytically to obtain the minimum non-dimensional sealing flow parameter for EI, $\Phi_{min,EI}$, so that;

$$\boldsymbol{\Phi_{min,EI} = \frac{2}{3} C_{d,e} (\Delta C_p)^{\frac{1}{2}}} \qquad \textbf{Equation 2-6}$$

Eastwood *et al*. (2012) conducted experiments on a 2-stage turbine rig, at the university of Sussex. The author investigated purge and re-ingestion flows. A tracer gas technique was used to measure the rim seal and re-ingestion flows. Re-ingestion experiments showed that 7% of the egress leaving the upstream wheel-space gets re-ingested in the downstream wheel-space,

furthermore, it was found that the re-ingested flow reduced with increasing sealing flow in the upstream wheel-space.

Sangan *et al.* (2013) used the theoretical model by Owen (2011) and derived the equations to predict ingress, but as a function of effectiveness of concentration (ε) rather than pressure.

The non-dimensional sealing flow parameter can be equated as;

$$\boldsymbol{\Phi_0 = \frac{C_w}{2\pi G_c Re_\Phi} = \frac{U}{\Omega b}} \qquad \textbf{Equation 2-7}$$

Here Φ_0 is equivalent to a flow coefficient: the ratio of radial velocity, U, through the seal clearance to the rotational speed, Ω, of the disc. All other symbols are defined in the nomenclature. The sealing effectiveness (ε) can be defined in terms of the mass flow of ingress, egress and superposed sealing flow, $\dot{m}_i$, $\dot{m}_e$, and $\dot{m}_0$:

$$\boldsymbol{\varepsilon = 1 - \frac{\dot{m}_i}{\dot{m}_e} = \frac{\dot{m}_o}{\dot{m}_e}} \qquad \textbf{Equation 2-8}$$

An explicit relationship can be formed between Φ_0 and the effectiveness, ε:

$$\boldsymbol{\Theta \equiv \frac{\Phi_0}{\Phi_{min}} = \frac{\varepsilon}{\left[1+\Gamma_c{}^{-2/3}(1-\varepsilon)^{2/3}\right]^{3/2}}} \qquad \textbf{Equation 2-9}$$

where Φ_{min} is the minimum flow rate to prevent ingress and Γ_c is the ratio of the discharge coefficients for ingress, $C_{d,i}$, and egress, $C_{d,e}$.

The equivalent equations for the non-dimensional ingress, Φ_i, and egress, Φ_e, are given by:

$$\boldsymbol{\Theta \equiv \frac{\Phi_i}{\Phi_{min}} = \frac{\varepsilon}{\left[1+\Gamma_c{}^{-2/3}(1-\varepsilon)^{2/3}\right]^{3/2}}} \qquad \textbf{Equation 2-10}$$

and

$$\boldsymbol{\Theta \equiv \frac{\Phi_e}{\Phi_{min}} = \frac{\varepsilon}{\left[1+\Gamma_c{}^{-2/3}(1-\varepsilon)^{2/3}\right]^{3/2}}} \qquad \textbf{Equation 2-11}$$

Popovic *et al*. (2013) studied engine representative rim seals, as shown in Figure 2-12(a-b). A large-scale linear cascade was used including a secondary air system capable of independently varying the mass flow-rate and swirl of the leakage flow. It was found that the industry representative rim seals shown by Figure 2-12(a) produced a poor sealing effectiveness compared to an improved rim seal shown by Figure 2-12(b). The authors suggested the sealing effectiveness was low due to the lack of sharp corners and associated recirculation zones. It was concluded that sharp corners and hooks improved sealing effectiveness; these seal features generated internal recirculation zones that act to restrict further ingestion into the wheel-space.

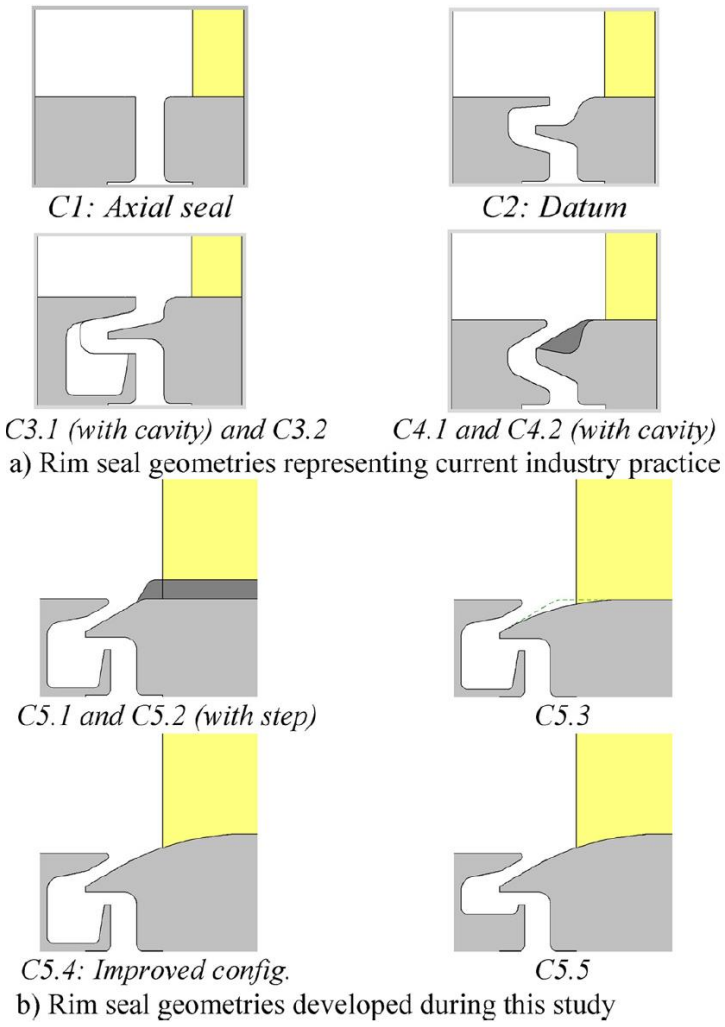

Figure 2-12: Tested rim seals; a) engine realistic seals; b) improved seals (Popovic *et al*, 2013)

Wang *et* al. (2013) performed simulations using a 360º, unsteady, 3D CFD model. Simulations of annulus flow showed that, the vane wake and blade bow wave interact,

resulting in asymmetrical pressure distributions. Large-scale structures were found to rotate in the same sense as the rotor at 86% of rotor speed. The results also revealed that increasing the sealing flow rate reduces the size of large-scale structures. The same effect was found by (Chilla *et al*. (2013). In the inner wheel-space the large-scale structures disappeared with high sealing flow-rates.

Scobie *et al.* (2015) conducted an experimental and computational study that lead to a patented rim-seal design, shown in Figure 2-13. The experiments were conducted in a 1-stage test rig at the University of Bath and the CFD computations were performed at Siemens Industrial Turbomachinery in Lincoln. The results of the CFD simulations showed a counter-rotating vortex in the outer wheel-space which shielded the stator wall from hot ingested fluid. The computations of sealing effectiveness, ε_c with non-dimensional sealing flow, Φ_0, revealed how each design feature of the seal (Figure 2-14) helped to combat ingestion and provided the minimum amount of sealing flow, Φ_{min},', needed to fully seal the wheel-space; for each feature. The EI orifice model developed by Owen (2011b) was fitted to the experimental data and showed good agreement. The authors concluded that the model was able to capture the flow physics of ingress.

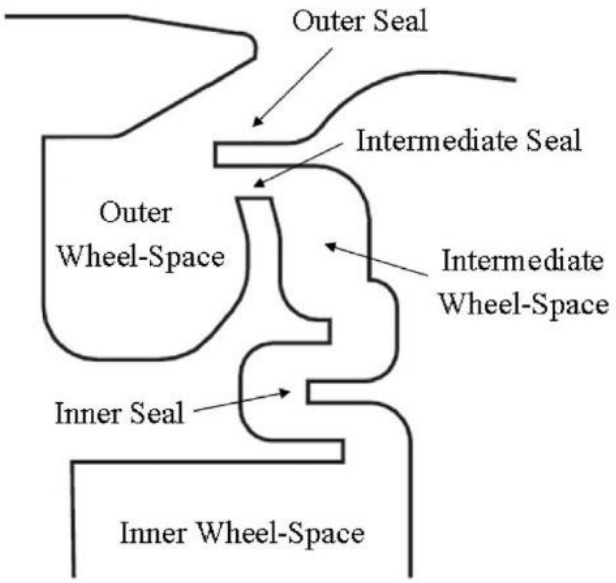

Figure 2-13: Rim seal design features (Scobie *et al,* 2015)

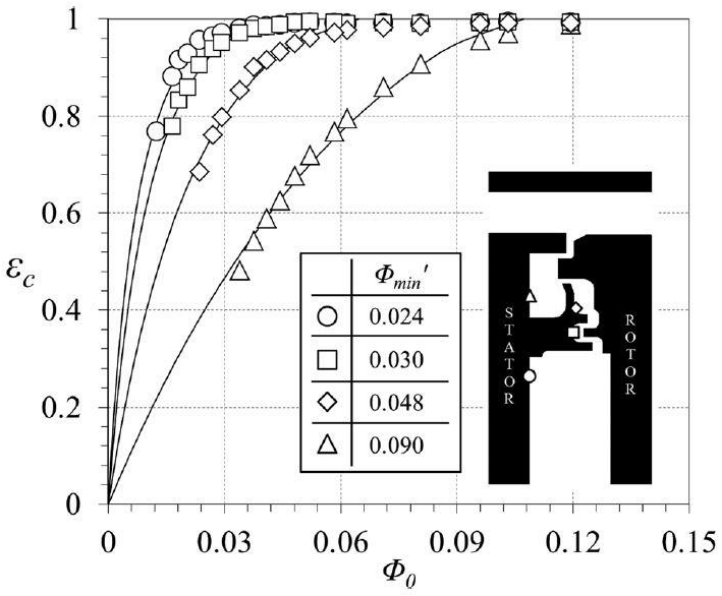

Figure 2-14: Variation of ε_c with Φ_0, for various locations of the improved seal (from Scobie *et al,* 2015)

Patinios *et al*. (2016) conducted experimental measurements in the upstream and downstream wheel-spaces of a 1.5- stage turbine rig. Engine representative rim seals were tested at incompressible operating conditions. A seeding method was used, which consisted of CO_2 as the tracer gas, this method was also used by (Clark *et al*. (2016)). The measurements revealed that a double-radial clearance seal (Figure 2-15) protects the upstream and downstream wheel-spaces significantly more compared to an axial or single-radial clearance seal. The author's discovery agreed with previously published data by (Sangan *et al* (2012a) and (Sangan *et al* (2013b). It was noted that downstream of the blade, external flow crossed an egress curtain before being ingested into the downstream wheel-space, this curtain enhanced the sealing effect. Furthermore, the author confirmed that ingress and egress flow get fully mixed after entering either upstream or downstream wheel-spaces, as discussed by James *et al*. (2017). It was concluded that in the upstream wheel-space the double-radial clearance seal outperformed the axial and single radial seals, furthermore, the combination of the double-radial clearance seal and the protective curtain, improved the sealing performance and provided a double cooling effect in the downstream wheel-space.

.

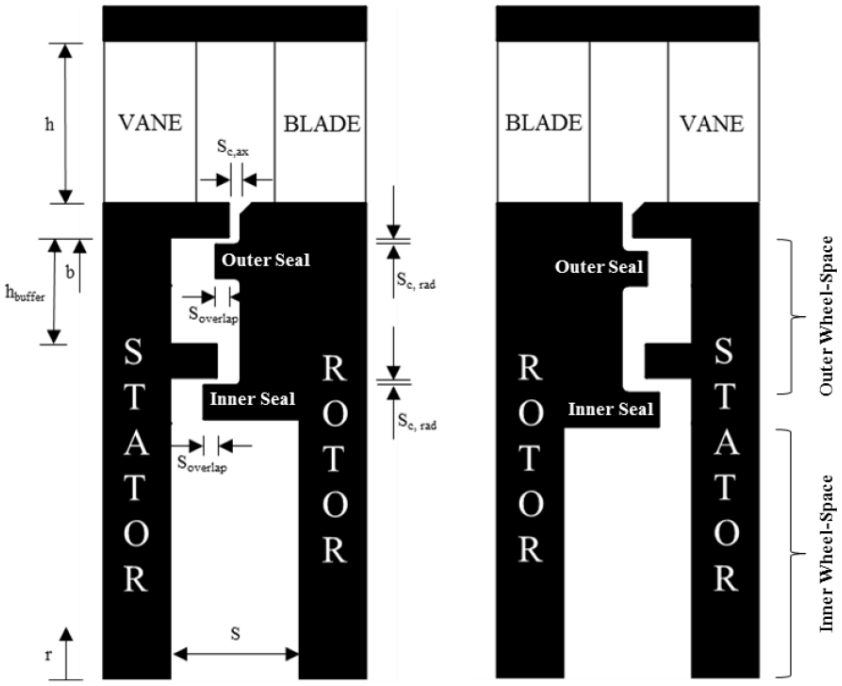

Figure 2-15: Upstream (left) and downstream (right) seal configurations for a double-radial clearance seal (Patinios *et al,* 2016)

Beard *et al*. (2016) conducted an experimental study regarding rim sealing flows, building on earlier experimental and numerical research by Boudet *et al*. (2005) and Gentilhomme *et al*. (2003). The experiments were conducted in a 1-stage rig, at the Oxford rotor facility. The turbine stage consisted of a chute seal and a rotor-stator system without blades or vanes. Cross-correlation of unsteady pressure measurements revealed that rotating flow structures existed in the wheel-space, rotating at approximately 22 times the rotor speed. The frequency was dependent on purge flow rate and rotational speed. It was found that near the rim seal region, the unsteadiness was strongest, but was sensitive to purge flow rate. Data were cross correlated with results showing that, for the 1mm seal gap, the cavity frequency corresponded to 26-29 large scale flow structures (lobes) as shown in Figure 2-16. These structures rotated with angular velocity, ω_s, at about 80% of the rotor speed, 0.8Ω, separated by an angle β with a time-lapse of Δt_β. Similar structures were found by Savov *et al*. (2016). The speed of the rotating structures, ω_s, was found to be independent of RPM and purge rate. The authors noted that the experimental results provide evidence of the existence of flow structures in the wheel-space, confirming previously published experimental and CFD studies by Rabs *et al*. (2009) and Wang *et* al. (2014).

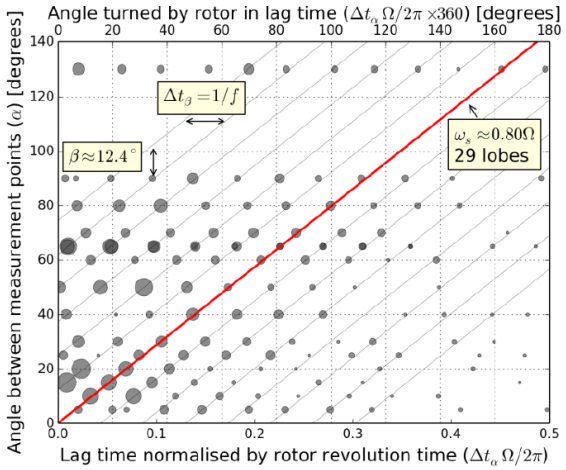

Figure 2-16: Cross-correlation of unsteady pressure data, for all sensors (Beard *et al*, 2016)

Savov *et al*. (2016) investigated shear-induced unsteadiness and the blade pressure field for a single and double clearance rim seal. A bladed and bladeless rotor disc was tested for two different Reynolds number, Re_θ, and isentropic Mach number, M_{is}. The results demonstrated that the double clearance seal performed substantially better than the single clearance seal. Steady pressure measurements revealed that the single clearance seal was more highly affected by the blade pressure field compared to the double clearance seal. Furthermore, the presence of the rotor blades had a detrimental effect on the sealing performance of the rim seals as shown in Figure 2-17. Spectrograms of unsteady pressure (Figure 2-18) revealed stronger fluctuations in pressure for the bladeless rotor case than for the bladed rotor case, with frequencies at 25-35 times disk passing frequency. The results were consistent for both rim seals. The authors associated the spectral fluctuations with shear layer instabilities, caused by the interaction between the annulus flow and rim seal flow.

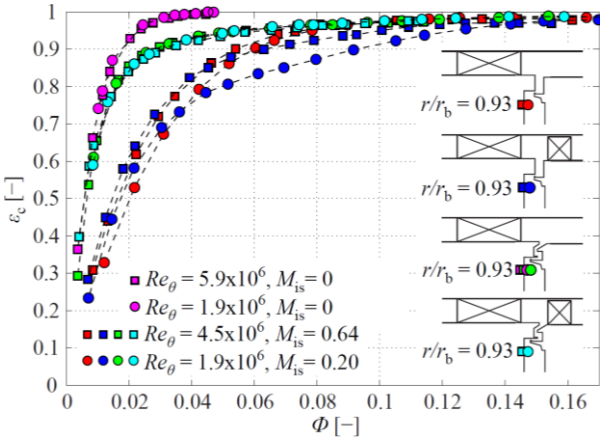

Figure 2-17:Sealing effectiveness for a single and double lip rim seal. Bladed and bladeless data are measured over a range of purge flow rates at engine-matched flow coefficient (Savov *et al*, 2016)

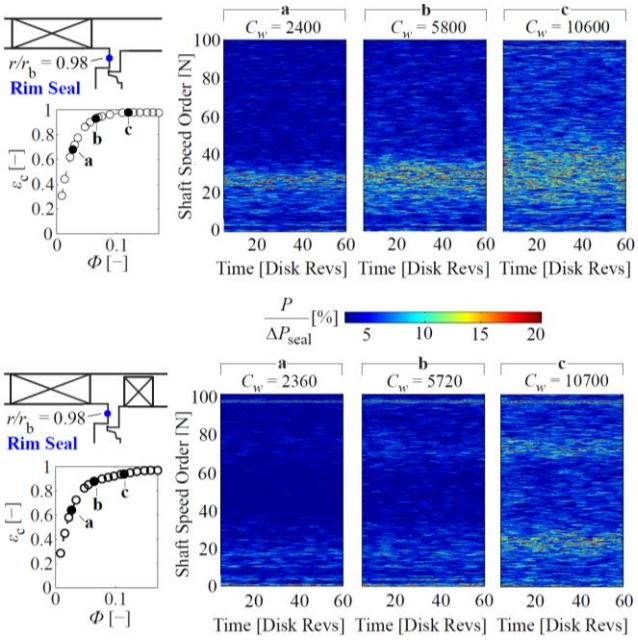

Figure 2-18: Spectrograms for bladeless and bladed data (Savov *et al*, 2016)

Schadler *et al.* (2017) experimentally and numerically investigated the interaction between external flow and frequency modes near the rim seal. The experiments were conducted in an engine representative 1.5-stage test rig with a bladed rotor disc. Measurements of unsteady pressure were made using fast-response aerodynamic probes, at two purge flow rates. Time-resolved experimental measurements and unsteady RANS simulations demonstrated sealing flow dependant low frequencies that increased aerodynamic losses. A high purge case showed that aerodynamic losses increased by 3%, compared to a low purge case. The authors concluded that rim seal induced frequencies need to be considered in the early design process, in order to reduce aerodynamic losses.

Clark *et al*. (2018) tested the sealing effectiveness of an engine realistic rim seal and rim cavity at engine-relevant conditions for two distinct purge flow configurations. The experiments were conducted in a 1.5-stage turbine at engine representative operating conditions. The wheel-space was sealed by individual purge holes. Two configurations were used, one with 32 purge holes and another with 150. The results showed that purge flow increased the sealing effectiveness, confirming results also found by Chew *et al* (2018), with measurements taken at high radius producing significantly lower sealing effectiveness, as shown in Figure 2-19. The authors found that 150 purge holes produced a higher sealing effectiveness than 32, at all radial locations on the rotor.

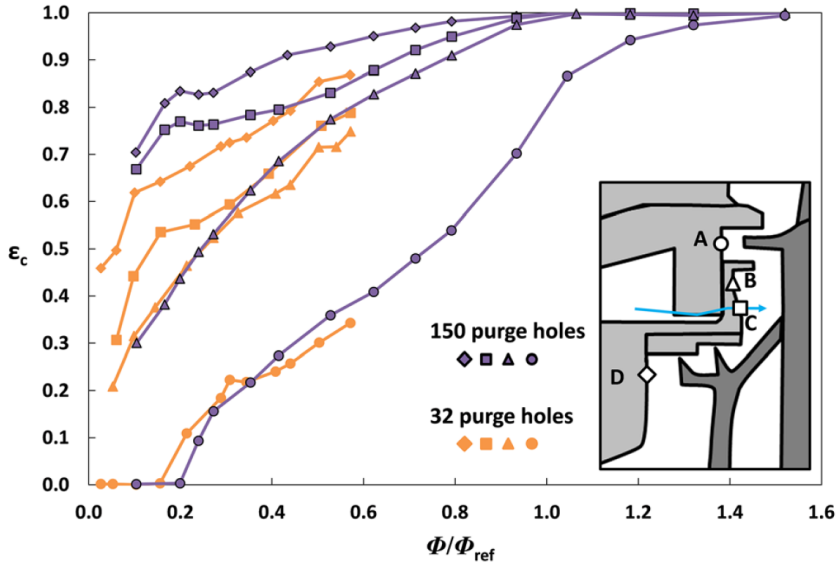

Figure 2-19: Gas concentration effectiveness curves for two purge hole configurations (Clark *et al*, 2018)

2.4 Theoretical Model for Re-ingestion

Scobie *et al.* (2017) measured re-ingestion through experiments. The quantity of re-ingestion was evaluated using a theoretical model developed by Mike Owen. The model consists of two main flow effects; a disturbance effect and a carry-over effect. The derivation and explanation of the model is expressed in the sections below.

Disturbance and Carry-over effect

The sealing effectiveness, ε, can be defined in terms of the mass flow of ingress, egress and superposed sealing flow, $\dot{m}_i$, $\dot{m}_e$, and $\dot{m}_0$:

$$\boldsymbol{\varepsilon = 1 - \frac{\dot{m}_i}{\dot{m}_e} = \frac{\dot{m}_o}{\dot{m}_e}} \qquad \textbf{Equation 2-12}$$

Here, concentration measurements (c) are used as a proxy and the concentration effectiveness is defined as;

$$\boldsymbol{\varepsilon_c = \left(\frac{c_s}{c_0} - \frac{c_a}{c_a}\right)} \qquad \textbf{Equation 2-13}$$

where the subscripts *a*, *0*, and s respectively denote the values measured in the annulus, in the sealing flow at inlet to the wheel-space and on the stator. A disturbance is a fluid-dynamic effect where the upstream egress disrupts the pressure field near the downstream seal. It should be noted that this disturbance effect could alter both ε_d and consequently $\varepsilon_{c,d}$ whereas the addition of seeding to the upstream wheel-space should not alter ed. Here, the subscripts *u* and *d* are used to denote the upstream and downstream wheel-spaces (Figure 2-20).

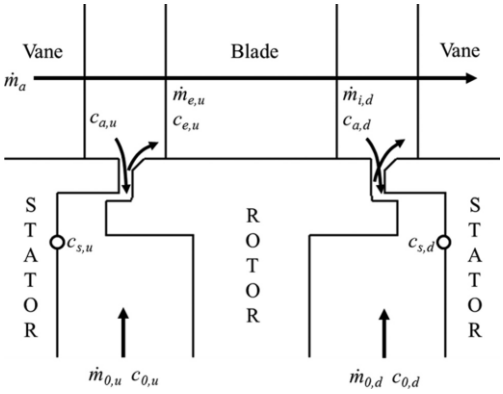

Figure 2-20: Simplified representation of mass flowrates and concentration.

It is assumed here that $\varepsilon_{c,u}=\varepsilon_u$, but, as discussed below, $\varepsilon_{c,d}$ is only equal to ε_d if it is defined correctly. Carry-over is defined as the seeded egress fluid not being fully mixed with the mainstream, so that the concentration of the fluid ingested into the downstream wheel-space is greater than the fully mixed value. To separate the disturbance and carry-over effects, it is necessary to conduct two sets of experiments for a range of upstream and downstream sealing flow rates: one set without and one with seeding added to the upstream sealing flow. These are referred further as the upstream-unseeded and upstream-seeded tests. For the upstream-unseeded tests, if the measured effectiveness in the downstream wheel-space, $\varepsilon_{c,d}$, is invariant with $(\Phi_o/\Phi_{min})_u$ and hence with ε_u then, the disturbance effect is not significant. However, if the upstream-unseeded tests do make a difference, so that ε_d depends on ε_u, the distribution of ε_d with $(\Phi_o/\Phi_{min})_d$ would need to be measured for different values of ε_u. The upstream-unseeded distributions of downstream effectiveness are referred to here as the datum cases, denoted by $\varepsilon^*_{c,d}$, with which the upstream-seeded distributions, $\varepsilon_{c,d}$, should be compared. That is,

$$\boldsymbol{\varepsilon^*_{c,d}} = \left(\frac{\boldsymbol{c_s}}{\boldsymbol{c_0}} - \frac{\boldsymbol{c^*_a}}{\boldsymbol{c^*_a}}\right)_{\boldsymbol{d}} \qquad \textbf{Equation 2-14}$$

where the downstream concentration in the annulus equals the upstream value, so that $c^*_{a,d}=c_{a,u}$. For the *upstream-seeded* tests, if $\varepsilon_{c,d} > \varepsilon^*_{c,d}$ this implies that there has been a carry-over of upstream egress, which has increased the concentration of the fluid ingested from the annulus into the downstream wheel-space, so that $c_{a,d} > c^*_{a,d}$. If the downstream effectiveness is incorrectly based on the upstream concentration in the annulus, the measured value of $\varepsilon_{c,d}$ will not equal the true value of ε_d. To reconcile $\varepsilon_{c,d}$ and ε_d, it is necessary to define $\varepsilon_{c,d}$ on the *actual* concentration of the fluid ingested into the wheel-space, $c_{a,d}$. That is, $\varepsilon_{c,d}$ should be defined as,

$$\boldsymbol{\varepsilon_{c,d}} = \left(\frac{\boldsymbol{c_s}}{\boldsymbol{c_0}} - \frac{\boldsymbol{c_a}}{\boldsymbol{c_a}}\right)_{\boldsymbol{d}} \qquad \textbf{Equation 2-15}$$

It follows that

$$\boldsymbol{c_{a,d}} = \left(\frac{\boldsymbol{c_s - c_0\varepsilon_c}}{\boldsymbol{1-\varepsilon_c}}\right)_{\boldsymbol{d}} \qquad \textbf{Equation 2-16}$$

If $\varepsilon_{c,d} = \varepsilon_d = \varepsilon^*_{c,d}$, it follows that,

$$\boldsymbol{c_{a,d}} = \left(\frac{\boldsymbol{c_s - c_0\varepsilon^*_c}}{\boldsymbol{1-\varepsilon^*_c}}\right)_{\boldsymbol{d}} \qquad \textbf{Equation 2-17}$$

Concentration in the annulus

For fully-mixed flow in the annulus downstream of the rotor,

$$(\dot{\boldsymbol{m}}_{\boldsymbol{0}}\boldsymbol{c_0})_{\boldsymbol{u}} + (\dot{\boldsymbol{m}}_{\boldsymbol{a}}\boldsymbol{c_a})_{\boldsymbol{u}} = (\dot{\boldsymbol{m}}_{\boldsymbol{0}} + \dot{\boldsymbol{m}}_{\boldsymbol{a}})_{\boldsymbol{u}}\tilde{\boldsymbol{c}}_{\boldsymbol{a,d}} \qquad \textbf{Equation 2-18}$$

That is, when seeding is added to the upstream sealing flow, the mixed-out concentration in the downstream annulus is given by,

$$\tilde{\boldsymbol{c}}_{\boldsymbol{a,d}} = \frac{(\dot{\boldsymbol{m}}_{\boldsymbol{0}}\boldsymbol{c_0})_{\boldsymbol{u}} + (\dot{\boldsymbol{m}}_{\boldsymbol{a}}\boldsymbol{c_a})_{\boldsymbol{u}}}{(\dot{\boldsymbol{m}}_{\boldsymbol{0}} + \dot{\boldsymbol{m}}_{\boldsymbol{a}})_{\boldsymbol{u}}} \qquad \textbf{Equation 2-19}$$

If there were no mixing in the annulus, then the ingress from the boundary layer on the rotor platform would be entirely egress from upstream. Under these circumstances the fluid ingested into the downstream wheel-space would have the same concentration as that of the egress from the upstream wheel-space, $c_{e,u}$, where,

$$\boldsymbol{c_{e,u}} = (\boldsymbol{c_0\varepsilon_c} + (\boldsymbol{1} - \boldsymbol{\varepsilon_c})\boldsymbol{c_a})_{\boldsymbol{u}} \qquad \textbf{Equation 2-20}$$

Mass fraction of re-ingested fluid

Consider the control volume (CV) shown in Figure 2-21, located outside the downstream seal where the carry-over fluid from the upstream egress ($\dot{m}'$) mixes with the downstream egress ($\dot{m}_{e,d}$) and ingress ($\dot{m}_{i,d}$). After mixing, all the fluid is assumed to leave the CV with the same concentration, $c_{i,d} = c_{s,d}$; this would be the value measured on the downstream stator and representative of the core concentration in the wheel-space as presented in Figure 1-10.

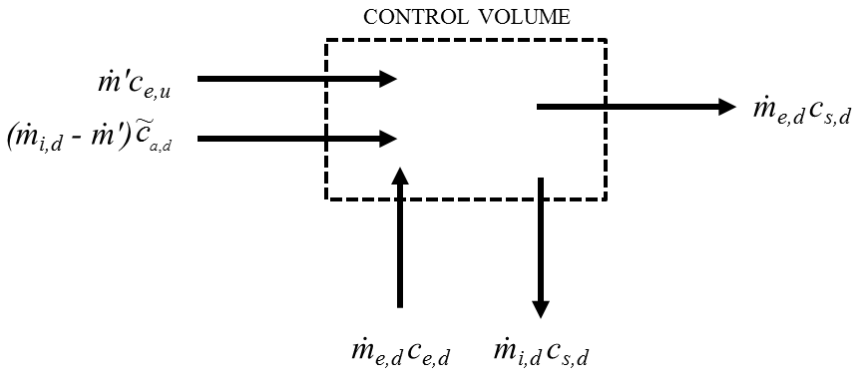

Figure 2-21: Representation of control volume.

$$(\dot{m}c)_{in} = \dot{m}'c_{e,u} + (\dot{m}_i - \dot{m}')\tilde{c}_{a,d} + (\dot{m}_e c_e)_d \quad \textbf{Equation 2-21}$$

The mass-concentration out of the CV is:

$$(\dot{m}c)_{out} = (\dot{m}_e c_s)_d + (\dot{m}_i c_s)_d \quad \textbf{Equation 2-22}$$

As

$$\dot{m}_{e,d} = (\dot{m}_0 + \dot{m}_i)_d \quad \textbf{Equation 2-23}$$

and

$$(\dot{m}c)_{e,d} = (\dot{m}_i c_s)_d + (\dot{m}_0 c_0)_d \quad \textbf{Equation 2-24}$$

it follows that

$$\dot{m}'c_{e,u} + (\dot{m}_{i,d} - \dot{m}')\tilde{c}_{a,d} + (\dot{m}_0 c_0)_d = \left((\dot{m}_0 + \dot{m}_i)c_s\right)_d \quad \textbf{Equation 2-25}$$

Hence, if $\dot{m}_{i,d} > 0$, the mass fraction is given by

$$\chi \equiv \frac{\dot{m}'}{\dot{m}_{i,d}} = \frac{c_{o,d} - c_{s,d}}{c_{e,u} - \tilde{c}_{a,d}} \left(\frac{c_{s,d} - \tilde{c}_{a,d}}{c_{0,d} - c_{s,d}} - \left(\frac{\dot{m}_0}{\dot{m}_i}\right)_d \right) \quad \textbf{Equation 2-26}$$

where

$$\left(\frac{\dot{m}_0}{\dot{m}_i}\right)_d = \left(\frac{\varepsilon^*}{1-\varepsilon^*}\right)_d$$ **Equation 2-27**

In the limit when $\dot{m}_{0,d} = 0$, Equation 2-15 reduces to

$$\chi = \frac{c_{s,d} - \tilde{c}_{a,d}}{c_{e,u} - \tilde{c}_{a,d}}$$ **Equation 2-28**

2.5 The Gap in the Literature

Ingress is a highly documented topic, with numerical orifice models, experimental data and CFD computations explaining the phenomenon. The literature shows that most of the studies focus on, experimental and CFD investigations that involve the application of purge flow into the upstream wheel-space, to assess the sealing effectiveness (performance) of rim seals and to study the effects (dependency) of rotational Reynolds number. Most of the studies have been conducted using generic (experimental) rotor-stator stages with generic rim-seals.

Abe *et al.* (1979) found that ingestion becomes suppressed with the addition of sealing flow, but on a non-engine representative rig that included only a stator disc with vanes and a generic rim-seal, like the rig used by Chew *et al.* (1994) where it was found that the amplitude of the circumferential pressure increased with a shift in the vane position. Phadke and Owen (1988c) expanded the work by Abe *et al.* (1979), and found that for all seals tested, the minimum amount of sealing flow needed to prevent ingress increased with increasing seal clearance ratio, but for a test rig without vanes and blades, just like the rig used by Dadkhah *et al*. (1992) where it was found for the first time that the rotor could experience a cooling effect. Furthermore, Bohn *et al.* (2000) found that for a simple rim-seal the rotor blades have an adverse effect on sealing effectiveness, this contradicts the work by Green and Turner (1994), however, for a more intricate rim seal, the blades had a positive effect that resulted in an increase in sealing effectives, which agrees with the work by Hills *et* al. (2002).

The experiments conducted by Feiereisen *et al*. (2000) found 24-34 large-scale structures rotating at speeds below the disc speed, in a 1-stage test rig. It was suggested that the structures formed due to shear layer interaction mechanisms, but no definitive explanation was given. The structures were dominant compared with the blade passing mode, and their strength were suppressed as the purge mass flow was increased. Similar results were also found in the work conducted by Jakoby *et al.* (2004) and Rabs *et al*. (2009). Rabs *et al*. (2009) found that the structures were suppressed by the presence of the vanes and blades and was concluded that the structures significantly influenced the mainstream ingestion and were linked to Kelvin-Helmholtz instabilities. Furthermore, Wang *et* al. (2013) found the occurrence of large-scale structures that rotated at 86% of rotor speed and weakened with increasing sealing flow, but for a simplified stage with, vanes, blades and rim-seal which did not represent a realistic engine stage. Similar results were found by Chilla *et al*. (2013). Recent studies by Beard *et al*. (2016) and Savov *et al*. (2016) also found the existence of flow instabilities near the rim-seal region. Beard *et al*. (2016) found that 25-30 large-scale flow structures formed near the rim-seal and rotated at about 80% the rotor speed, but for a single stage without vanes or blades. This excludes important vane-blade interactions that occur in real engines.

Little experimental work has been conducted in the downstream wheel-space, specifically to evaluate the interaction of upstream egress and annulus flow. Furthermore, there are contractions between Green and Turner (1994), Bohn *et al.* (1995), Chew *et al.* (1994), and Bohn *et al.* (2000), regarding the effect of vanes and blades on ingestion. Studies regarding flow instabilities (Kelvin Helmholtz instabilities) in rotor-stator systems have not been studied thoroughly. There is not a single study that tabulates in detail, the number and speed of structures against sealing flow rate, for an engine realistic 1.5-stage with vanes and removable blades. Furthermore, there is not enough data to explain and conclude the effect large-scale structures has on ingestion. Although a vast number of generic rim-seals and vane-blade configurations have been tested, not many studies have investigated ingestion with an engine realistic (geometrically scaled) vane-blade geometry, rim-seal and wheel-space. The is very little literature about re-ingestion into downstream stages. Eastwood *et al*. (2012) conducted temperature experiments and found that that 7% of egress leaving the upstream wheel-space gets re-ingested in the downstream wheel-space, however heat transfer was not considered, and temperature conditions were not controlled accurately. It was concluded the re-ingested flow reduced with increasing sealing flow in the upstream wheel-space.

To fill the missing gaps in the literature, the author aims to conduct experiments in an engine scaled 1.5-stage turbine rig that possesses the flexibility to accommodate any vane, blade and seal geometry. The present study aims to answer the following questions:

1) *Can a prove be traversed across the annulus and seal clearance to study the interaction or mainstream and egress? How far does the upstream egress penetrate the mainstream annulus flow upstream and downstream of the blade? And, is there a flow asymmetry in the seal clearance?*
2) *Does the vane and blade relative proximity influence ingestion? What effect do the blades have on ingestion? And, how are large-scale flow structures affected by different vane-blade configurations and sealing flow rate?*
3) *Does the flow structure in the wheels-space change for an engine realistic (geometrically scaled) vane-blade geometry, rim-seal and wheel-space? Do large-scale flow structures behave the same way in an engine realistic stage as in a generic experimental stage?*
4) *How is re-ingestion transported into the downstream wheel-space? How does the upstream egress expand across the blade passage? How much of the upstream egress gets re-ingested into the downstream wheel-space? Can re-ingestion be quantified using a tracer gas technique? And, why is re-ingestion beneficial for a typical gas turbine engine?*

Results and answers for the above questions are presented in Chapters 4, 5, 6, and 7, respectively, and a complete discussion is presented in Chapter 8.

2.6 Thesis Aim and Objectives

The aim of this experimental research is to improve the engine designer's knowledge regarding the effect vanes and blades has on the fluid dynamics associated with hot gas ingestion. To provide fundamental understanding of re-ingestion of upstream egress flow into the downstream wheel-space, and to provide new understanding on how the formation of large-scale flow structures (Kelvin Helmholtz instabilities) influence ingestion, for generic and engine-realistic gas turbine stages. It is hoped that this experimental study will inspire current and future engine designers, to produce better secondary air systems for the gas turbines of the future.

Data were collected using a newly built 1.5-stage turbine rig. The rig was designed by Dr. James Scobie and built by Dr. Marios Patinios, in 2015. However, the turbine rig was upgraded and modified by the author in order to conduct the new experiments presented in this study. The research presented in this thesis aims to accomplish the following objectives:

1. Investigate the interaction of egress and annulus flow using a gas concentration traverse probe, and to assess how this affects ingestion in the wheel-spaces.
    a. To perform gas concentration and pressure measurements in the annulus and upstream wheel-space, for generic single radial-clearance rim seal.
    b. To quantify the annulus and egress flow interaction using a gas concentration traverse probe, in the upstream and downstream wheel-spaces.
2. To examine what effect the relative proximity of stator vanes and rotor blades and the absence of rotor blades has on ingestion and flow instabilities.
    a. To investigate the influence of vane position relative to the seal clearance trailing edge stator vanes, in the upstream wheel-space.
    b. Perform unsteady pressure measurements in the upstream wheel-space, to investigate the formation of large-scale flow structures near the rim seal.
3. To investigate the sealing performance and flow structure of a geometrically scaled Siemens turbine stage.
    a. Conduct gas concentration, steady pressure and unsteady pressure measurements in the upstream wheel-space, for an engine realistic stage and rim seal.
    b. To validate CFD data.

4. To study the re-ingestion behaviour and flow mechanics in the downstream wheel-space using a 1.5-stage turbine rig, and apply a theoretical model developed by Prof Mike Owen, to quantify and evaluate the mass fraction of the re-ingested fluid from upstream egress.
    a. Conduct probe measurements to demonstrate that mixing between the re-ingestion and downstream egress occurs near the rim seal region.
    b. Evaluate re-ingestion for a range of sealing flow-rates.

It is hoped that the outcomes of this investigation have significant impact in the gas turbine research and industry community. This thesis aims to offer great contribution to the topic of ingress in rotor–stator systems.

Chapter 3: The Bath 1.5-Stage Test Facility

A 1.5-stage turbine rig was used to conduct the experiments. A brief description of the main rig components and vane-blade profiles are provided in this chapter as well as instrumentation and rim seal geometries. The operating capabilities and an uncertainty analysis for the important parameters are also presented.

3.1 Rig Description

The Bath 1.5-stage turbine rig has evolved through a successful research collaboration with Siemens, aimed to fundamentally investigate ingress. An exploded CAD view of the main components can be seen in Figure 3-1(a). The turbine rig was designed to be modular and accessible, to allow easy exchangeability of the stator and rotor discs and instrumentation. The purpose for a modular rig was to be able to conduct various comparative experiments, back to back and within the same day, this provided virtually identical ambient conditions.

A centrifugal compressor supplies mainstream at flow-rates up to 1.6 kg/s, the air then flows through two heat exchangers where the temperature of the flow is reduced in order to achieve a desired TET, the mainstream then flows to the annulus through a radial diffuser comprising 32 pipes before entering a transition section. In the transition section the flow becomes fully developed and then enters the test section that is encased by two 180^{o} segments which provide easy access to the turbine stage.

The mainstream and sealing flow are supplied, measured and controlled using thermal mass flow meters and valves. Sealing flow to the upstream wheel-space is supplied via one sealant feed, shown in Figure 3.1(a), and to the downstream wheel-space via 16 individual sealant feeds, shown in Figure 3.2.

The rotor disc is connected to a shaft by a hydraulic coupling and can rotate at speeds up to 5200 RPM, the rotor can spin faster but the compressor cannot supply enough mainstream flow in order to match the engine's operating point. The shaft is rotated by a 34 kW drive-and-brake dynamometer, required to absorb the power generated from the rig. A photograph of the 1.5-stage turbine rig is shown in Figure 3-1(b).

The rig was constructed from various materials, the radial diffuser and sealant feed were made from carbon fibre, the inlet pipes, annular transition, casing, upstream and downstream stator discs were made from aluminium and the rotor disc was made from titanium.

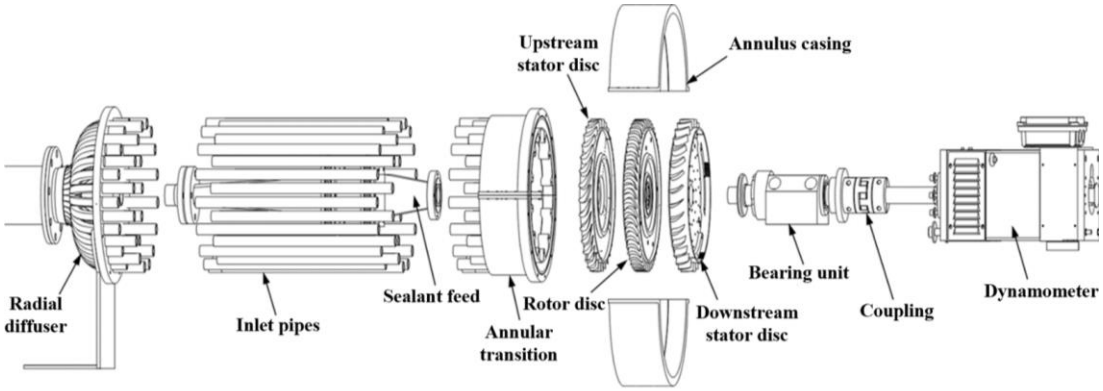

(a)

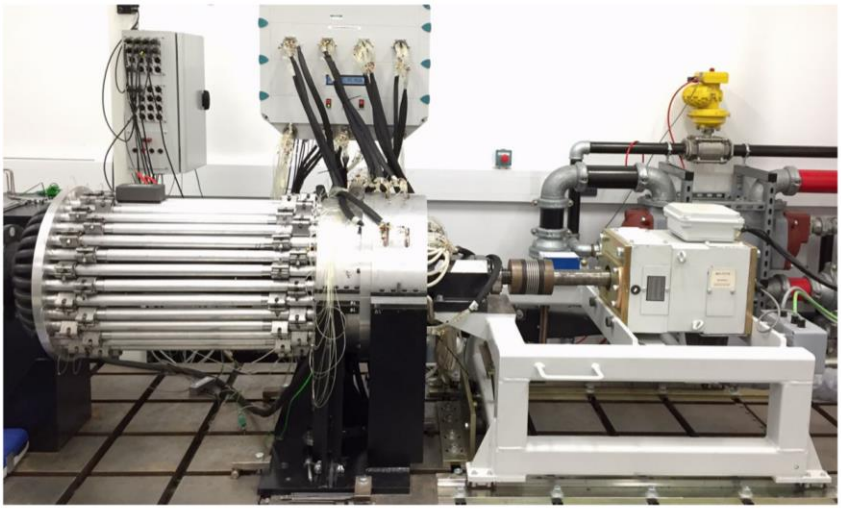

(b)

Figure 3-1: (a) Exploded view of the 1.5-stage turbine rig (Patinios *et al*, 2016), (b) assembled rig in the laboratory.

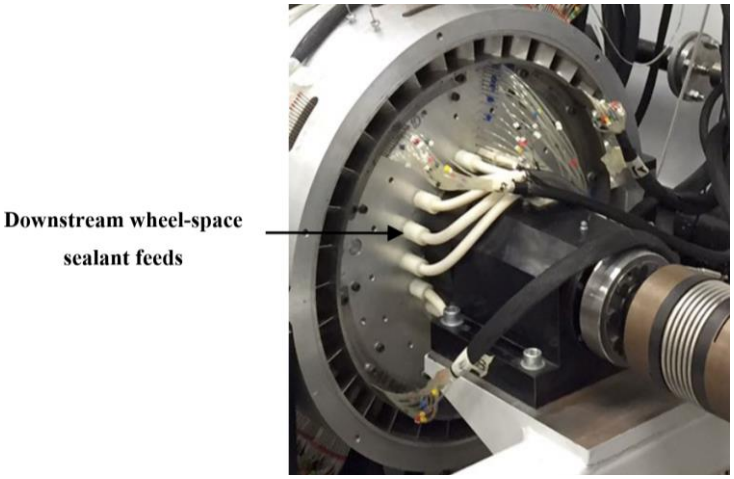

Figure 3-2: Downstream sealant feeds (shown in white)

Tables 3-1, 3-2, 3-3 and 3-4 show all the operating conditions tested in the 1.5-stage turbine test facility. Experiments were performed at four rotor disc speeds of 3000, 3840, 4000 and 5181 RPM. The tested rotational Reynolds numbers are an order of magnitude less ($Re_\phi \sim 10^6$) than that which occurs in a real engine ($Re_\phi \sim 10^7$), however the range of the turbulent flow parameter, $\lambda_T < 0.22$, is engine representative, therefore a typical Batchelor flow-structure is expected in the wheel-spaces, according to Owen and Rogers (1989). Using a mass flow controller, the quantity of external flow supplied to turbine rig can be adjusted to test different flow coefficients, C_F. This allows testing at off-design conditions. The operating flow coefficients for this study are C_F = 0.293, 0.35 and 0.407, other flow parameters can be found in Table 3-1, 3-2 and 3-3, respectively. In this study the vanes exit Mach number (0-0.5) are relatively low compared to the Mach numbers that occur in a real engine (> 0.7).

Table 3-1: Operating conditions of the 1.5-stage rig for upstream and downstream wheel-spaces (Chapter 4)

Parameters	**Disc Speed (RPM)**	
	3000	**4000**
Rotational Reynolds Number, $\mathbf{Re}_\phi$	7.2×10^5	1.0×10^6
Axial Reynolds Number, $\mathbf{Re}_w$	2.1×10^5	2.9×10^5
Vane exit Mach number, $\boldsymbol{M}$	0.24	0.32
Flow coefficient, $\boldsymbol{C_F}$	0.293	

Table 3-2: Operating conditions of the 1.5-stage rig for upstream wheel-space (Chapter 5)

Parameters	**Disc Speed (RPM)**	
	3000	**4000**
Rotational Reynolds Number, $\mathbf{Re}_\phi$	7.4×10^5	1.0×10^6
Axial Reynolds Number, $\mathbf{Re}_w$	3.0×10^5	4.1×10^5
Vane exit Mach number, $\boldsymbol{M}$	0.33	0.44
Flow coefficient, $\boldsymbol{C_F}$	0.407	

Table 3-3: Operating conditions of the 1-stage for the upstream wheel-space (Chapter 6)

Parameters	**Disc Speed (RPM)**	
	3840	**5181**
Rotational Reynolds Number, $\mathbf{Re}_\phi$	9.6×10^5	1.3×10^6
Axial Reynolds Number, $\mathbf{Re}_w$	3.4×10^5	4.6×10^5
Vane exit Mach number, $\boldsymbol{M}$	0.37	0.50
Flow coefficient, $\boldsymbol{C_F}$	0.35	

Table 3-4: Operating conditions of the 1.5-stage rig for upstream and downstream wheel-spaces (Chapter 7)

Parameters	Disc Speed (RPM)	
	3000	**4000**
Rotational Reynolds Number, $\mathbf{Re}_{\phi}$	7.2×10^5	1.0×10^6
Axial Reynolds Number, $\mathbf{Re}_{w}$	2.1×10^5	2.9×10^5
Vane exit Mach number, $\boldsymbol{M}$	0.24	0.32
Flow coefficient, $\boldsymbol{C_F}$	0.293	

Two rotational Reynolds numbers were tested for each flow coefficient (C_F = 0.293, 0.35 and 0.407). The operating flow coefficients (C_F = 0.293, 0.35 and 0.407) were kept constant, for the tested rotational Reynolds numbers, this ensured constant velocity triangles. An illustrative example of the velocity triangles used in, Chapter 4 and 7, is shown by Figure 3-3, and the velocity parameters are shown in Table 3-5.

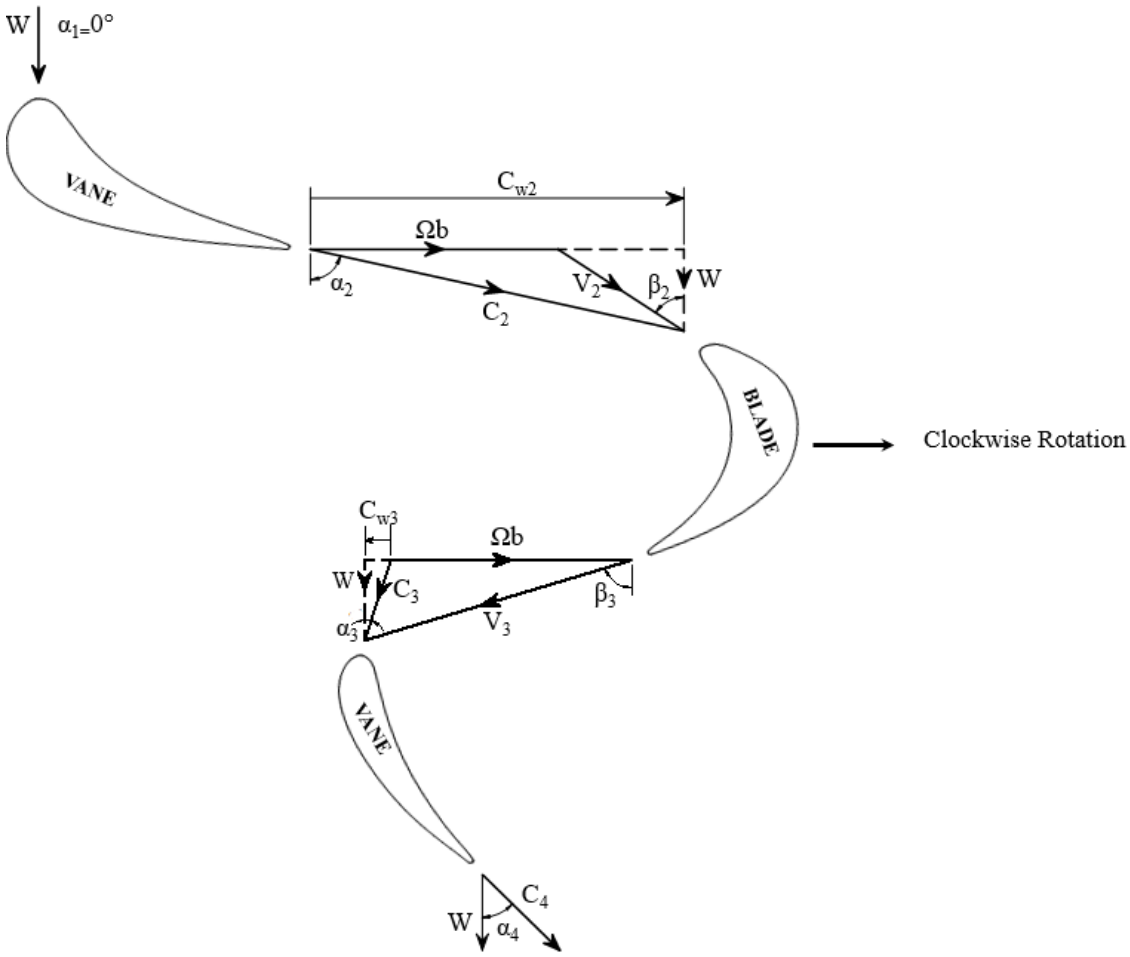

Figure 3-3: Velocity triangles for the 1.5-Stage turbine rig.

Table 3-5: Velocity triangle parameters for the 1.5-Stage turbine rig.

Velocity Triangle Parameter	**Disc Speed (RPM)**	
	3000	**4000**
Vane 1 Inlet Angle (α_1)	0°	
Vane 1 Exit Angle (α_2)	77.5°	
Blade Inlet angle (β_2)	63.2°	
Blade Turning angle ($\beta_2 + \beta_3$)	129.9°	
Blade Exit angle (β_3)	66.7°	
Vane 2 Inlet Angle (α_3)	11.8°	
Vane 2 Exit Angle (α_4)	46.3°	
Rotational Velocity (Ωb)	59.5 m/s	79.4 m/s
Axial Velocity (W)	25.6 m/s	34.1 m/s
Vane 1 Exit Velocity (C_2)	118.4 m/s	158.3 m/s
Blade Inlet Velocity (V_2)	57.3 m/s	76.1 m/s
Blade Exit Velocity (V_3)	65.3 m/s	86.5 m/s
Vane 2 Inlet Velocity (C_3)	26.1 m/s	35 m/s
Vane 2 Exit Velocity (C_4)	37 m/s	49.2 m/s

3.2 Vane and Blades Profiles

During this study two configurations were tested: a Siemens scaled 1.5-stage turbine and a 1-stage turbine. The 1.5-stage comprised an upstream and downstream stator disc with a rotor disc in between, altogether forming an upstream and downstream wheel-space. The operating flow coefficients for this stage were, C_F = 0.293 and 0.407, other flow parameters can be found in Tables 3-1. 3-2 and 3-4. The 1-stage comprised an upstream stator disc and a rotor disc that formed an upstream wheel-space only. The operating flow coefficient for this stage was, C_F = 0.35 (Table 3-3). The profile of the stator vanes and rotor blades of the 1.5-stage can be found in Figure 3-4. This stage is a geometrically scaled version of a Siemens engine. Both upstream and downstream stator discs have 32 vanes, and the rotor disc has 48 turned and untwisted blades. The profiles of the stator vanes and rotor blades of the 1-stage can be found in Figure 3-5. It is a geometrically scaled version of a Siemens gas turbine and the experimental facility at KTH Royal Institute of Technology. The stage comprises a chute seal, 48 vanes on the stator disc and 60 turned and twisted blades on the rotor disc. This work reports on the first phase of a collaboration with KTH to investigate the influence of scaling (Mach and Reynolds numbers) on ingress in gas turbines.

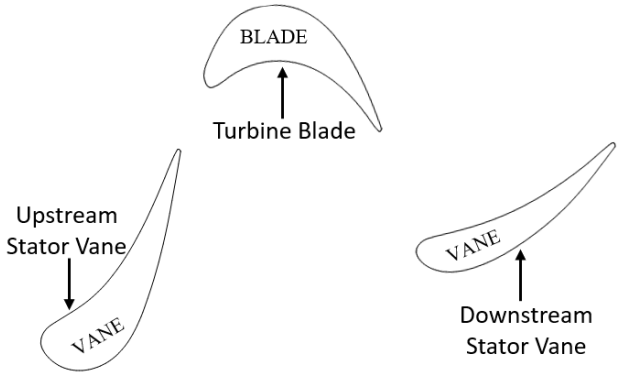

Figure 3-4: Vane and blade profiles of a geometrically scaled 1.5-stage version of a Siemens turbine

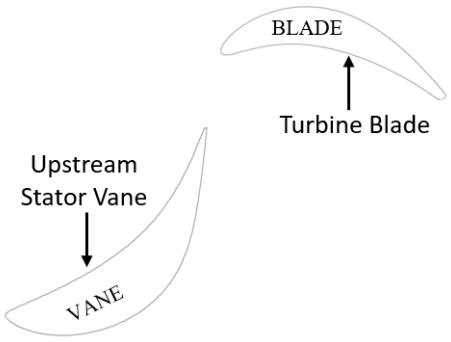

Figure 3-5: Vane and blade profiles of a geometrically scaled 1-stage version of the KTH test rig

3.2.1 Rim Seal Designs

Three type of gas turbine rim seals were tested in this study: a single radial clearance, double radial clearance and a chute seal. A single and double radial clearance rim seal was chosen because of its generic (simple) geometry, manufacturability and easy installation procedure. An engine realistic chute seal was chosen to study the effect, an engine realistic seal and wheel-space, has on ingestion. The first part of this study involved testing the performance of a single radial clearance rim seal in the upstream and downstream wheel-space of the 1.5-stage rig. A silhouette of this seal is shown by Figure 3-6. This includes the upstream vane-1, rotor blade and downstream vane-2. Axial and radial dimensions of the seal are presented in Table 3-6.

The second part of this study involved a double radial clearance rim seal, its performance was evaluated only in the upstream wheel-space of the 1.5-stage rig. The seal was strategically chosen in order to be able to conduct and compare an experimental and CFD study (Chapter 6). It benefited the CFD computation in terms of run-time and performance cost. A silhouette of this seal is shown by Figure 3-7, it includes the upstream vane-1 and blade, furthermore important axial and radial dimensions of the seal are shown in Table 3-7.

The final rim seal tested was an engine realistic chute seal. Its performance was evaluated in the upstream wheel-space using the 1-stage KTH geometry, a silhouette of this seal is shown in Figure 3-8. This includes the upstream vane and blade; important dimensions of this seal are shown in Table 3-8.

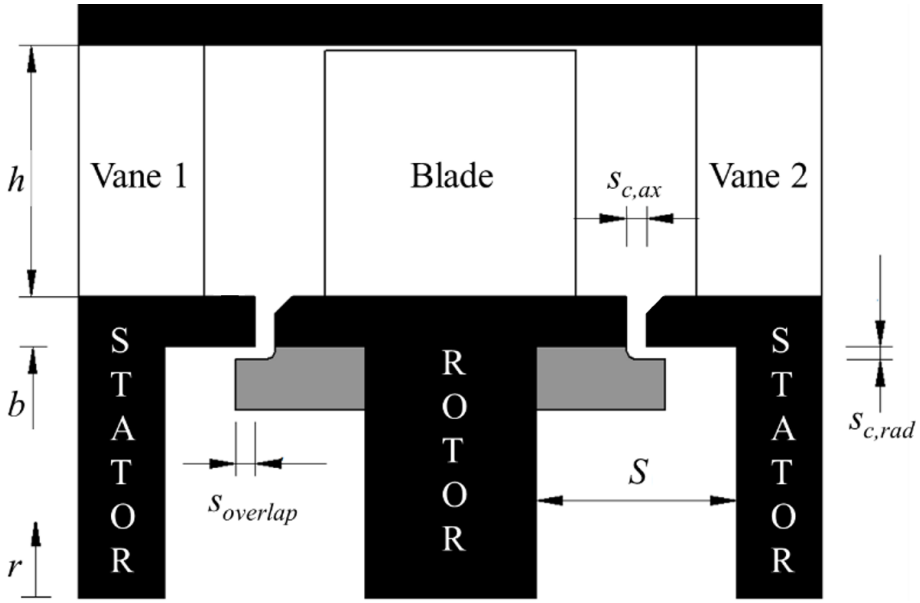

Figure 3-6: Silhouette of single radial-clearance rim seals upstream and downstream of the rotor disc (Scobie *et al,* 2018).

Table 3-6: Geometric dimensions for the single radial-clearance rim seal

Parameter	Dimension (mm)	
	Axial clearance	Radial clearance
h	25	25
b	190	190
S	20	20
$s_{c,ax}$	2	2
$s_{c,rad}$	-	1.28
$s_{overlap}$	-	1.86

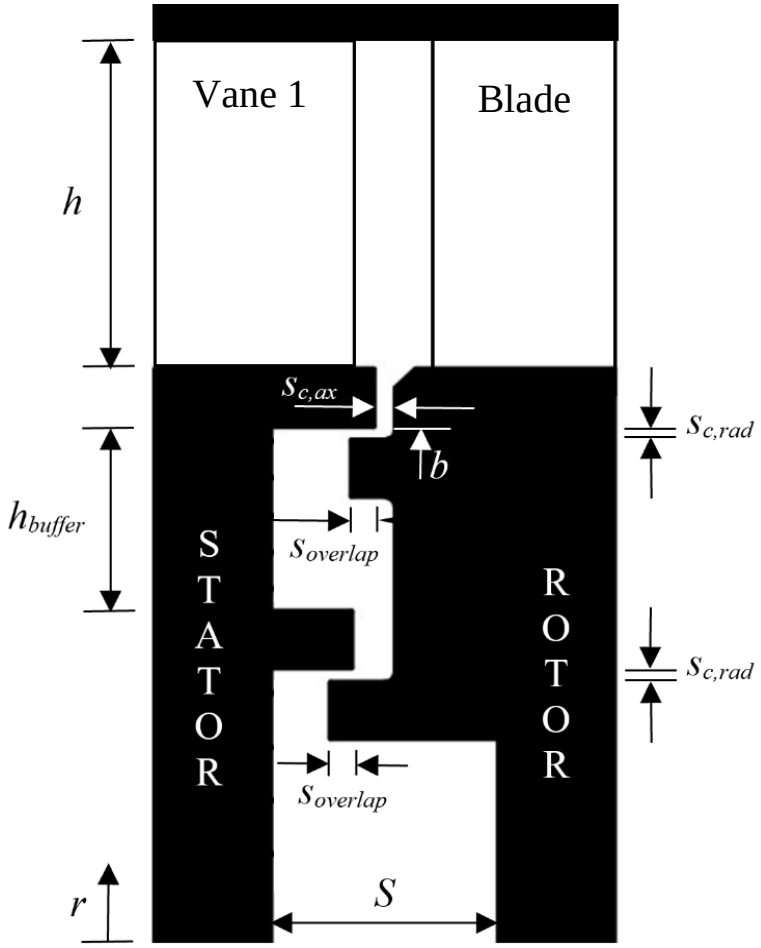

Figure 3-7: Silhouette of a double radial-clearance rim seal, for the upstream wheel-space (Scobie *et al*, 2018).

Table 3-7 Geometric dimensions for the double radial-clearance rim seal

Parameter	Dimension (mm)
h	25
b	190
S	20
H_{buffer}	16.5
$s_{c,ax}$	2
$s_{overlap}$	1.86
$s_{c,rad}$	1.28

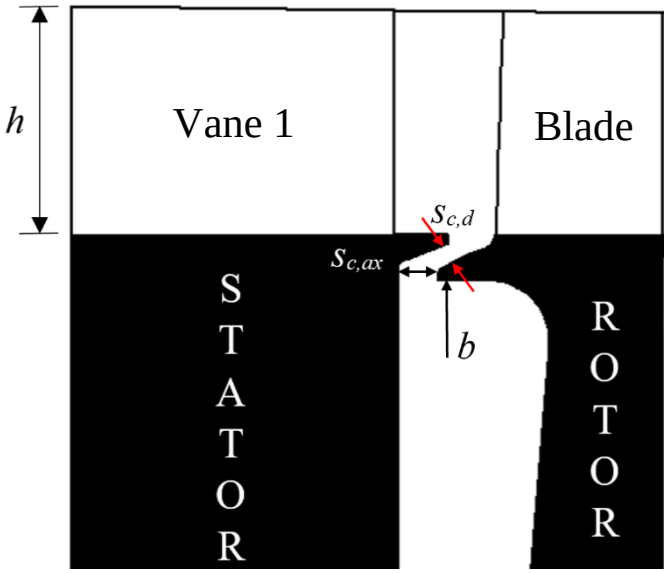

Figure 3-8: Silhouette of an engine representative chute seal, for the upstream wheel-space

Table 3-8 Geometric dimensions for an engine representative chute seal

Parameter	Dimension (mm)
h	25
b	190
$s_{c,ax}$	2
$s_{c,d}$	4

3.3 Instrumentation

3.3.1 Measurement Locations

The 1.5-stage test rig was designed for easy instrumentation access and assembly. This facilitates the investigation of different turbine stage designs and the performance of generic and advanced rim-seal geometries to better understand the fundamentals of the fluid mechanics with rotor-stator systems. Figure 3-9 shows where static (1), total pressure (2), CO_2 concentration (1 and 3) and unsteady pressure (4) measurements were taken. In the upstream and downstream wheel-spaces static pressure and CO_2 concentration were measured at radial locations on the wall of the stator discs. The tracer gas method (CO_2 concentration) is a mature and well documented experimental technique that is used to trace ingestion (Patinios *et al*. (2016) and Clark *et al*. (2016)). Total pressure and core concentration measurements were taken at radial in the core flow using hypothermic probes (2) that extrude 5 mm away from the wall of the stator discs . Unsteady pressure was measured at two circumferential locations using Kulite ultra-miniature (XCS-062-1PSI) transducers (4) located in the wheel-space at r/b=0.993, just below the vane platform lip. The static and total pressures, and annulus and sealing flow pressures were measured using differential pressure transducers. The acquisition of the experimental data and the operation of the 1.5-stage turbine was controlled by the Sierra-CP Engineering CADET system. This system commonly used by the automotive industry for testing engines but can be adapted to work with gas turbine rigs.

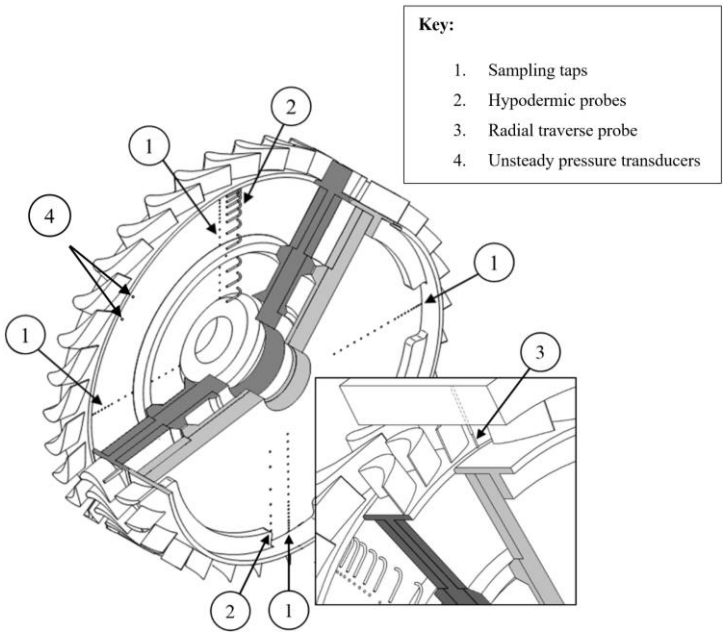

Figure 3-9: A cut-out through the downstream stator and rotor of the 1.5-stage rig (Scobie *et al,* 2018).

In the annulus, measurements of steady pressure were taken at two locations; at the outer wall in the annulus section and at the shroud of the stator disc. For the shroud of the upstream stator disc there are two sets of circumferential pressure taps (A1 and A2) at two axial locations, with identical versions 180^{o} apart from each other. Therefore, there are a total of four circumferential pressure taps. The same can be found in the downstream shroud of the stator disc. The pressure taps in the shroud of upstream and downstream stator discs cover one vane pitch, as seen in Figure 3-10. In the upstream outer wall of the annulus there are three sets of circumferential pressure taps (B1, B2 and B3) at three axial locations, as shown in Figure 3-11. Again, there are versions 180^{o} apart from each other. Therefore, there are a total of six circumferential pressure taps. The same can be found in the downstream outer wall.

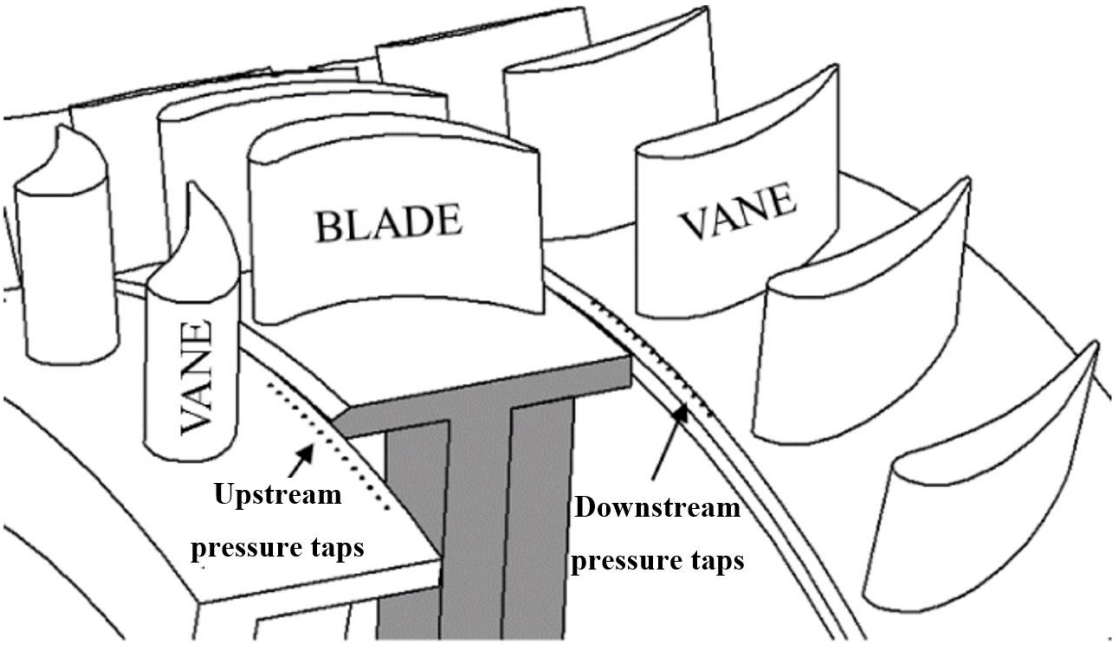

Figure 3-10: Upstream and downstream circumferential pressure taps across one vane pitch (Scobie *et al,* 2018).

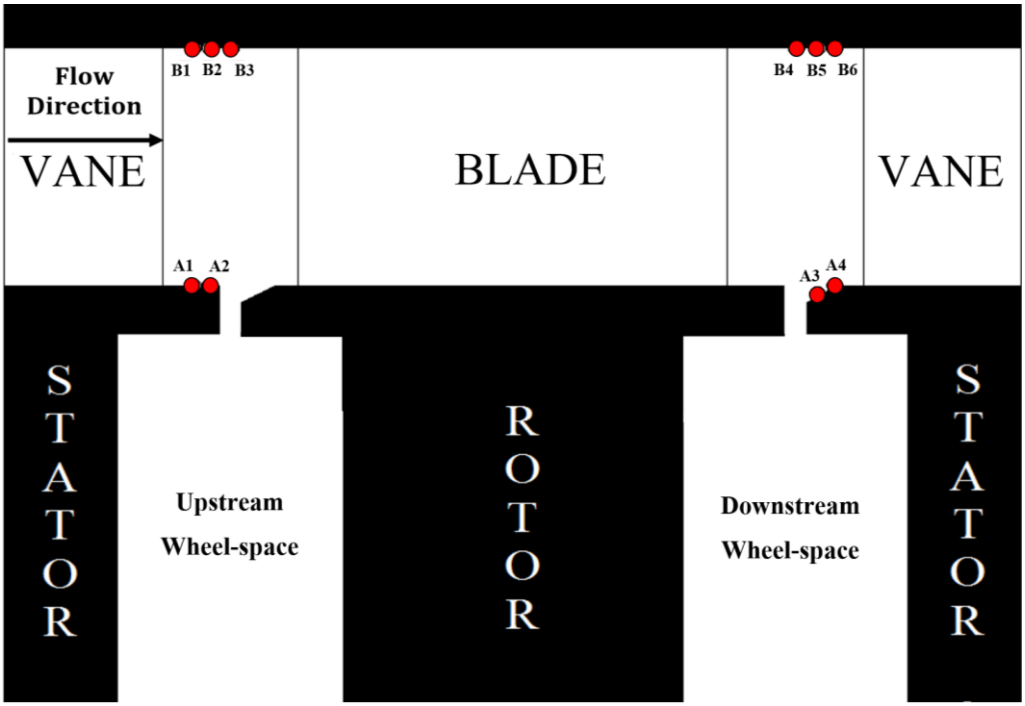

Figure 3-11: Circumferential pressure taps A1-A4 and B1-B6, upstream and downstream

Instrument	Manufacturer	Model	Range	Accuracy
Differential Pressure Transducers	ESI Technology	PR3202	0 – 150 mbar	Accuracy ±0.3% of range
			0 – 80 mbar	
			-40 – 40 mbar	
CO_2 Gas Analyser	Signal Group	9000MGA	1%	±0.5% of range Linearity: ±0.5% of range
Thermal Mass Flow Meters and Controllers	Bronkhorst	F-106EI	1.47 kg/s	± (0.5% of reading + 0.1% of range)
		F206-AI	0.048 kg/s	
			0.02 kg/s	
		F-202AI	0.003 kg/s	
Thermocouples	TC Direct	K-Type	0 – 100 °C	±0.2 °C
Unsteady Pressure Transducers	Kulite Sensors	XCS-062-1PSI	68.9mbar	±5mV

Table 3-9: Instrumentation specifications for 1.5-stage turbine test facility

The instrumentation used in this study is listed in Table 3-9. The differential pressure transducers were chosen to meet our pressure requirements, and for their accuracy and working pressure range. The gas analyser was chosen for its accuracy and applicability to this study. The thermal mass flow meters were chosen to satisfy out engine operating conditions and beyond. The thermocouples were chosen to operate in typical laboratory temperature conditions.

Using the measurements of static pressure , p, total pressure, p_T, (Figure 3-9) and rotational speed (Ω) of the turbine disc, the annulus pressure coefficient ($C_{p,a}$) and tangential velocity (V_Φ) in the wheel-space was quantified. With the measurements of unsteady pressure (p_{uns}) and rotational speed (Ω) of the turbine disc, the unsteady pressure coefficient C_p was quantified. With the measurements of gas concentration (C_s, C_a and C_o), the concentration of effectiveness (ε_c) was quantified. The swirl ratio (β) was calculated using the tangential velocity and the rotational speed of the turbine. All the equations for the important parameters used in this study are shown below.

The swirl ratio, β, is given by

$$\boldsymbol{\beta = \frac{V_\Phi}{\Omega b}} \qquad \textbf{Equation 3-1}$$

where V_Φ is the tangential component of velocity in the wheel-space, and can be calculated by rearranging Bernoulli's equation, to give:

$$\boldsymbol{V_\Phi = \sqrt{\frac{2(p_T - p)}{\rho}}} \qquad \textbf{Equation 3-2}$$

Here ρ is the air density which varies within the wheel-space and annulus and is evaluated at each measuring location.

The annulus pressure coefficient, $C_{p,a}$, is given by

$$\boldsymbol{C_{p,a} = \frac{(p_a - \overline{p_a})}{1/2\rho\Omega^2 b^2}} \qquad \textbf{Equation 3-3}$$

where p_a is the annulus pressure and $\overline{p_a}$ the average pressure across a vane pitch.

The concentration of effectiveness, ε_c, is given by

$$\boldsymbol{\varepsilon_c = \frac{(C_s - C_a)}{(C_0 - C_a)}} \qquad \textbf{Equation 3-4}$$

Here the concentration of CO_2 at the stator wall is defined as C_s, the concentration in the annulus is defined as C_a and is measured upstream of the nozzle guide vanes and C_0 is the

concentration in the sealing flow and is measured at the sealant feed just before the entry to the wheel-space. The concentration of effectiveness is determined by tracking the dilution of CO_2 at the sampling locations. If no sealing flow is supplied to the wheel-space, hence no CO_2, then maximum ingress occurs, resulting in $C_a = C_s$ and $\varepsilon_c = 0$. If enough sealing flow is introduced, sufficiently to prevent ingress, then $C_0 = C_s$ and $\varepsilon_c = 1$. For this study the sealing flow was seeded whilst the annulus flow was kept unseeded.

The non-dimensional sealing flow parameter, Φ_0, is given by

$$\boldsymbol{\Phi_0 = \frac{C_w}{2\pi G_c Re_\Phi} = \frac{U}{\Omega b}} \qquad \textbf{Equation 3-5}$$

where C_w is the non-dimensional axial flow rate, G_c the sealing clearance ratio, Re_Φ the rotational Reynolds number and U the bulk mean radial velocity of sealing flow across the seal.

The wheel-space unsteady pressure coefficient, C_p, is given by

$$\boldsymbol{C_p = \frac{(p_{uns} - \overline{p_{uns}})}{(1/2\rho\Omega^2 b^2)}} \qquad \textbf{Equation 3-6}$$

where p_{uns} is the instantaneous unsteady pressure in the wheel-space at r/b=0.993 and $\overline{p_{uns}}$ the average unsteady pressure for the entire sampling time.

Measurements of unsteady pressure were conducted in the wheel-space, at r/b=0.993, just below the vane platform lip. Measurements were taken at two circumferential locations and at the same PCD using Kulite ultra-miniature (XCS-062-1PSI) transducers with a characteristic natural frequency of 150 kHz. These transducers are temperature compensated from 10°C to 30°C. The sensors were flush mounted to the stator disc wall. At 4000 RPM the blade passing frequency (BPF) is 3.2 kHz for the rotor with 48 blades, and at 5181 RPM the BPF becomes 5.1kHz for the rotor with 60 blades. These frequencies are significantly lower than the manufacturer quoted natural frequency. Unsteady pressure data at $Re_\phi = 7.2\times10^5$ and $Re_\phi = 1.3\times10^6$ is presented in this study. The unsteady data were sampled at 100 kHz for 10 seconds, equivalent to 500 disk revolutions. The results were computed using a Fast Fourier Transform (FFT) of windowed segments of the signals.

3.3.2 Uncertainty of Measurements

The measurements obtained in the 1.5-stage turbine rig are influenced by various uncertainties that affect the recorded output values. Two well-known uncertainties include Type (A) and Type (B). An example of a type (A) uncertainty is, the variation of a measurement with time. Type (B) uncertainties include; transducer error, linearity and accuracy of the sensor, as well as calibration error.

Type A and Type B uncertainties can be combined to provide an overall uncertainty, given by,

$$u_m = \left(u_A^2 + u_B^2\right)^{\frac{1}{2}} \qquad \textbf{Equation 3-7}$$

For the uncertainty analysis that follows both Type A and Type B individual uncertainties are assumed to have been stated at a 95% confidence interval.

The use of data reduction equations results in the propagation of the overall uncertainty of the measurement which can be calculated using the root of the sum of the squares uncertainty (RSS) approach.

$$u_r = \left(\left(u_{X_1}\frac{\partial r}{\partial X_1}\right)^2 + \left(u_{X_2}\frac{\partial r}{\partial X_2}\right)^2\right)^{\frac{1}{2}} \qquad \textbf{Equation 3-8}$$

Based on the above, uncertainty analysis was performed for parameters associated with the experiments in the 1.5-stage turbine test facility. Rearranging $C_{p,a}$ from Equation 3.3 to give only measured quantities, results in,

$$C_{p,a} = \frac{(p_a - \overline{p_a})RT_{ref}}{1/2 p_{ref}\Omega^2 b^2} \qquad \textbf{Equation 3-9}$$

where R = 287 J/kgK the specific gas constant, T_{ref} and p_{ref} the reference temperature and absolute pressure respectively measured at r/b = 0.958 in the wheel-space. The result $C_{p,a}$ is therefore a function of six measured quantities, p_a, $\overline{p_a}$, p_{ref}, T_{ref}, Ω and b and the propagated uncertainty is given by

$$u_{C_{p,a}} = \left(\left(u_{p_a} \frac{\partial C_{p,a}}{\partial p_a} \right)^2 + \left(u_{\overline{p}_a} \frac{\partial C_{p,a}}{\partial \overline{p}_a} \right)^2 + \left(u_{p_{ref}} \frac{\partial C_{p,a}}{\partial p_{ref}} \right)^2 + \left(u_{T_{ref}} \frac{\partial C_{p,a}}{\partial T_{ref}} \right)^2 + \left(u_{\Omega} \frac{\partial C_{p,a}}{\partial \Omega} \right)^2 + \left(u_b \frac{\partial C_{p,a}}{\partial b} \right)^2 \right)^{\frac{1}{2}}$$ **Equation 3-10**

The uncertainty for $C_{p,a}$

By substituting the overall uncertainties (Table 3-10) and the values of these quantities measured during an experiment (Table 3-11), into Equation 3-10, the uncertainty in $C_{p,a}$ is calculated for each of the four Scani-Valves, these can be found in Table 3-12.

Table 3-10: Overall uncertainty in measured quantities in a standard pressure test

Scani-valve	Overall Uncertainty					
	u_{p_a} (Pa)	$u_{\overline{p}_a}$ (Pa)	$u_{p_{ref}}$ (Pa)	$u_{T_{ref}}$ (K)	u_{Ω} (RPM)	u_b (mm)
1	24.05	6.15	24.05	0.5	1	0.05
2	24.3	6.3	24.3			
3	25.8	6.59	25.8			
4	25	6.45	25			

Table 3-11: Measured values in a standard steady pressure test

Measured Quantity	Typical Values
p_a	Variable
$\overline{p_a}$	Variable
p_{ref}	101100 Pa
T_{ref}	293 K
Ω	3000 RPM
b	190 mm

Table 3-12: Uncertainty values of $C_{p,a}$ for each Scani-Valve

	Uncertainty for $C_{p,a}$
Scani-Valve	$u_{Cp,a}$
1	±0.0031
2	±0.0031
3	±0.0032
4	±0.0032

For simplicity, it can be assumed that Equation 3-10 was used for the calculation of uncertainty in the following parameters, β, ε_c and Cp.

The uncertainty for β

Using the overall uncertainty values from Table 3-13 and the typical values that these quantities take during an experiment in Table 3-14, u_β is calculated from Equation 3-10, for each of the four Scani-Valves. Over the range of experimental conditions, the uncertainty for β was calculated and the result was < 3%.

Table 3-13: Overall uncertainty in measured quantities in a standard swirl test

Scani-Valve	**Overall Uncertainty**					
	u_{p_T} **(Pa)**	u_p **(Pa)**	$u_{p_{ref}}$ **(Pa)**	$u_{T_{ref}}$ **(K)**	u_Ω **(RPM)**	u_r **(mm)**
1	24.05	24.05	24.05	0.5	1	0.05
2	24.3	24.3	24.3			
3	25.8	25.8	25.8			
4	25	25	25			

Table 3-14: Measured values in a standard swirl test

Measured Quantity	Typical Values
p_T	Variable
p	Variable
p_{ref}	101100 Pa
T_{ref}	293 K
Ω	3000 RPM
b	190 mm

The Uncertainty for ε

The CO_2 gas analyser used for the concentration measurements includes a dual channel configuration, this means both channels experience the same uncertainty, therefore the overall uncertainty for u_{Cs}, u_{Ca} and u_{C0} are equal. The overall uncertainty of the dual channels provided by the manufacturer is 0.0125% CO_2, which results in $u_{Cs} = u_{Ca} = u_{C0} = 0.0125\%$ CO_2 (Table 3-15) substituting the overall uncertainties in a standard concentration test and the typical values measured (Table 3-16), into Equation 3-10, $u_{\varepsilon c}$ is calculated. Over the range of experimental conditions, the uncertainty of ε_c resulted in $u_{\varepsilon c}= 0.0127$.

Table 3-15: Overall uncertainty in measured quantities in a standard concentration test

Overall Uncertainty						
u_{c_o} % CO_2	u_{c_a} % CO_2	u_{c_s} % CO_2	$u_{T_{ref}}$ (K)	u_{Ω} (RPM)	u_{Φ_o} (kg/s)	$u_{\dot{m}}$ (kg/s)
0.0125	0.0125	0.0125	0.5	1	0.000015	0.0075

Table 3-16: Baseline gas concentration values measured in a standard gas concentration test

Measured Quantity	Values
C_0	1% CO_2
C_a	0.047% CO_2
C_s	variable

Uncertainty for C_p

The overall uncertainty in the measured quantities for an unsteady pressure test can be found in Table 3-17, the actual values that these quantities take during a test can be found in Table 3-18. Substituting these values into Equation 3-10, the uncertainty in C_p is calculated for each Kulite pressure transducer, these can be found in table 3-19.

Table 3-17: Overall uncertainty in measured quantities in a standard unsteady pressure test

	Overall Uncertainty				
Kulite	$u_{p_{uns}}$ **(Pa)**	$u_{\bar{p}_a}$ **(Pa)**	u_{Ω} **(RPM)**	u_r **(mm)**	u_t **(s)**
1	10.2	10.2	1	0.05	0.001
2	10.1	10.1			

Table 3-18: Measured values in a standard unsteady pressure test

Measured Quantity	Typical Values
p_{uns}	Variable
$\overline{p_{uns}}$	Variable
Ω	3000 RPM
b	190 mm
t	10s

Table 3-19: Uncertainty values of C_p for each Kulite pressure transducer

	Uncertainty for C_p
Kulite	u_{Cp}
1	±0.0008
2	±0.0008

3.4 Summary

This chapter presented a detailed discussion of the major design features, operating capabilities and instrumentation of the turbine rig. Th 1.5-stage turbine rig was built to investigate ingress with a more advanced engine representative stage, compared to its predecessor, a 1-stage rig, built by Sangan *et al*. (2012). The rig operates with mainstream and sealing flows, which are controlled by accurate thermal mass flow meters. The 1.5-stage turbine stage consists of two stator discs with 32 vanes, and one rotor disc with 48 blades. The engine-realistic stage consists of one stator disc with 48 vanes and one rotor disc with 60 blades. The rotor discs can rotate at speeds up to 5200 RPM and above, but the compressor cannot supply enough mass flow in order to retain the engine's operating flow coefficient. An uncertainty analysis was performed for the annulus pressure coefficient, $C_{p,a}$, swirl ratio β, concentration effectiveness, ε_c and wheel-space pressure coefficient, C_p.

Chapter 4: Interaction Between Egress and Mainstream

This chapter presents experimental data acquired using a CO_2 extraction system in the 1.5-stage turbine test rig introduced in Chapter 3. The flow conditions can be found in Table 3-1. This chapter mainly focuses on a novel measuring technique for ingress concentration experiments, and the interaction between egress and mainstream, for two generic rim seals. Measurements were taken in both the upstream and downstream wheel-spaces. Levels of ingress and egress were measured using a CO_2 concentration probe, sealing flows in the upstream and downstream wheel-spaces were seeded with 1% CO_2 as required by the experiment.

It is important for engine designers to be able to precisely predict EI ingress that is driven by the circumferential pressure asymmetry in the mainstream annulus. The pressure asymmetry creates regions of high and low pressure, ingress occurs in the high-pressure regions and the outflow of purge (egress) occurs in the low-pressure regions. Near the hub end-wall of the rotor disc the interaction between egress and the mainstream (annulus flow) produces losses that decrement the aerodynamic performance.

4.1 Experimental Results

Experiments were conducted at two operating points, seen in Table 3-1. The experiments were conducted under engine representative values of λ_T. Incompressible flow exited the vanes; the speed of sound, density and viscosity of the flow was calculated using the static temperature and pressure measured on the stator wall inside the upstream and downstream wheel-spaces at a radial location of, r/*b* = 0.958. Single axial and radial-clearance rim seals were investigated with geometric parameters and dimensions given in Table 3-6. A silhouette of these seals can be seen in Figure 3-6.

4.1.1 Pressure Measurements in the Mainstream Annulus

Steady pressure measurements were made over a vane pitch (11.25°) upstream and downstream, using two independent sets of 15 pressure taps (diameter 0.5 mm) on the end-walls, A1 and A3 (Figure 4-1). The upstream set of pressure taps (A1) are located on the stator platform, 2.5 mm axially downstream of the upstream stator-vane trailing edge; the downstream set of pressure taps (A3) are located 1.5 mm axially downstream of the

downstream rim-seal. Both sets of pressure taps were duplicated at a circumferential location 180° apart to assess the uniformity of the flow around the annulus.

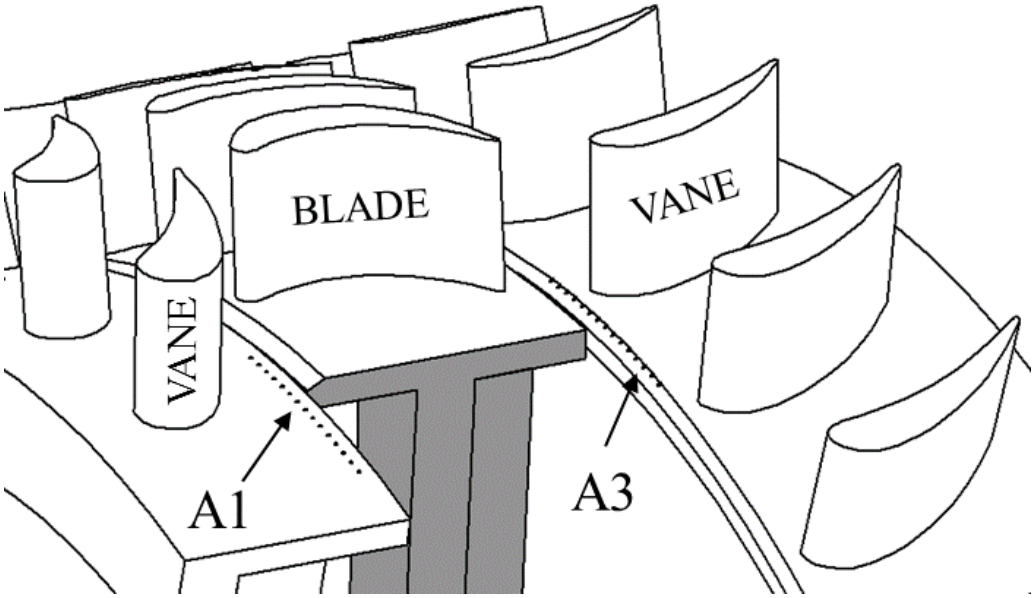

Figure 4-1: Location of upstream (A1) and downstream (A3) pressure taps on stator-vane platforms (Scobie *et al*, 2017)

The variation of pressure at locations A1 and A3 is shown in Figure 4-2. The measurements were made in the absence sealing flow, *i.e.* $\Phi_0 = 0$. Definitions for the non-dimensional pressure in the annulus ($C_{p,a}$) and peak-to-trough pressure difference ($\Delta C_{p,a}$) can be found in the nomenclature. Figure 4-2 shows that for the same operating flow coefficient of $C_F = 0.34$, $C_{p,a}$ and $\Delta C_{p,a}$ are not affected by Re_ϕ and can be said to be independent of rotational speed. Although not presented here, other rotational speeds were tested, and the results were consistent. Overall the results show a conventional trend, however there are three data points that show anomalous behaviour and it is believed that the cause could be dust or dirt inside the pressure taps. Patinios *et al.* (2017) demonstrated that $\Delta C_{p,a}$ decreases with axial distance from the vane trailing edge, for both upstream and downstream locations. In addition, the results demonstrate that $\Delta C_{p,a}$ is greater in the upstream (A1) than that downstream (A3). An unsteady pressure field exists in the annulus which decays with axial distance upstream from the leading edge of the blade overlaid onto a steady pressure field which decays with axial distance downstream of the trailing edge of the vane. Owen (2011) discusses how ΔC_p and Φ_{min} measurements obtained in a test rig could be used to scale up the results to a real engine.

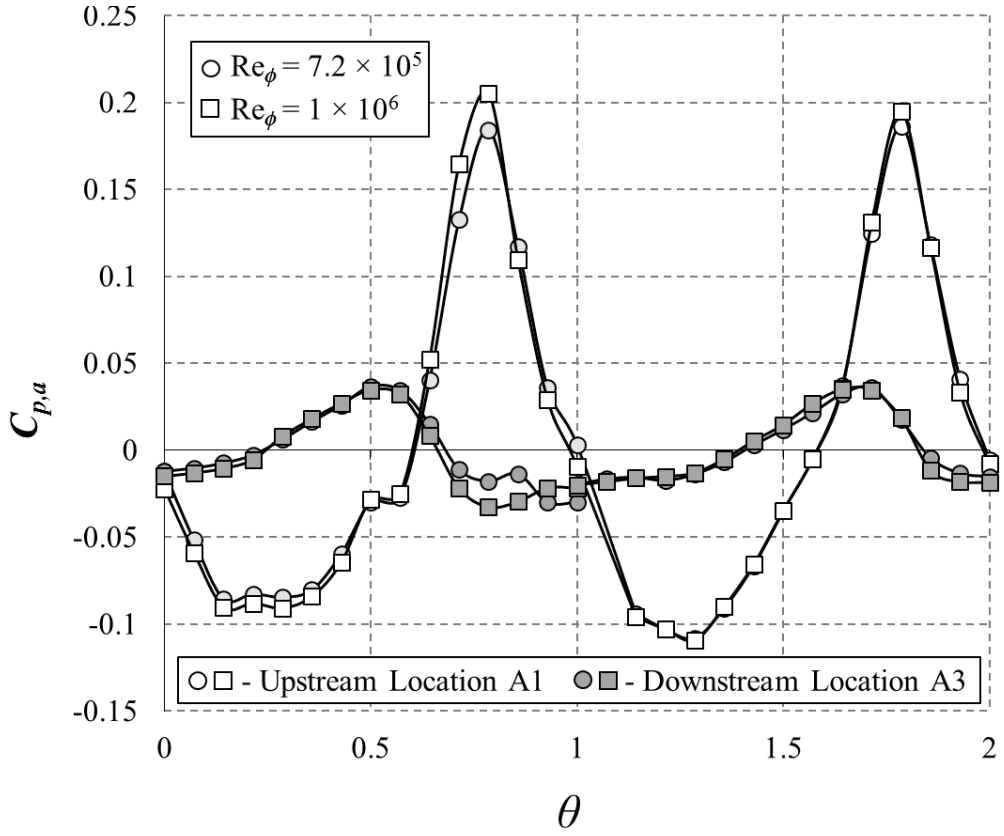

Figure 4-2: Circumferential distribution of steady pressure coefficient in the annulus over two non-dimensional vane pitches 180° apart (open symbols are location A1 upstream of rotor; grey symbols are location A3 downstream of rotor), by Scobie *et al.* 2017

4.1.2 Probe Validation

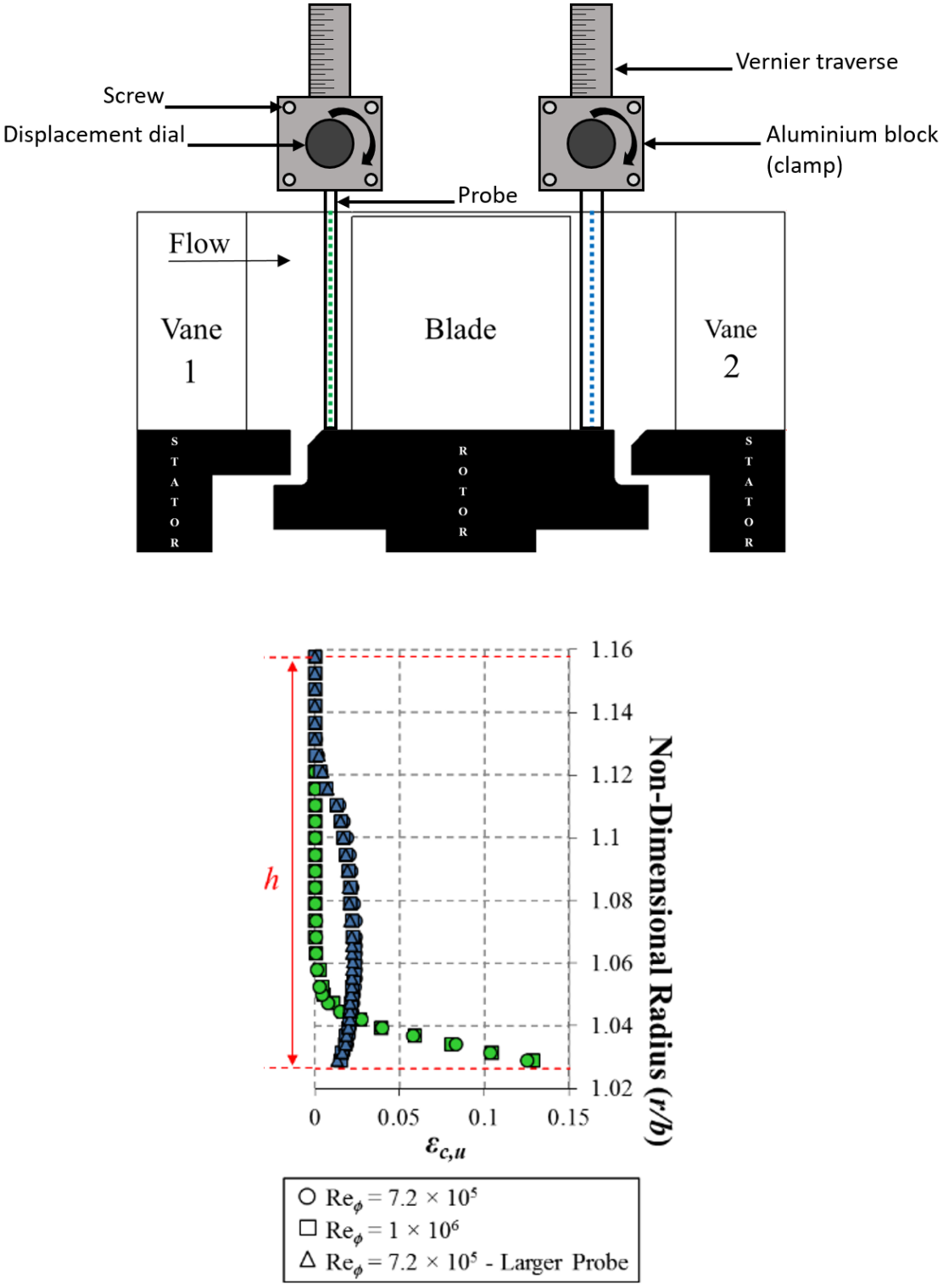

Figure 4-3: Measurements of upstream concentration effectiveness using a novel experimental technique, in the annulus either side of the rotor blades (Φ0,u = Φmin,u). By Scobie *et al.* (2017)

For the results presented in this section, a novel experimental technique was developed. This novel experimental set up involves a cylindrical probe, a Vernier traverse, clamping blocks and screws. The probe was attached to a Vernier traverse with small blocks and screws. The procedure consisted of firstly placing the probe to a start position of 0.5mm above the vane platform, setting up the flow conditions required for the experiment, and once the flow conditions were fixed, data were collected. For each measurement the displacement dial was turned, in order to lift the probe by 0.5mm - 1mm.

The variation of effectiveness in the annulus was measured using a probe both upstream and downstream of the rotor blades. A small probe (green dashed line) was attached to a Vernier-traverse stage and displaced vertically down by turning a rotary dial, the probe traversed the entire annulus section (Figure 4-3). A second larger probe (blue dashed line) was used in the downstream to assess the influence of the probe size. The two blue curves in Figure 4-3 (triangles for the large probe and squares for the small probe) overlay each other, therefore it was concluded that the probe size does not influence the measurements. The probes had outer diameters of 1mm and 1.7mm. Figure 4-3 shows the radial variation of effectiveness across the annulus section. On the y-axis is the non-dimensional radius; the results are plotted within the range of $1.03 \leq r/b \leq 1.16$ which corresponds to the annulus height, h = 25mm. Measurements of concentration effectiveness at the two Re_ϕ conditions show that the concentration profile is independent of rotational speed. The seeded sealing flow was supplied to the upstream wheel-space with $\Phi_{0,u} = \Phi_{min,u}$, $c_{0,u} = 0.03$ and $\varepsilon_{c,u} = 1$. The effectiveness, $\varepsilon_{c,u}$, is calculated using the local concentration measured by the probe (c) relative to the concentration of the egress flow in the upstream wheel-space:

$$\boldsymbol{\varepsilon_{c,u} = \frac{c - c_{a,u}}{c_{o,u} - c_{a,u}}} \qquad \textbf{Equation 4-1}$$

The effectiveness in the upstream is unity, $\varepsilon_{c,u} = 1$, when $c = c_{0,u}$, demonstrating no mixing between egress and mainstream and indicating that the local flow is purely from the upstream wheel-space. The effectiveness in the upstream is zero, $\varepsilon_{c,u} = 0$, when $c = c_{a,u}$, demonstrating that egress is not present in the annulus.

The location of the radial traverse measurements upstream of the rotor blades is shown in green data labels, and downstream of the rotor blades is shown in blue data labels. Upstream of the rotor blades a maximum effectiveness of $\varepsilon_{c,u} = 0.125$ was measured near the rotor platform. This shows that there has been interaction between the egress and the mainstream annulus. The effectiveness then reduces radially as the egress mixes further with the annulus flow. The results indicate a concentration boundary layer thickness of $0.18h$ ($1.03 \leq r/b \leq$

1.05). The results also suggest that there could a small benefit of film-cooling on the rotor platform as well as aerodynamic mixing losses. The concentration measurements downstream of the rotor blades reveal that flow diffuses radially to 0.8*h* (*r/b* = 1.13) and migrates into the blade passage vortex. Consequently, the interaction between the egress and mainstream annulus, downstream of the blades, reveals a maximum effectiveness of $\varepsilon_{c,u}$ = 0.024, and close to the downstream platform an effectiveness of $\varepsilon_{c,u}$ = 0.015. Although the effectiveness near the downstream rotor platform is low, *r/b* =1.03 or 0.25mm, the results suggests a low degree of film cooling could be beneficial as the sealing flow is typically an order of magnitude lower in temperature to that of the mainstream flow.

4.1.3 The effect of Reynolds number on concentration measurements

Traverse measurements in the annulus and through the mid-plane of an axial seal-clearance, shown in Figure 4-4. These measurements were made downstream of the rotor blades. The co-ordinate system in Figure 4-4 is geometrically aligned with the silhouette of the turbine passage. For this experiment the downstream wheel-space was fully sealed ($\Phi_{0,d} = \Phi_{min,d}$) and seeded with CO_2, this resulted in a sealing effectiveness of $\varepsilon_{c,d}$ = 1 as measured on the stator wall of vane-2 (black circle) at *r/b* = 0.958.

In the outer region (0.98 < *r/b* < 1) of the wheel-space the seeded purge flow experiences a small amount of ingress, for 0.98 < *r/b* < 1 (Figure 4-4), which results in an effectiveness of just below unity, $\varepsilon_{c,d}$=0.98. However, a large amount of mixing occurs across the seal, between the ingress and egress flow; for 1 < *r/b* < 1.026, further into the annulus the effectiveness becomes zero, $\varepsilon_{c,d}$ = 0. Measurements were made for two operating points, $Re_\phi = 1x10^6$ and $Re_\phi = 7.2x10^5$; the results show the concentration profiles are independent of rotational speed. Although not presented here, other rpm conditions were tested too, and the results were consistent.

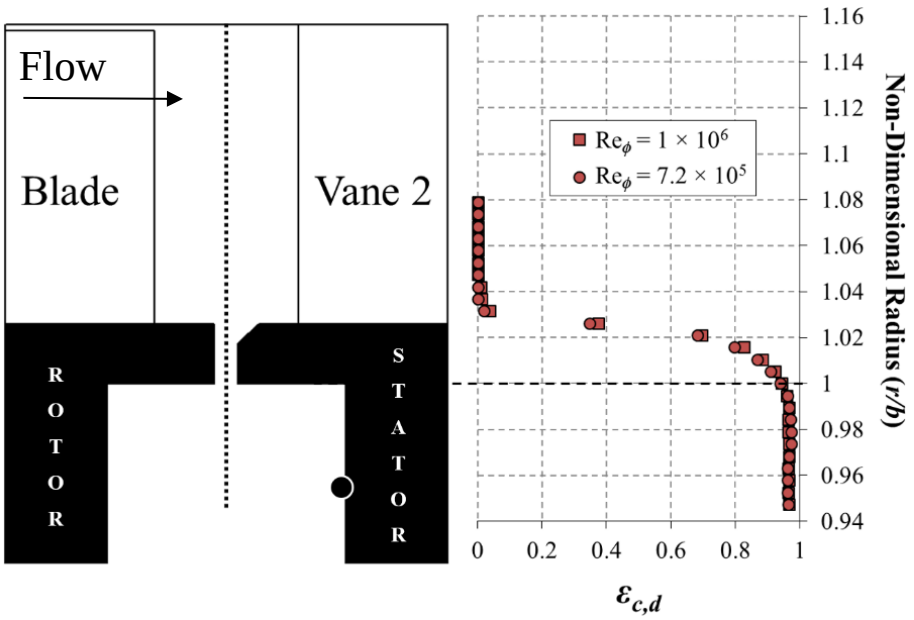

Figure 4-4: Radial variation of effectiveness at the seal clearance mid-plane (Scobie *et al*, 2017).

4.1.4 Radial Distribution of Effectiveness Through an Axial and Radial Rim-Seal

The flow structure in the downstream wheel-space was sampled at three sealing flow rates: $\Phi_{0,d} / \Phi_{min,d}$ = 0.28, 0.52 and 0.83. Figure 4-5 shows how the concentration of effectiveness, $\varepsilon_{c,d}$, varies across the annulus; measurements were taken downstream of the rotor blades and within the downstream wheel-space. The measurements in the core (diamonds) were taken using hypodermic probes in the shape of pitot tubes, at z/S = 0.25. Probe measurements (circles) across the annulus and through the middle of the seal clearance (vertical dotted line) were taken by traversing a probe through the casing of the rig. Measurements on the stator-wall (squares) were taken from taps distributed radially on the surface of the stator disc in the downstream wheel-space. The vertical axis is geometrically aligned with the silhouette of the stage. For all test cases, the effectiveness increases with increasing sealing air, Φ_0, as the wheel-space becomes pressurised. The wheel-space effectiveness does not change with radius for 0.65 < r/b < 0.975 and becomes fully mixed near the rim-seal. The effectiveness data acquired in the core collapses upon the stator wall effectiveness and shows consistency with the flow structure in Figure 1-10. The probe measurements at r/b > 0.975 show high mixing between the ingress and egress, resulting in a steep reduction in effectiveness, $\varepsilon_{c,d} \rightarrow 0$, this is consistent with Figure 4-4 in Section 4.1.3. For r/b < 0.65, there is an increase in effectiveness due to the inner seal which minimises ingestion into the inner wheel-space.

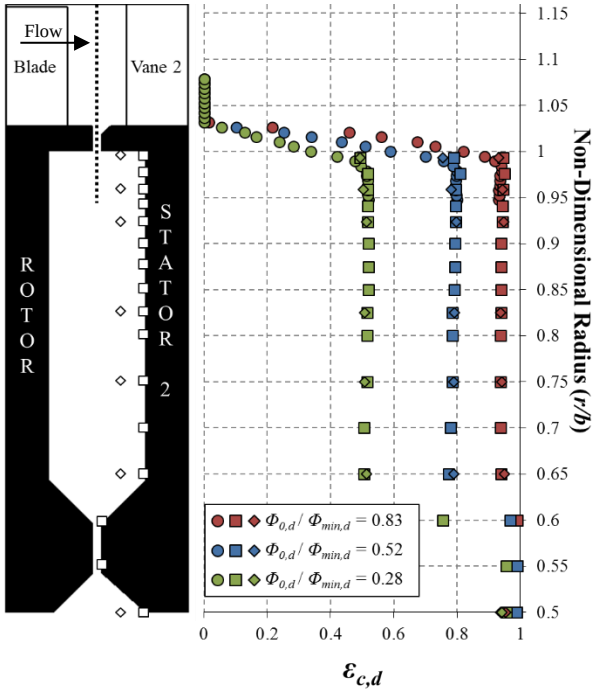

Figure 4-5: Effect of sealing flow rate on radial distribution of effectiveness in the downstream cavity ($Re\phi = 7.20 \times 10^5$ and CF = 0.34) (squares: wall; diamonds: core; circles: probe. By Scobie *et al.* (2017)

A similar test was conducted for a radial seal at different sealing conditions. Figure 4-6 shows the variation of concentration effectiveness ($\varepsilon_{c,u}$) across the annulus and within the seal clearance. The tests were conducted at difference sealing flow conditions. In the upstream, the sealing flow rate was $\Phi_{0,u} = \Phi_{min,u}$ (blue data). In the downstream, the unseeded sealing flow rate was $\Phi_{0,d} = \Phi_{min,d}$ (red data). The data symbols are geometrically aligned with the silhouette of the stage. The results showed significant re-ingestion, which decreases with increasing sealing flow rate ($\Phi_{0,d}$). The probe measurements are consistent with Figure 4-6; large mixing occurs near the rim seal mixing region, between the seeded upstream sealing flow and unseeded downstream sealing flow. The results in Figure 4-6 suggest that 1.8% ($\varepsilon_{c,u}$ = 0.018x100) of upstream egress is re-ingested into the downstream wheel-space, since only the upstream flow has concentration and this concentration is detected in the downstream wheel-space. Like the axial seal results, the radial seal effectiveness does not change with radius. For the case of $\Phi_{0,d} = \Phi_{min,d}$, the results show higher mixing near the seal clearance, compared to the case with no downstream sealing flow. Above the seal platform, the concentration does not vary significantly, for the two sealing flow cases, indicating only a mild interaction between the egress and mainstream.

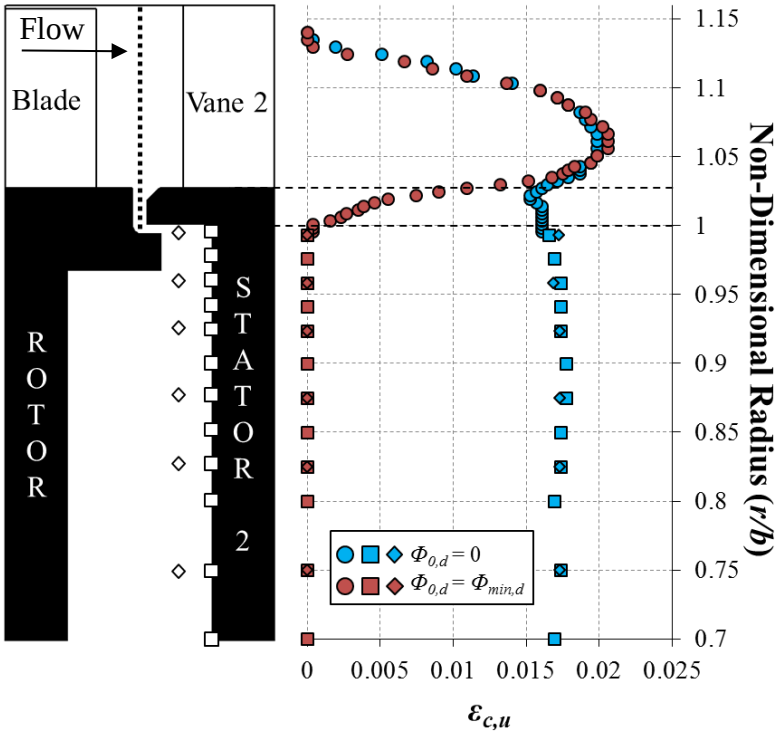

Figure 4-6: Effect of downstream sealing flow rate on radial distribution of effectiveness in the downstream annulus and wheel-space for $\Phi_{0,u} = \Phi_{min,u}$ (squares: stator-wall; diamonds: rotating-core; circles: probe measurements). By Scobie *et al.* (2017)

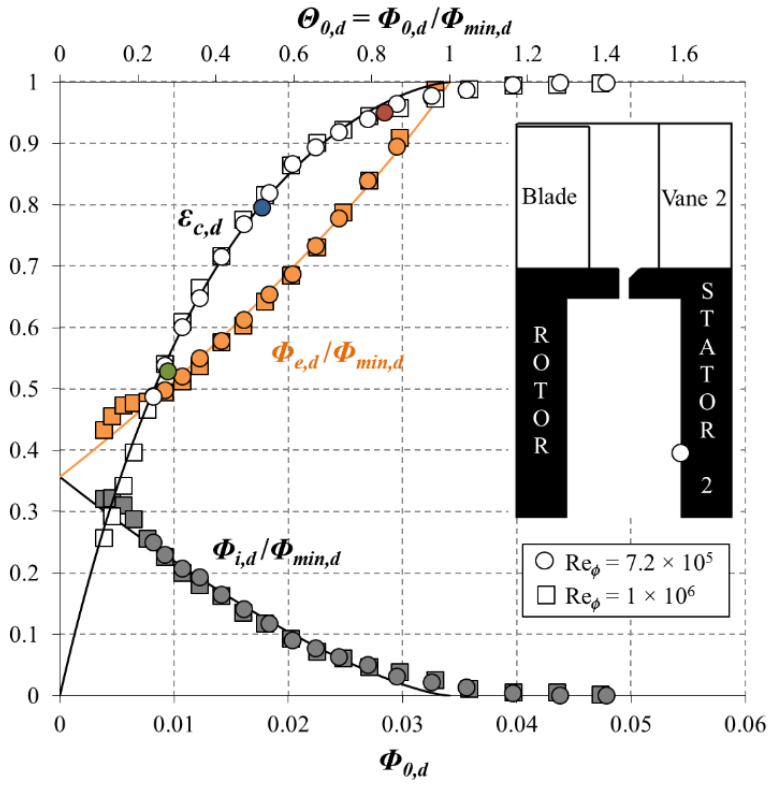

Figure 4-7: Variation of concentration effectiveness, ingress and egress flow ratios with non-dimensional sealing flow rate in the downstream wheel-space (Symbols denote data; lines denote theoretical model fits). By Scobie *et al.* (2017)

Concentration measurements for a range of non-dimensional sealing flows (Φ_0) are shown in Figure 4-7; measurements are taken at r/b = 0.85. The results reveal that the effectiveness ($\varepsilon_{c,d}$) increases with increasing Φ_0, which results in a reduction of ingress through the seal clearance. For all cases the results collapse onto a single curve, showing that the effectiveness of the seal is not dependent on rotational Reynolds number, Re_ϕ. Equation 4.3 calculates a theoretical effectiveness using a statistical fitting method, maximum likelihood estimation (Sangan *et al.* 2013). The theoretical effectiveness was fitted to the experimental data and the results are consistent, as shown in Figure 4-7 (solid lines). Data labels; green, blue and red represent the $\Phi_{0,d} / \Phi_{min,d}$ values for the three test cases.

Two other curves are presented in Figure 4-7, the non-dimensional ingress and egress to $\Phi_{min,d}$ ratios, calculated using Equations 3.4 and 3.5, respectively. The non-dimensional ingress and egress curves indicate the maximum ingested flow as a ratio of the minimum amount of sealing flow needed to prevent ingress. When there is no sealing flow ($\Phi_{0,d} = 0$) all the ingested mainstream must leave as egress, hence $\Phi_{i,d} = \Phi_{e,d}$, however when the wheel-space is fully sealed ($\Phi_{0,d} = \Phi_{min,d}$) all the sealing flow leaves as egress.

4.1.5 Circumferential Distribution of Effectiveness

The effectiveness asymmetry was measured in the annulus and across the seal clearance. Figures 4-8 and 4-9 present radial traverse measurements upstream and downstream of the rotor blades respectively. All tests were conducted at $\Phi_0 = \Phi_{min}$, hence with a fully sealed wheel-space ($\varepsilon_{c,u} = 1$), measured at location $r/b = 0.958$ (white circle). The results also show that, at $\theta = 0.189$ the highest effectiveness ($\varepsilon_{c,u}$) is produced, this suggests the probe measured near a location of minimum ingress, however at $\theta = 0.3$ the lowest effectiveness occurred, this suggests the probe measured near a location of maximum ingress. The results indicate that the distribution of effectiveness is dependent on the relative circumferential vane position (θ), for both upstream and downstream locations, Figures 4-8 and 4-9, respectively.

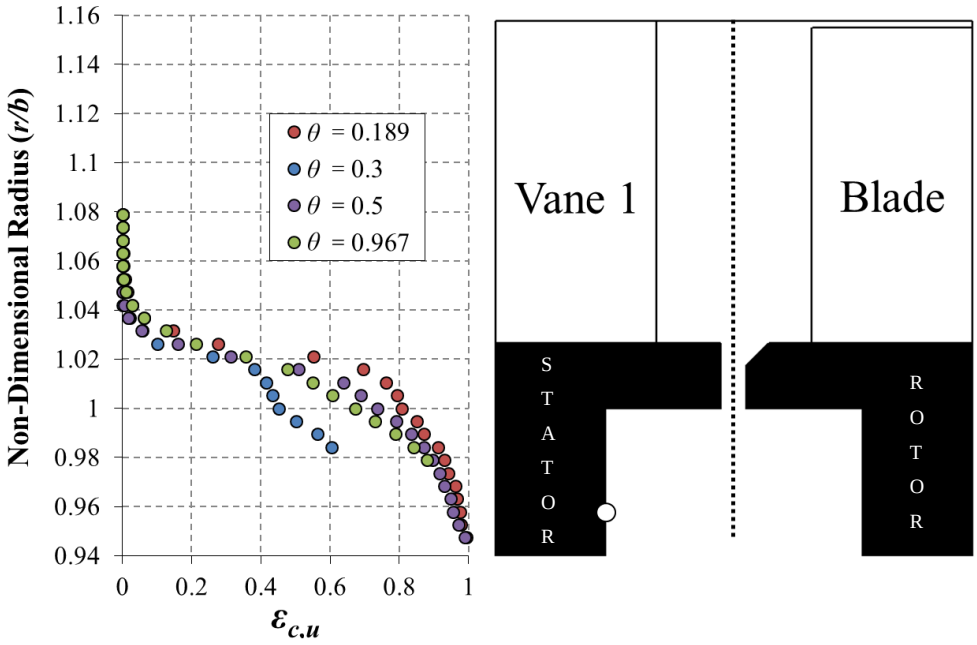

Figure 4-8: Radial traverse through upstream axial-clearance rim seal for four circumferential positions relative to upstream vane ($\Phi_{0,u} = \Phi_{min,u}$). By Scobie *et al.* (2017)

The results in Figure 4-9 show that across the seal clearance an asymmetric trend has been formed due to the circumferential pressure distribution. Furthermore, it was anticipated that the effectiveness asymmetry would be more noticeable in the upstream region due to a stronger circumferential pressure distribution ($\Delta C_{p,a}$), the distribution of effectiveness results supports this. For all four circumferential locations ($\theta = 0.189, 0.3, 0.5$ and 0.967) the effectiveness (ε_c) in the upstream annulus is virtually zero, it then increases across the rim seal-clearance and down into the wheel-space as the ingress and egress interact. At the non-dimensional radius, $r/b \sim 0.94$ in the upstream and $r/b \sim 0.98$ in the downstream, the effectiveness is virtually unity

(ε_c = 1) but a mismatch in concentration arises at the same measuring location of the probe and stator wall (white circle), r/b = 0.958. It must be noted that at some circumferential locations (θ = 0.3 and θ = 0.967) radial probe measurements were not possible for r/b < 0.98 due to restrictions in the experimental setup (traverse not long enough), however it is expected to reach ε_c = 1 at r/b = 0.94.

The results for the measurements downstream of the rotor blades (Figure 4-9) show similar mixing behaviour as in the upstream location (Figure 4-8), some differences involve the maximum and minimum effectives for each curve as well as the intensity of mixing in the seal clearance. It is evident that in the downstream seal clearance the mixing is more vigorous, and a steep rise in effectiveness is produced across the seal clearance; this may be caused by an axisymmetric curtain of egress that the ingress must cross before mixing with the ingested flow. The results also show that, at θ = 0.089 the lowest effectiveness ($\varepsilon_{c,u}$) is produced, this suggests the probe measured near a location of maximum ingress, however at θ = 0.422 the maximum effectiveness occurred, this suggests the probe measured near a location of minimum ingress.

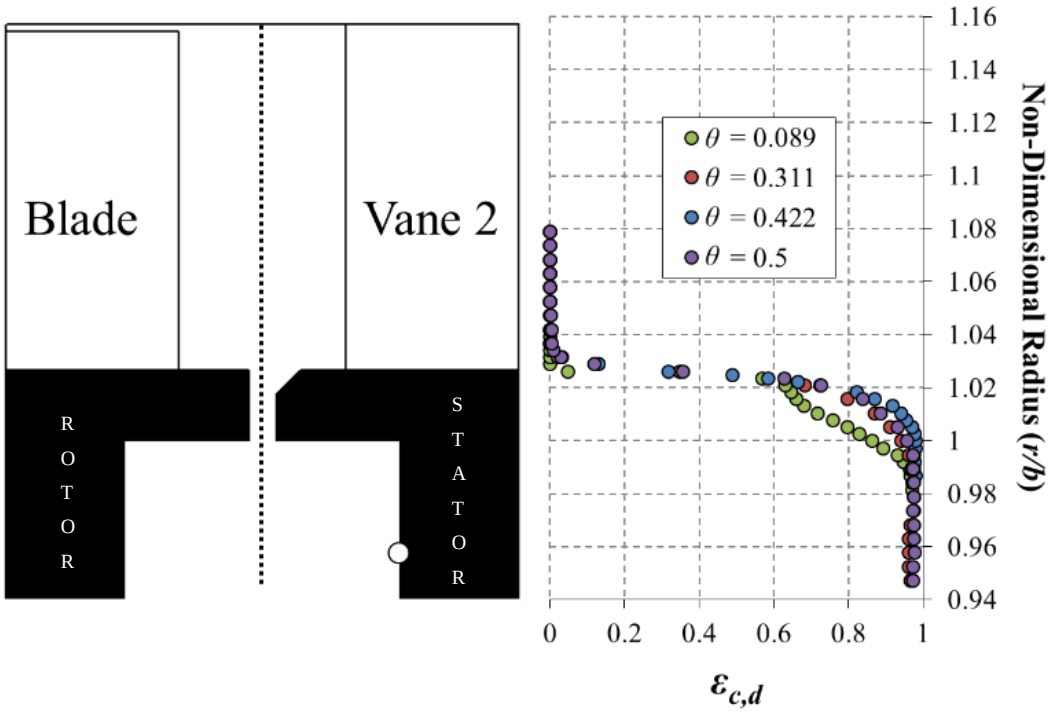

Figure 4-9: Radial traverse through downstream axial-clearance rim seal for four circumferential positions relative to downstream vane ($\Phi_{0,d}$ = $\Phi_{min,d}$). By Scobie *et al.* (2017)

4.1.6 Egress Concentration Measurements- Downstream Annulus

Figure 4-10 shows effectiveness data in the annulus at location A3. These measurements were taken with a fully sealed wheel-space, $\Phi_{0,d} = \Phi_{min}$. The results show strong mixing between the egress and mainstream; across the annulus a concentration profile exists that replicates a boundary-layer with thickness 0.15h ($1.027 \leq r/b \leq 1.046$) which suggests a film-cooling benefit on the stator platform. A maximum effectiveness of $\varepsilon_{c,d} = 0.2$ was measured at $r/b = 1.025$. As the traverse is displaced vertically up across the annulus the effectiveness decreases to zero, as a result of intense mixing in the annulus. Concentration measurements at A3 were measured at one circumferential position (θ) but it is expected that the effectiveness trend would vary at different circumferential positions.

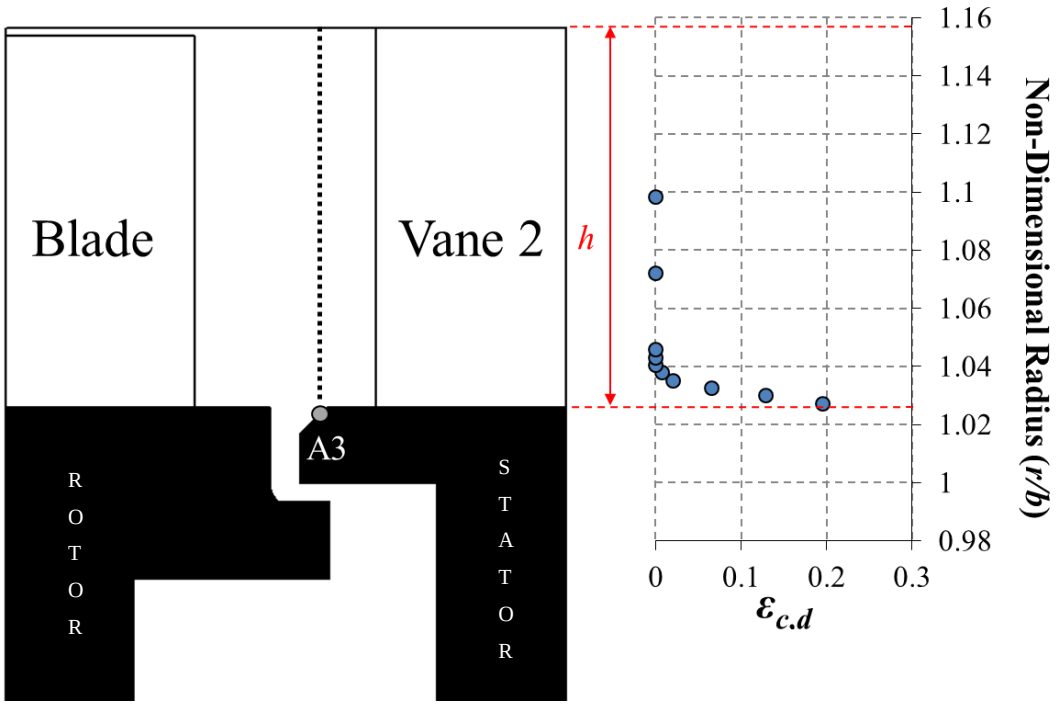

Figure 4-10: Radial distribution of effectiveness at the seal clearance ($\Phi_{0,d} = \Phi_{min,d}$ and $\theta = 0.42$). By Scobie *et al.* (2017)

The effectiveness ($\varepsilon_{c,d}$) and pressure asymmetry ($C_{p,a}$) was measured circumferentially at location A3 and is shown in Figure 4-11. The effectiveness data are distributed circumferentially across two vane pitches $0 < \theta < 1$ and $1 < \theta < 2$. Figure 4-11 demonstrates the uniformity of the annulus flow and repeatability of the measurements for the two vane pitches. The tests were conducted for four sealing flow-rates ($\Phi_{0,d} = 3\Phi_{min}$, $2\Phi_{min}$, Φ_{min} and $½\Phi_{min}$) and two rotational speeds (see Table 3-1).

The results demonstrate that the non-dimensional pressure, $C_{p,a}$, and effectiveness ($\varepsilon_{c,d}$) is virtually independent of Re_ϕ. Egress emerges from the downstream wheel-space with high concentration levels, it then mixes with the annulus flow which lessens the concentration; this mixing is strongest at high sealing flow velocity. Furthermore, the presence of the downstream vanes affects the static pressure in the mainstream annulus and creates asymmetry. The maxima of the pressure curves correspond to the stagnation streamline to the leading edge of the vane; a region of slow mixing flow (low velocity) that results in a maximum effectiveness. However, high velocity flow moves through a region of low-pressure (vane passage), away from the stagnation line, this causes high mixing and the effectiveness to decrease. Evidently, the results suggest that increasing the downstream wheel-space sealing flow, $\Phi_{0,d}$, and therefore the outflow of egress, increases the film cooling effect on the vane platform.

Overall the results show a conventional trend, however there are some data points that show anomalous behaviour and it is believed that the cause could be dust or dirt inside the pressure taps. This is something unavoidable and could not be internally cleaned.

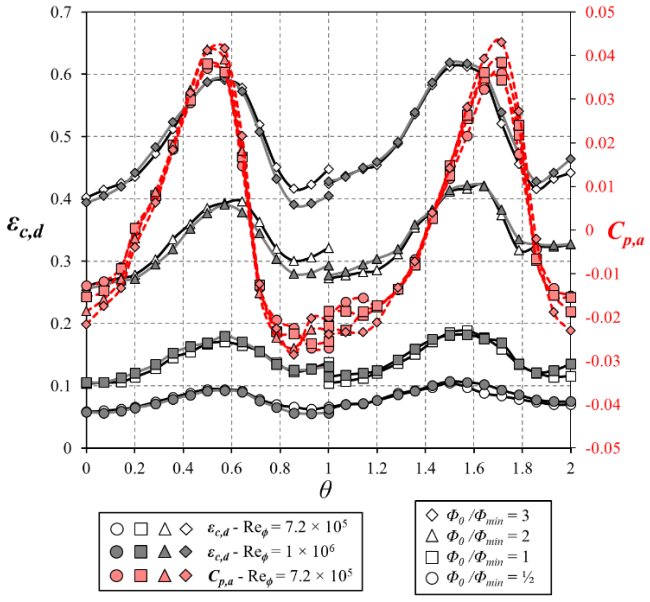

Figure 4-11: Variation of concentration effectiveness and pressure coefficient with non-dimensional vane pitch - location A3 (Scobie *et al*, 2017).

4.2 Summary

A novel experimental technique was developed in order to study the flow structure and interaction, in the annulus and across the seal mixing plane. The experimental set up consisted of a probe attached to a Vernier traverse, with clamping blocks and screws. For a given flow coefficient, the concentration profiles were invariant with rotational Reynolds number and followed the expected flow structure. The measurements showed an intense mixing region near the seal mixing plane, in the outer wheel-space. This study has shown for the first time, asymmetric variations of concentration to pierce through the seal mixing plane and into outer wheel-space. Re-ingested was detected, and large mixing occurred near the rim seal mixing region, between the seeded upstream and unseeded downstream sealing flow. The results suggested that 1.8% of upstream egress gets re-ingested into the downstream wheel-space. Chapter 7 will cover a complete study on re-ingestion.

The results reveal that egress can provide some film cooling benefits, on the vane and rotor platforms. Furthermore, the measurements acquired in this study provides new insight into the flow behaviour across the seal clearance and the interaction between egress and mainstream. It also offers quantitative data for CFD validation. The findings presented here could be used to help engine designers optimise the use of purge and improve engine efficiency.

Chapter 5: The Effect of Vanes and Blades on Ingestion

This chapter presents experiments and computations associated to the vane and blade interaction, and how it influences ingress. The effect of the vanes and blades on ingress can significantly decrease the performance of rim-seals. Figure 5-1 shows a typical rim seal configuration for a 1-stage rotor-stator system. A complex interaction occurs between the vanes and blades of a turbine, this creates a pressure variation which is unsteady and causes ingestion into the wheel-space of the turbine. To assess the effect the vanes and blades have on ingress, several configurations were investigated: the axial distance between the vane trailing-edge and the rim-seal was varied, and both a bladed and bladeless rotor were used. Studies have shown that unsteady pressure structures (large-scale flow structures) exist near the rim-seal region, in the presence or absence of vanes and blades. These pressure structures have been linked to Kelvin-Helmholtz instabilities or Taylor-Couette flow, both could influence ingress, due to the vortex generated by the shear layer interaction between the purge and tangential annulus flow. To investigate what effect large-scale structures has on ingress, the unsteady pressure field near the rim-sea l region was investigated. Chapter 2 identifies a gap in the literature regarding this problem.

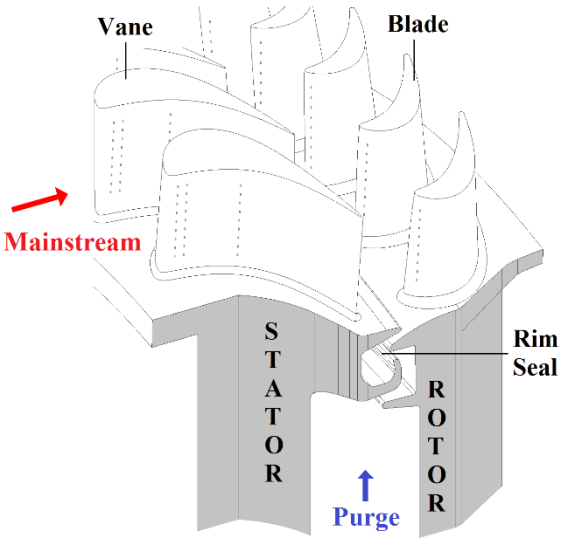

Figure 5-1: A generic high-pressure gas turbine stage with a rim-seal fitted at the periphery of the cavity (Hualca *et al*, 2019)

5.1 Experimental Setup

Experiments were conducted at two operating points, presented in Table 3-2. The experiments were conducted under engine representative values of λ_T. Incompressible flow exited the vanes. The speed of sound, density and air viscosity were calculated using the static temperature and pressure measured on the stator wall inside the upstream and downstream wheel-spaces at *r/b* = 0.958. Two vane configurations were tested. The first configuration, referred to here as vane-P1, was used previously by Patinios *et al.* (2017) and Horwood *et al.* (2018). The axial distance between the upstream edge of the rim-seal gap and vane trailing-edge was 5 mm. The second configuration, referred to here as vane-P2, is geometrically identical to vane-P1, however the axial location of the vane was moved 2.5 mm closer to the edge of the rim-seal. A double radial-clearance rim seal was installed in the upstream wheel-space, with dimensions given in Table 3-7. Silhouettes for two vane configurations are highlighted in red and blue (See Figure 5-2).

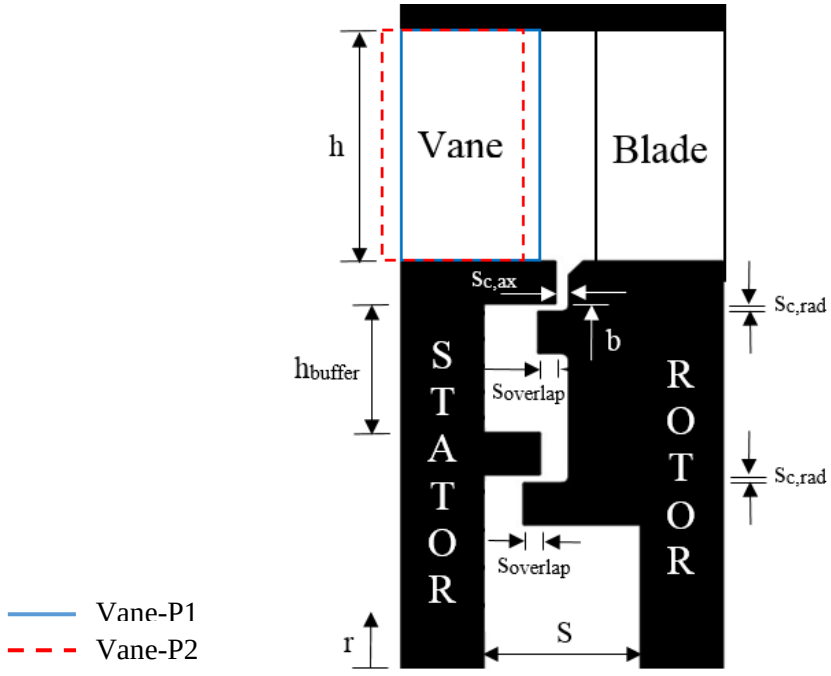

Figure 5-2: Double radial-rim seal configuration and vane configurations in the upstream wheel-space (Hualca *et al*, 2019)

5.2 Experimental Results

This section presents the distributions of pressure, swirl ratio and concentration effectiveness in the annulus and upstream wheel-space, for a range of sealing flow rates. The first section (5.2.1) compares experiments and time-averaged CFD computations of steady static pressure in the annulus; the computations were taken in the stationary and rotating domains. The computations were made using Reynolds-Averaged Navier-Stokes (URANS), with a finite-volume approach. A 22.5º sector was used, for a domain that comprised of a wheel-space alongside 2 vanes and 3 blades (bladed configuration only). Meshes were created using NUMECA. The second section (5.2.2) shows data for the variation of swirl ratio in both the inner and outer wheel-spaces. In the third section (5.2.3), the level of ingress into the upstream wheel-space is determined by gas concentration measurements. The final section (5.2.4) presents unsteady pressure data acquired at a location near the rim seal mixing plane.

5.2.1 Pressure Distribution in the Annulus

Pressure measurements were taken at locations A2(1) (red circle on silhouette) for vane-P1 and A2(2) (blue circle on silhouette) for vane-P2, as shown in Figure 5-3. The circumferential distribution of pressure in the annulus is compared for both vane configurations. The static pressure measurements are time-averaged. Circumferential measurements are taken 1.5 mm axially away from the edge of the seal, and colour-coded with reference to the silhouette. Figure 5-3 presents experimental data from two vane pitches, spaced over 180°; the first pitch ranges from $0 < \theta < 1$ at 0º and the second pitch ranges from $1 < \theta < 2$ at 180°.

The results show that the peak-to-trough pressure difference ($\Delta C_{p,a}$) for the vane set closest to the rim seal edge (vane-P2, blue colour vane) is larger than that of vane-P1 (red colour vane). The increase in peak-to-trough pressure occurs because the pressure has less time to decay axially. The pressure field downstream of the trailing vane decays with axial distance; a shorter distance gives the flow less time to decay, this makes vane-P2 possess higher magnitudes for the same axial location as vane-P1. Two rotational speeds were tested for the same operating flow coefficient, for both vane configurations, and he non-dimensional pressure distribution showed to be independent of Re_ϕ. The experiments and computations show good qualitative and quantitative agreement for $\Phi_0 = 0.03$, and other levels of sealing flow rate. Previous research on ingress found second-order effects of sealing flow (Φ_0) on pressure distribution, also termed the *spoiling effect*. The *spoiling effect* demonstrates that the increment of sealing flow rate weakens the peak-to-trough pressure difference (amplitude), as the sealing flow interacts with the mainstream. Though not presented here, Sangan *et al*.

(2013) demonstrates this spoiling effect which shows consistency with the findings of Bohn *et al.* (2006).

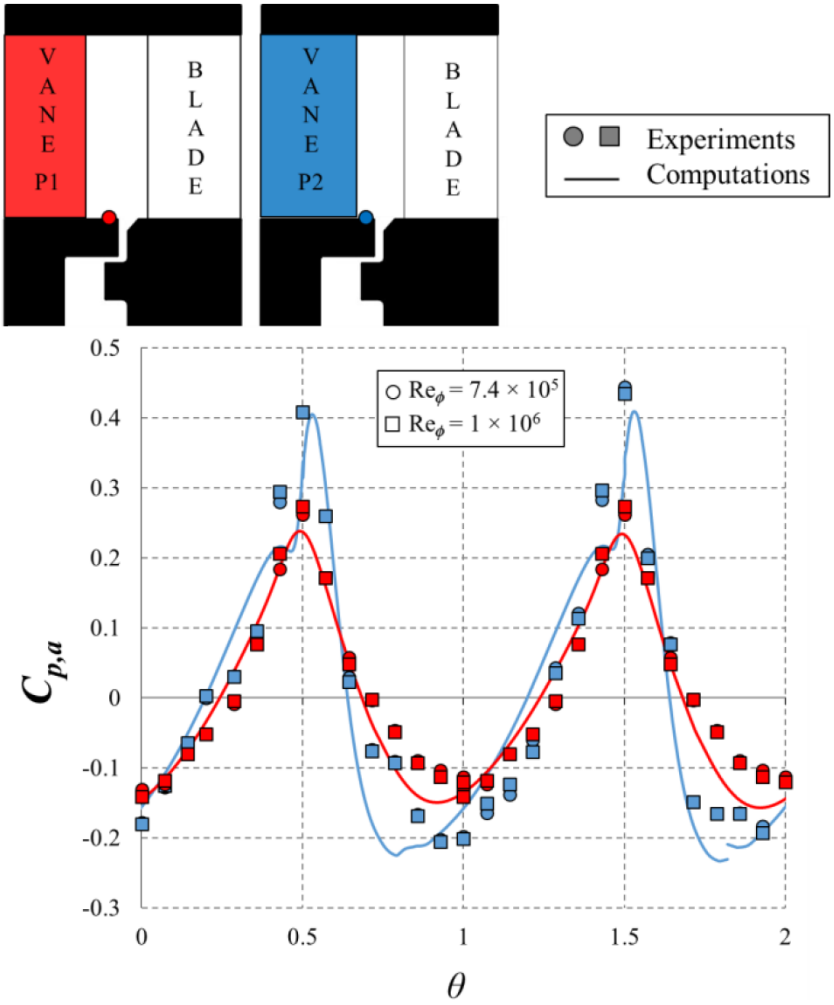

Figure 5-3: Circumferential distribution of steady pressure coefficient in the annulus over two non-dimensional vane pitches (Φ_0 = 0.03). Data are colour-coded with the silhouette (Hualca *et al*, 2019)

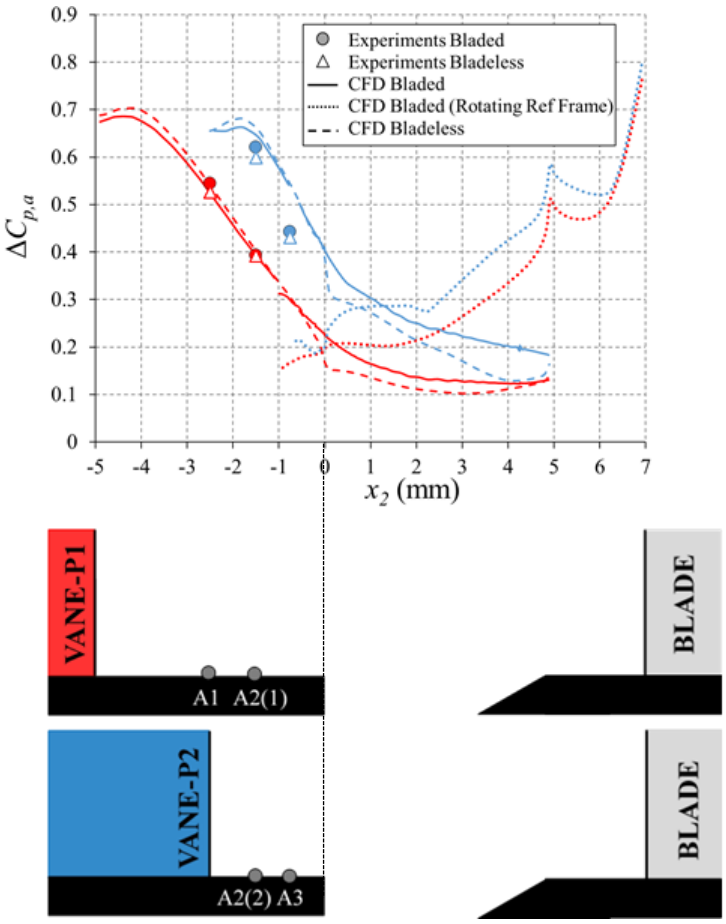

Figure 5-4: Axial variation of ΔC_p on the hub of the annulus centred from the rim seal leading edge, for bladed and bladeless rotor discs ($Re_\phi = 1\times10^6$, $\Phi_0 = 0.03$). By Hualca *et al.* (2019)

In Figure 5-4, the variation of $\Delta C_{p,a}$ is plotted for two vane positions (axial positions). The measurements were made across one vane pitch (15 data points) for each axial location and taken at a non-dimensional sealing flow parameter of $\Phi_0 = 0.03$. Note: In Figure 5-4 the x-axis is geometrically aligned with the silhouette of the rim seal; for both vane positions, starting with $x = 0$ at the leading edge of the rim seal. Experimental data are plotted for two distinct locations on the stator platform for a bladed (solid circles) and a bladeless (open triangles) configuration. Computations are presented for the entire vane-blade passage. The computational results include: $\Delta C_{p,a}$ in the stationary frame of reference (solid lines) and rotating frame of reference (dotted lines) both for a bladed case, and $\Delta C_{p,a}$ in the stationary frame of reference for a bladeless case (dashed lines); data are shown for both vane positions.

The results in Figure 5-4 show that for all cases (bladed and bladeless), the pressure difference, $\Delta C_{p,a}$, decreases with axial distance from the vane trailing edge. Furthermore, both the computations and experimental data show that the rotor blades do not have a significant effect on $\Delta C_{p,a}$ (the *steady* static pressure variation), in the stationary frame of reference. This

negligible effect occurs because the relative distance between flow field location and blade leading edge is not close enough to affect $\Delta C_{p,a}$. Data analysis showed that the absolute magnitudes of pressure (*p)* decreased with the bladeless rotor as the downstream blockage was reduced, however, when plotted in the non-dimensional form, $C_{p,a}$ was virtually the same for both bladed and bladeless cases. The computations in the rotating frame of reference revealed that $\Delta C_{p,a}$ was affected by the change in axial distance, relative to the blade leading edge. The effect on $\Delta C_{p,a}$ is significant in the rotating frame of reference because flow field ($x_2 > 0$) is closer to the leading edge of the blade. The dotted lines in Figure 5-4 represent unsteady pressure distribution, comparable to a circumferential pressure distribution that rotates with the blades. The computations of $\Delta C_{p,a}$ in the rotating frame of reference (dotted lines) show that the curves do not match. This indicates that the pressure distribution is dominated by the rotor blades. Evidently, the stationary frame of reference (solid lines) data validate computations for vane positions P1 and P2, but for $x_2 > 0$ in the rotating frame of reference, the $\Delta C_{p,a}$ values remain inconsistent. Previously it has been demonstrated that the local pressure across the rim seal is a key driver for ingress (Owen *et al.*(2014) and clearly difficult to compute.

In addition, the variation of $\Delta C_{p,a}$ at the outer casing of the annulus was also measured (See Figure 5-5). Experimental and computational results are plotted relative to the trailing edge of the vanes. The experiments validate the computations well. Once again, the effect of the blades on the pressure field is insignificant and all curves collapse. All configurations demonstrate a consistent trend of pressure distribution, with higher $\Delta C_{p,a}$ values for vane-P2, as seen in Figure 5-4. Furthermore, as expected, $\Delta C_{p,a}$ is seen to decay axially from the vane, indicating that the pressure field created by the vane dominates the driving potential for ingress.

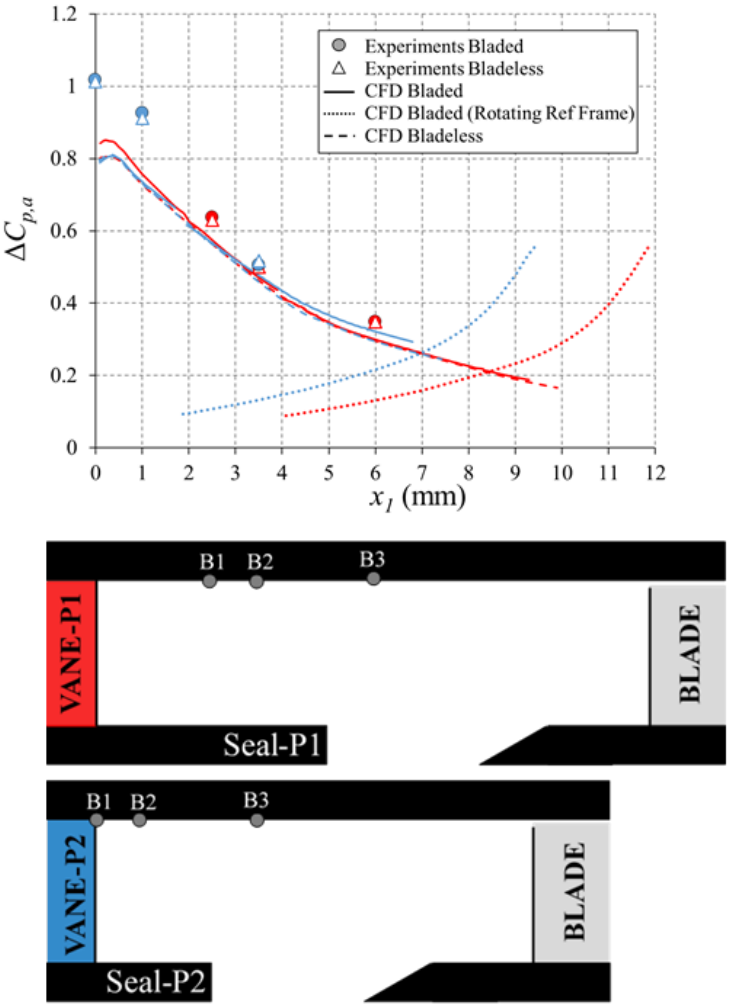

Figure 5-5: Axial variation of ΔC_p at the shroud of the annulus plotted from the vane trailing edge, for bladed and bladeless rotor discs ($Re_\phi = 1\times10^6$, $\Phi_0 = 0.03$). By Hualca *et al.* (2019)

5.2.2 Variation of Swirl Ratio with Sealing Flow in the Wheel-Space

Tangential swirl was measured at two locations: one in the inner (r/b = 0.825) and one in the outer (r/b = 0.993) wheel-space; these measurements were for a bladed case. For both vane positions, the variation of the swirl ratio, β (relative to the disc speed), is plotted in Figure 5-6 for a range of non-dimensional sealing flow rates. The measurement locations correspond to z/S = 0.25 and are shown on the silhouettes below.

The results show that the swirl ratio is higher in the outer wheel-space (near the outer seal) compared to the inner wheel-space, over the full range of sealing flow rates tested. Furthermore, the tangential velocity gets suppressed with increasing sealing flow, resulting in a reduction of β, as demonstrated in Figure 5-6. In the inner wheel-space the swirl ratio is not affected by the shift in vane position and is consistent with the outer wheel-space results, in that β decreases with sealing flow. Although the inner wheel-space shows consistent results,

there are a few anomalous data points ($0.14 < \Phi_0 < 0.17$) that show unconventional behaviour. This irregularity in the swirl is the error between the total and the static pressure. At high sealing flow rates, the total and static pressure become virtually identical and it is difficult for the pressure transducer to capture these small differences in pressure. The outer wheel-space displays an inflexion between $0.03 < \Phi_0 < 0.08$ for both vane configurations, demonstrating a significant influence of the vane translation. However, away from the inflexion the curves collapse on each other, demonstrating an insensitivity to vane position.

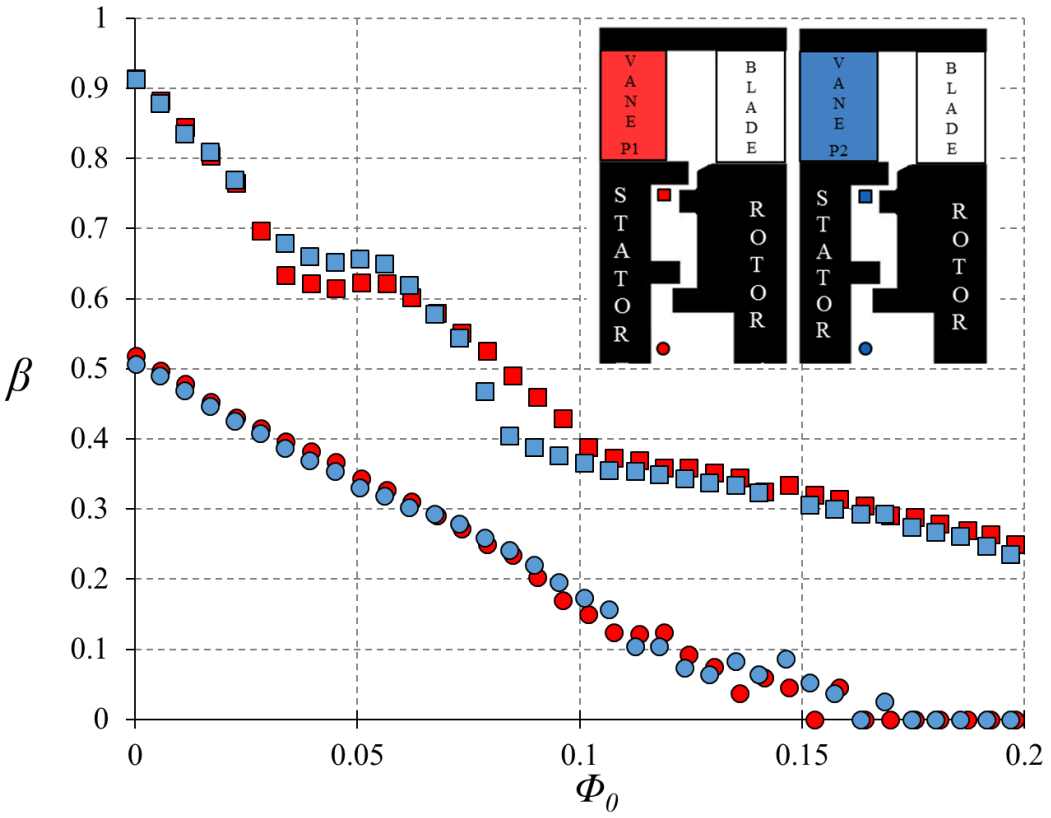

Figure 5-6: Measured variation of swirl ratio with non-dimensional sealing flow rate at *r/b* = 0.993 (squares) and *r/b* = 0.825 (circles), for two vane positions with rotor blades ($Re_\phi = 7.4\times10^5$). By Hualca *et al.* (2019)

In contrast to Figure 5-6 the results plotted in Figure 5-7 show swirl ratio measurements for a bladeless case; in these experiments the vane was positioned at P2. The solid symbols are reproduced from Figure 5-6 and the open symbols represent measurements for the bladeless case. In the inner wheel-space, data for the bladed and bladeless cases collapse, indicating no effect of the blades on the swirl ratio. However, there is a difference in swirl ratio for the outer wheel-space, where data for the bladeless rotor show no inflexion. On the bladed case an inflexion is present, demonstrating a discontinuous region, this translates to a

sharp increase in β which results in an increase on ingress, due to high-swirling flow from the annulus. The presence of the blade clearly affects β, for sealing flow-rates $0.03 < \Phi_0 < 0.08$, but as more sealing flow is introduced it gains enough momentum and overcomes this discontinuous region; the data collapses onto the bladeless data for sealing flow-rates $\Phi_0 > 0.08$. The occurrence of this inflexion could be caused by flow instabilities, linked to kelvin Helmholtz flow structures. This phenomenon is studied further in Chapter 5.2.4. When the wheel-space is fully sealed ingress is completely prevented and the effect of this instability cannot be observed. For sealing flow-rates blow, $\Phi_0 < 0.03$, the flow conditions are not affected due to insufficient egress momentum.

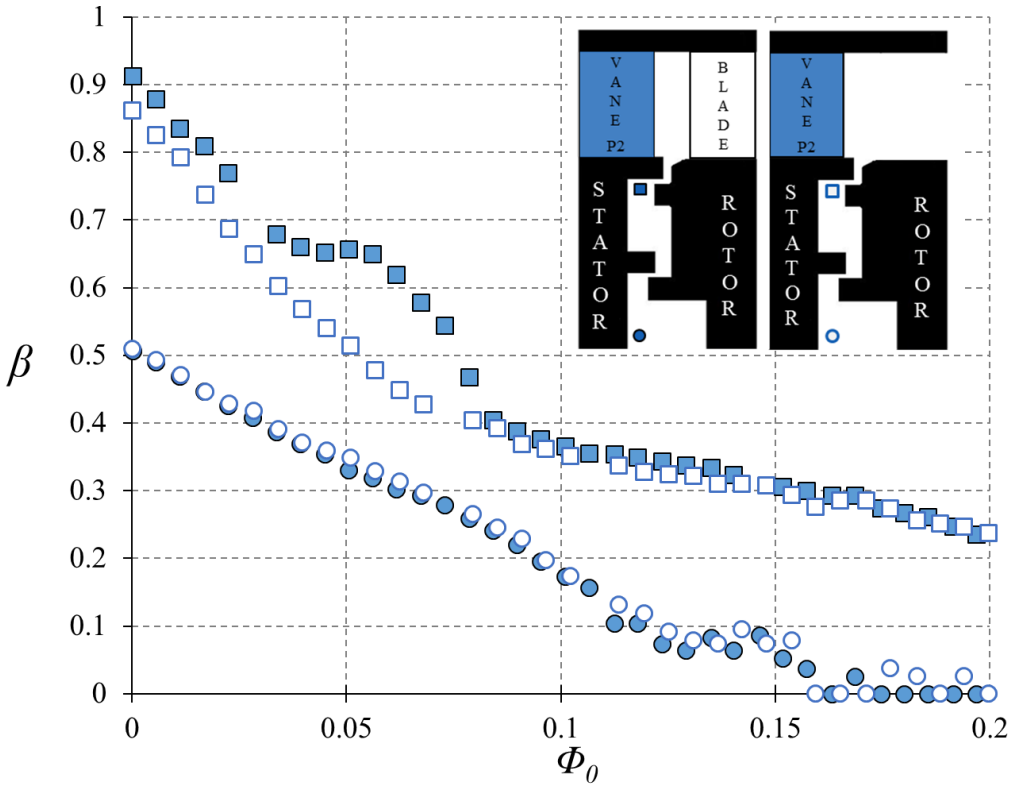

Figure 5-7: Measured variation of swirl ratio with non-dimensional sealing flow rate at *r/b* = 0.993 (squares) and *r/b* = 0.825 (circles), for bladed (solid symbols) and bladeless (open symbols) rotor discs ($Re_\phi = 7.4\times10^5$). By Hualca *et al.* (2019)

5.2.3 Gas Concentration Measurements

The distribution of concentration effectiveness with sealing flow, Φ_0, is presented in Figure 5-8 for two vane configurations and a bladed rotor disc. Measurements of concentration were made on the stator wall at r/b = 0.85 (inner wheel-space) and 0.958 (outer wheel-space). The results demonstrate that the effectiveness, ε_c, increases with sealing flow, and when the effectiveness reaches unity the wheel-space is fully pressurised, and no ingress occurs. Measurements were taken at two engine operating speeds and the results show that the variation of effectiveness with sealing flow is independent of Re_ϕ. Although Figure 5-8 shows only two engine operation speeds, other rotational speeds were tested, and the results were consistent. An inflexion occurs at similar sealing flow-rates as in Figure 5-7 (Section 5.2.2), $0.03 < \Phi_0 < 0.07$, for both vane configurations. However, the inflexion for vane-P2 is more noticeable and does depend on vane position.

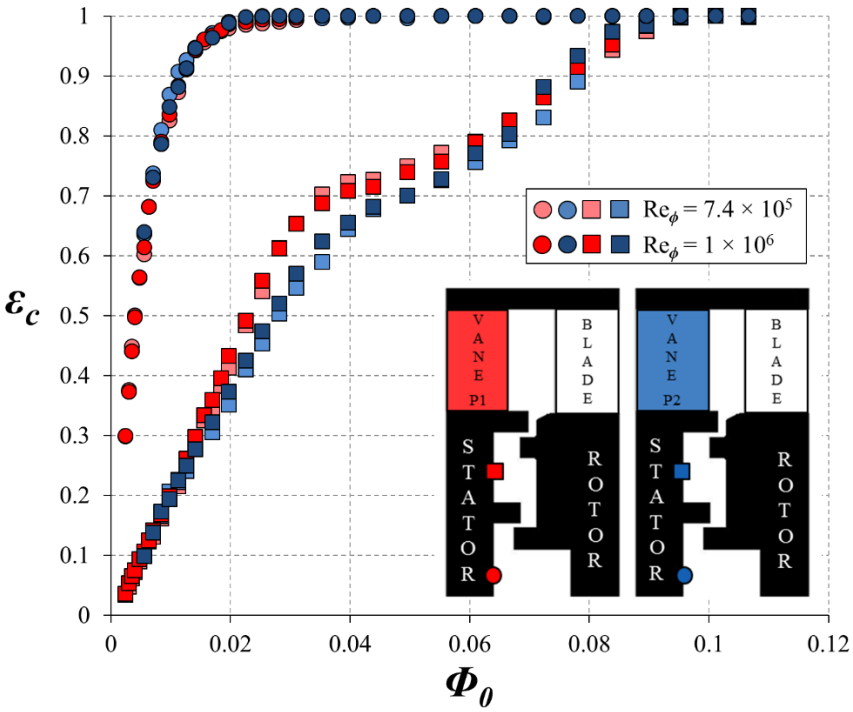

Figure 5-8: Variation of sealing effectiveness with non-dimensional sealing flow rate at r/b = 0.958 (squares) and r/b = 0.85 (circles), for two vane positions with rotor blades. By Hualca *et al.* (2019)

In the inner wheel-space, the sealing effectiveness curves are consistent with previously published experimental data (Sangan *et al*. 2012) but in the outer wheel-space an inflexion occurs, for both vane configurations (Figure 5-8). These inflexions are independent of Re_ϕ. Inflexions have been found by Horwood *et al.* (2018) for the same configuration as vane-P1, and traces of unconventional curves have been published by Boudet *et al.* (2005),

Gentilhomme *et al.* (2003) and Clark *et al*. (2016), however an explanation for these inflexions was not presented by the authors.

In the outer wheel-space, the sealing effectiveness curves do not collapse on each other, for sealing flow-rates $0.03 < \Phi_0 < 0.08$. The same sealing flowrates were used for both vane configurations, this was controlled by a high precision mass flow controller (Table 3-9). The axial shift in vane position (vane-P2) clearly influences the outer wheel-space. Vane-P2 is nearest to the rim seal leading edge and produces higher levels of ingress into the wheel-space. Considering the peak-to-trough pressure difference ($\Delta C_{p,a}$) is the main driver of ingress; the pressure asymmetry caused by the presence of the vanes, then the concentration measurements are consistent with the experiments and computations of $\Delta C_{p,a}$, presented in Figure 5-4. In contrast to the outer wheel-space, the inner-wheel-space is not affected by vane position and the fluid dynamics is controlled by rotationally-induced ingress, rather than externally-induced ingress.

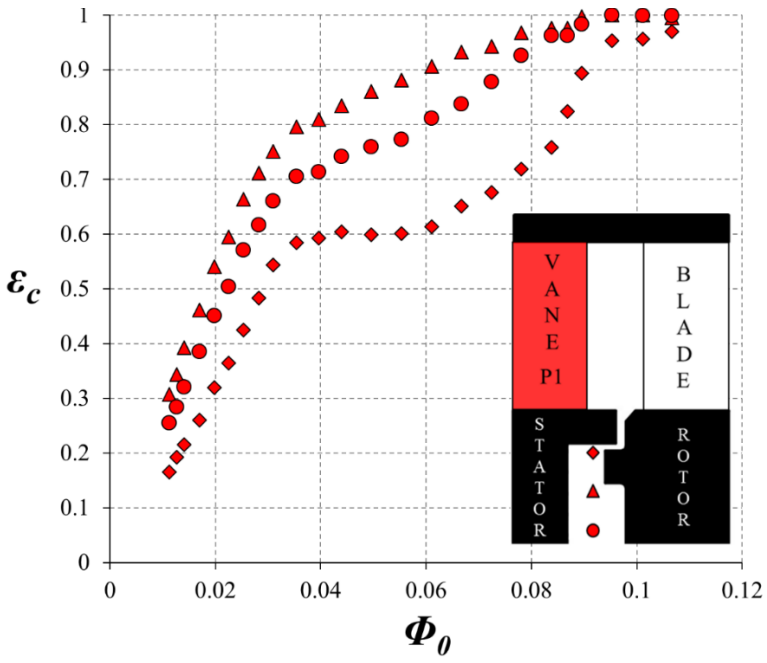

Figure 5-9: Effectiveness measurements in the core of the outer wheel-space at three radial locations: diamonds (r/b = 0.993), triangles (r/b = 0.958) and circles (r/b = 0.924). By Hualca *et al.* (2019)

To study further the inflexion phenomena shown in Figure 5-8, measurements of concentration were made in the core (z/s=0.25) at three radial locations: r/b=0.993, r/b=0.958, r/b=0.924; data here are presented for vane-P1 (see Figure 5-9). The results demonstrate that the inflexion is more pronounced near the seal clearance, just below the edge of the seal at r/b=0.993. Clearly a correlation exists between the corresponding swirl (Figure 5-6) and

concentration (Figure 5-8) measurements; all displaying an inflexion between the range of $0.04 < \Phi_0 < 0.08$. Section 5.2.4 discusses how unsteady pressure fluctuations are measured within the sealing flow-rates $0.02 < \Phi_0 < 0.104$.

Horwood *et al.* (2018) found a similar pattern in the radial distribution of core effectiveness and demonstrated that ε_c, at r/b = 0.958, is affected by high-concentration fluid which is pumped radially outwards from the rotor boundary layer. The author's computations did not show an inflexion in the effectiveness but hypothesised that the inflexion in the experiments is linked to large scale flow structures. Horwood *et al.* (2018) concluded that the CFD was not able not capture the inflexion in the experimental data between $0.05 < \Phi_0 < 0.08$, as the turbulence model was not accurate enough to capture the discontinuity on effectiveness.

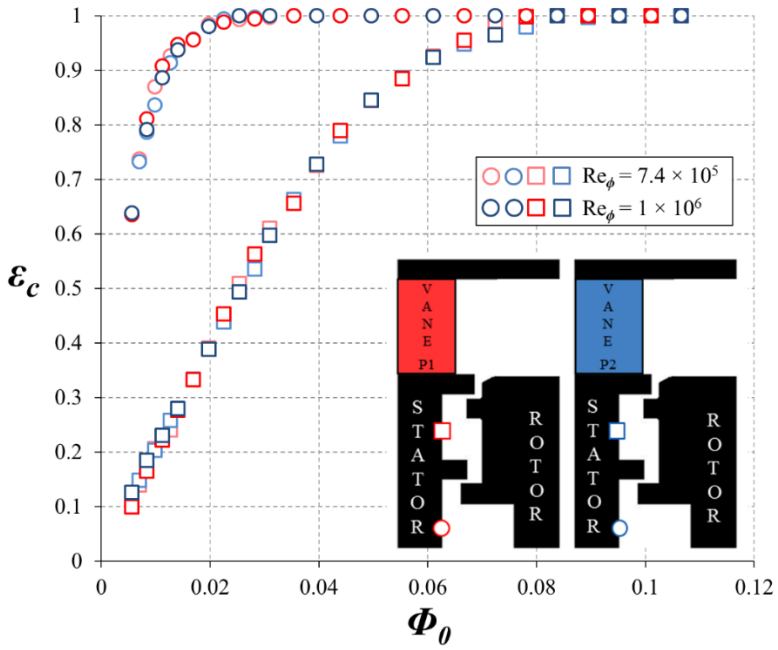

Figure 5-10: Variation of sealing effectiveness with non-dimensional sealing flow rate at *r/b* = 0.958 (squares) and *r/b* = 0.85 (circles), two vane positions without rotor blades. By Hualca *et al.* (2019)

In order to understand what influences the inflexion phenomena found in the swirl (Figure 5-6) and concentration (Figure 5-8) plots, the sealing effectiveness was measured for both vane configurations, in the absence of blades. The results (Figure 5-10) show that ingress in the inner and outer wheel-spaces is independent of rotational speed and vane position, suggesting that $\Delta C_{p,a}$ does not change. Furthermore, in the absence of the rotor blades the inflexion disappears for both vane configurations. The results therefore show clear evidence that the inflexion is caused by a vane and blade interaction.

The results in Figure 5-10 challenges previous findings from Chew *et al.* (1994). Experiments from Chew *et al.* (1994) showed that in the absence of blades, the peak-to-trough pressure difference ($\Delta C_{p,a}$) is affected by vane position. Ingress is dominated by $\Delta C_{p,a}$, therefore different $\Delta C_{p,a}$ values would produce different levels of ingestion, but Figure 5-10 shows virtually identical ingestion for both vane configurations. Owen (2011) proposed a model that predicted the externally-induced ingress to be proportional to $\Delta C_{p,a}^{1/2}$, but Figure 5-8 shows that for sealing flow-rates Φ_0 = 0 - 0.02 and Φ_0 = 0.07 - 0.104, the effectiveness is not affected by the different $\Delta C_{p,a}$ values produced by the two vane configurations (Figure 5-4). This challenges the model proposed by Owen (2011), as at certain sealing flow-rates ingress is not affected by $\Delta C_{p,a}$.

The results in this section suggest that ingress might not be driven only by the peak-to-trough pressure difference, but also by other complex flow behaviour near the seal clearance mixing plane. The following section will study the unsteady flow behaviour near the seal mixing.

5.2.4 Measurements of Unsteady Pressure

Experimental measurements of unsteady pressure were recorded for five purge flow rates, Φ_0 = 0.02, 0.03, 0.05, 0.078 and 0.104, for the two vane configurations with and without blades. These measurements were taken on the stator wall (r/b = 0.993) near the rim seal in order to assess the presence of rotating flow structures, discussed in Chapter 2. The effect of large scale flow structures on ingress has not been thoroughly studied, and this experiment aims to investigate the effect of rotor blades and vane position on these instabilities.

Fast Fourier Transformations (FFTs) of unsteady pressure are plotted in Figure 5-11 and Figure 5-12, for $Re_\phi = 7.4\times10^6$. Horwood *et al.* (2018) measured unsteady pressure for vane-P1 and plotted FFTs for a range of non-dimensional sealing flows (see Table 5-1). The data are reproduced in Figure 5-11 along with FFTs of unsteady pressure for vane-P2. In Figure 5-11, the x-axis shows the non-dimensional frequency, (f / f_d), where f_d is the disc rotation frequency; the y-axis shows the non-dimensional pressure coefficient, C_p - see nomenclature.

Beard *et al.* (2017) used a phase analysis method to calculate the number of rotating flow structures (N). The same phase analysis method was used here with signals acquired from two unsteady pressure transducers separated by 8° (α) circumferentially. The number of flow structures (N) and their rotational speed relative to the disc (ω/Ω) is presented in Table 5-1 for the bladed rotor, and Table 5-2 for the bladeless rotor.

The unsteady pressure transducers acquired measurements over 10 seconds at a sampling frequency of 100 kHz. This sampling frequency corresponds to a Nyquist frequency of 50 kHz; therefore, an anti-aliasing filter of 50 kHz was installed in the data acquisition system to prevent distortion or error in the signals. The signals from the two transducers were cross-correlated to determine the lag time (Δt_α) and rotational speed ($\omega = \alpha / \Delta t_\alpha$).

Figure 5-11 illustrates FFTs for two vane configurations for the case with a bladed rotor. For all FFTs a constant normalised frequency (f / f_d) of 48 exists and corresponds to the blade passing frequency (BPF). The strength of the BPF varies with increasing sealing flow rate. The FFT was expected to give a dense spectrum of frequencies but instead it produced a spread of several distinct frequencies. A hypothesis for the spread is that the number of structures switch between integer values, thus producing several distinct frequencies. The analysis showed that the number of flow structures vary between $22 < N < 28$. The vane configuration and sealing flow rate did not significantly influence the number of flow structures. The number (N) and speed (ω/Ω) of the flow structures are presented in Table 5-1. The speed of the flow structures was between $0.96 < \omega/\Omega < 1.12$. A flow structure can rotate faster than the disk speed (Ω) when, the swirl ratio is β_a=1.6 downstream of the vanes.

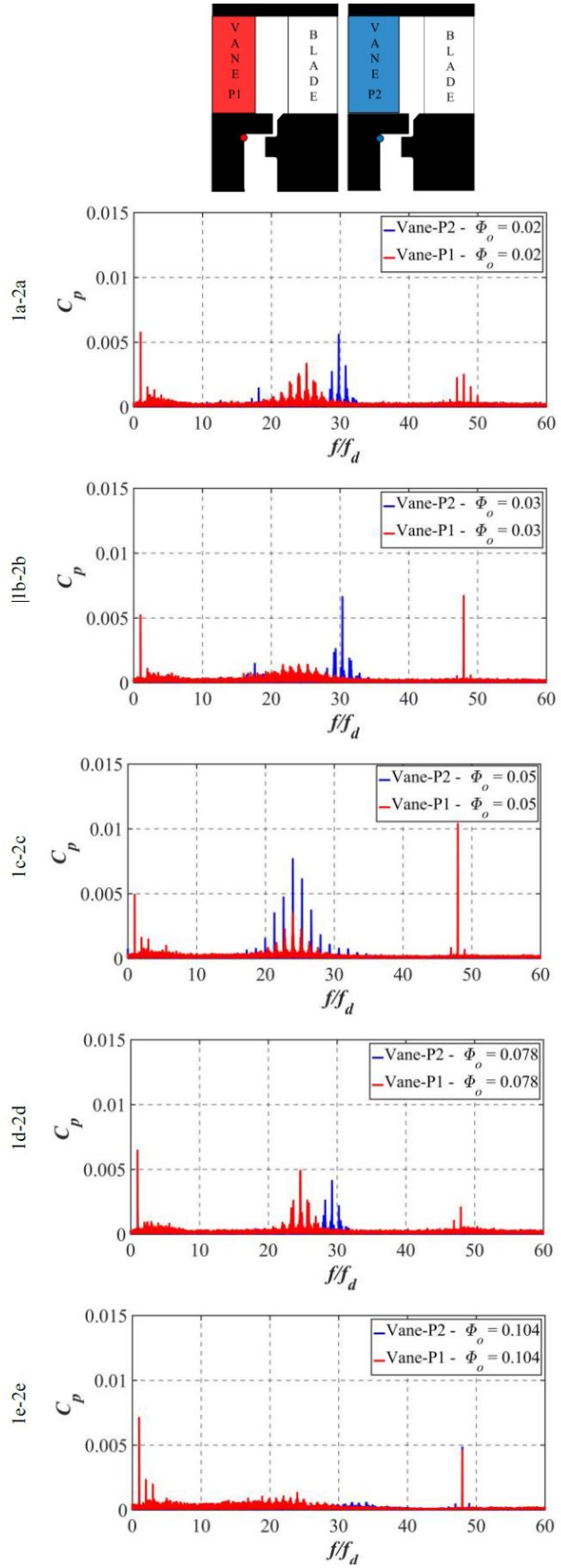

Figure 5-11: Fast Fourier Transforms of unsteady pressure data at *r/b* = 0.993 on the wheel-space stator wall, for two vane positions with rotor blades ($Re_\phi = 7.4\times10^5$). By Hualca *et al.* (2019)

For the two vane configurations the FFTs shown in Figure 5-11 demonstrate that two distinct frequencies occur at f / f_d ~24 and f / f_d ~30, for Φ_0 = 0.02 and Φ_0 = 0.03. However, at Φ_0 = 0.05 the magnitude of these frequencies increases and collapse on top of each other at precisely f / f_d = 24, which corresponds to half the number of blades of the rotor disk. For the high sealing flow-rate of Φ_0 = 0.078, again two distinct frequencies occur at f / f_d ~24 and f / f_d ~30, for each vane configuration but when the wheel-space becomes fully sealed at Φ_0 = 0.104 the spectral activity virtually disappears for both vane configurations. Evidently the formation of the structures is closely linked to the presence of the blades. The behaviour of the structures is influenced by the sealing flow-rate and the unsteady pressure field from the blades; specifically, at the inflexion region (Figure 5-6 and 5-8). A critical sealing flow rate (Φ_0 = 0.05) exists, where the number of flow structures (N) become half the blade count and the rotational speed becomes unity.

It is speculated that the magnitude of these low pressure structures gets reinforced by synchronous superposition of the unsteady pressure field created by the blades. This effect results in lower effectiveness and increasing swirl in the wheel-space. Note the annulus swirl ratio is βa = 1.6.

	Rotor Speed (RPM)	Non-dimensional Sealing Parameter (Φ_0)	Number of Structures (N)	Rotational speed of Structures (ω/Ω)
Vane P1				
Experiment	3000	0.020	26	0.96
Experiment	3000	0.030	26	0.92
Experiment	3000	0.050	23	1.03
Experiment	3000	0.078	26	0.94
Experiment	3000	0.104	N.A.	N.A.
Vane P2				
Experiment	3000	0.020	26	1.10
Experiment	3000	0.030	28	1.12
Experiment	3000	0.050	24	0.99
Experiment	3000	0.078	22	0.94
Experiment	3000	0.104	N.A.	N.A.

Table 5-1: Comparison of large-scale flow structures, for two vane positions with rotor blades

FFTs for a bladeless case are shown in Figure 5-12, for two vane configurations. The same sealing flow-rates as in Figure 5-11 were used, but only one pronounced frequency was visible; at $f / f_d = 31$ for vane-P1 and $f / f_d = 28$ for vane-P2. The results suggest that the number of flow structures is influenced by the blade potential field. In contrast to the bladed FFTs where the signals were divided over several frequencies, in the absence of blades, the energy of the signals is concentrated into one distinct frequency, resulting in a large value of C_p. The calculations demonstrate that the number structures range from $34 < N < 40$, with a speed of $0.71 < \omega/\Omega < 0.89$. Table 5-2 shows results for the bladeless case with two different vane configurations. The results show that in the absence of blades the flow structures increase in number and rotate at lower speeds when compared to the bladed case. Furthermore, the flow-structures for vane-P2 rotate slower than that of vane-P1. The unsteady data points toward two fundamental driving mechanisms, large-scale structures that possibly arise from Taylor-Couette or Kelvin-Helmholtz instabilities. These could influence the fluid behaviour near the rim-seal region. The blade-vane interaction supresses the magnitude of the structures and changes the frequency.

	Rotor Speed (RPM)	**Non-dimensional Sealing Parameter (Φ_0)**	**Number of Structures (N)**	**Rotational speed of Structures (ω/Ω)**
Vane P1				
Experiment	3000	0.020	34	0.89
Experiment	3000	0.030	36	0.85
Experiment	3000	0.050	37	0.82
Experiment	3000	0.078	39	0.79
Experiment	3000	0.104	39	0.79
Vane P2				
Experiment	3000	0.020	37	0.74
Experiment	3000	0.030	38	0.73
Experiment	3000	0.050	38	0.73
Experiment	3000	0.078	40	0.70
Experiment	3000	0.104	39	0.71

Table 5-2: Comparison of large-scale flow structures, for two vane positions without rotor blades

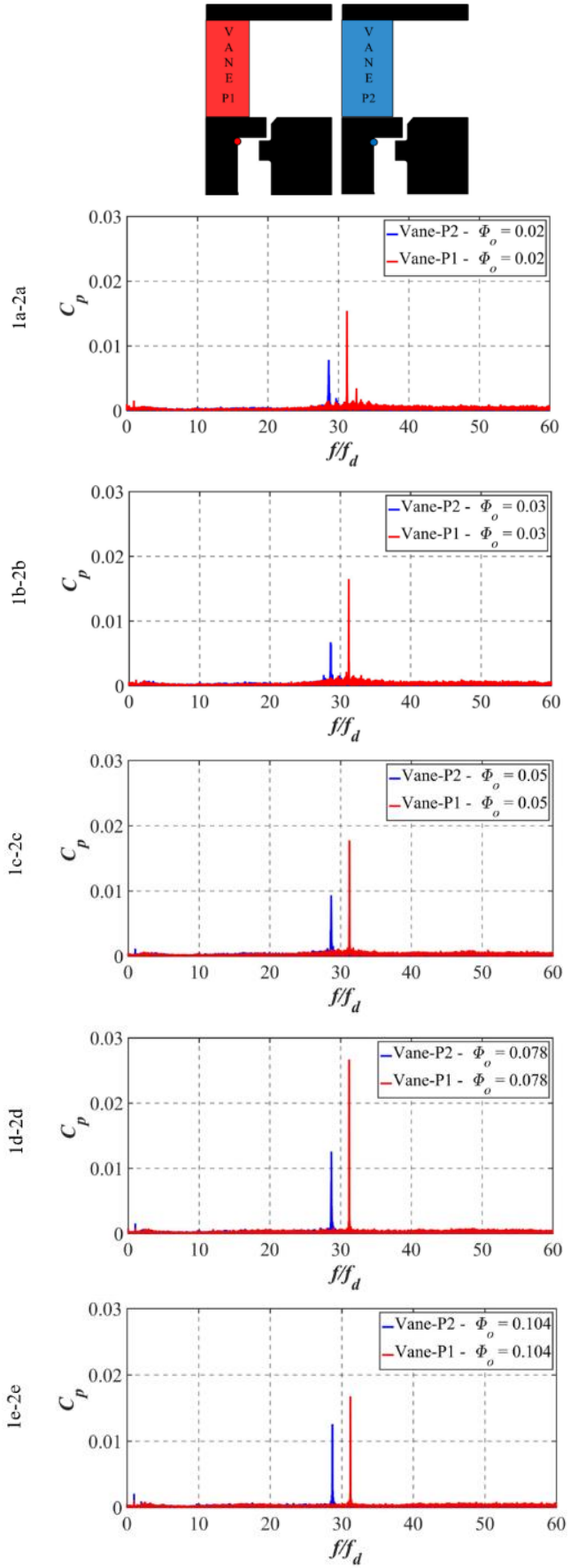

Figure 5-12: Fast Fourier Transforms of unsteady pressure data at *r/b* = 0.993 on the wheel-space stator wall, for two vane positions without rotor blades, ($Re_\phi = 7.4\times10^5$) , (Hualca *et al*. 2019)

5.3 Summary

The effect of vanes and blades on ingress was investigated. Four configurations were investigated, two vane positions and two rotor discs. Circumferential distribution of pressure was measured in the annulus, the measurements were validated by computations. Both, experiments and computations demonstrated that rotor blades do not have a significant effect on $\Delta C_{p,a}$, on the stator side of the annulus. However, $\Delta C_{p,a}$ is significantly affected by the vane proximity, relative to the to the rim seal edge.

Ingress was quantified with gas concentration measurements in the inner and outer wheel-spaces, for two vane positions and two rotor discs. The sealing effectiveness for the inner wheel-space followed a conventional trend, for both vane configurations. However, an inflexion occurred in sealing effectiveness of the outer wheel-space, for a sealing flow rate range of $0.03 < \Phi_0 < 0.08$. The inflexion region was affected by vane position. The inflexion disappeared in the absence of the blades. The inflexion is clearly linked to the presence of the blades.

Unsteady pressure measurements were made a for bladed and bladeless configuration in the outer wheel-space, near the seal mixing plane. The results revealed the existence of large-scale pressure structures (flow instabilities), these were affected by the vane position and sealing flow rate. The flow structures rotated at a speed close to the rotor speed, for all cases. A critical sealing flow rate was found, that produced a distinguishable frequency at precisely half the blade count, for both vane configurations.

Chapter 6: Flow Instabilities in Gas Turbine Chute Seals

This chapter presents experiments and computations of flow through a gas turbine chute seal (Figure 6-1). The study investigates the phenomena of flow instabilities. Flow instabilities arise from Kelvin-Helmholtz or Taylor Couette flow. The aim of this chapter is to study the steady and unsteady flow features and pressure field, near the rim seal mixing plane. A geometrically scaled vane, blade and chute seal geometry is tested. The results presented here form part of a future work with KTH Royal Institute of Technology. KTH will study the effect of engine scaling, which consists on increasing the engine size and flow conditions (Mach number). Experiments and computations for pressure, swirl and sealing effectiveness were done at engine representative values of λ_T. The computations were conducted by Joshua Horwood (Horwood *et al.* 2019).

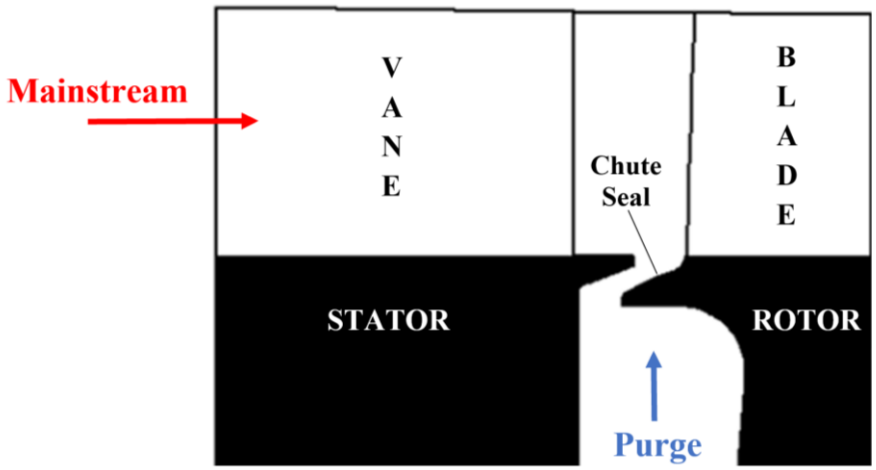

Figure 6-1: A generic high-pressure gas turbine stage with a chute seal fitted at the periphery of the cavity

6.1 Experimental Setup

Experiments and computations were conducted at two operating points under sub-sonic flow conditions, presented in Table 3-3. The speed of sound, density and air viscosity were calculated using the static temperature and pressure measured on the stator wall inside the upstream and downstream wheel-spaces at r/*b* = 0.958. A chute rim seal was installed in the upstream wheel-space, with dimensions given in Table 3-8. The test section was instrumented with static and total pressure probes as well as fast-response pressure transducers. The

stationary disc included 48 stacked vanes and the rotor disc comprised of 60 turned and twisted blades. The periphery of both discs formed a chute seal (Figure 6-2).

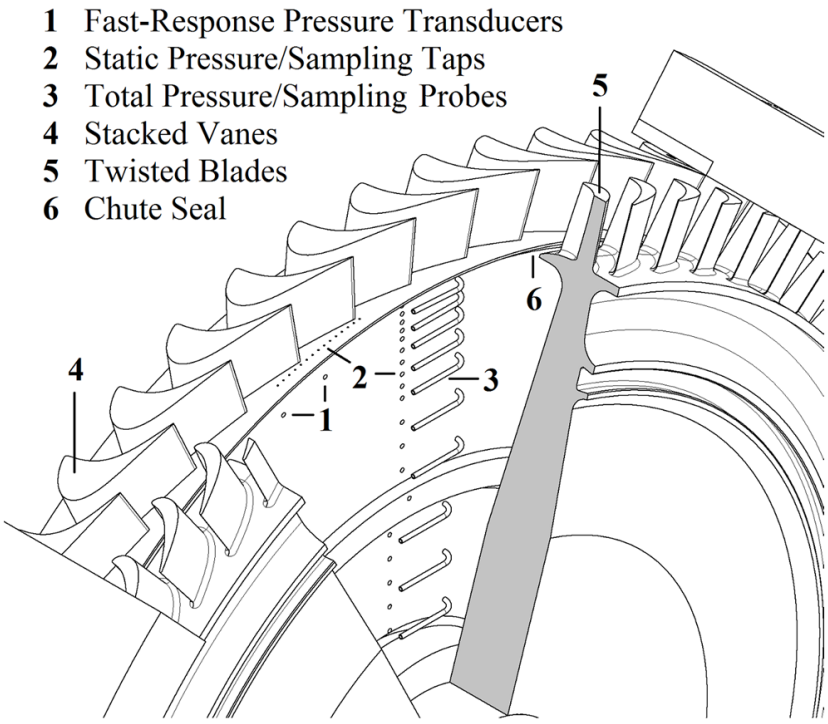

Figure 6-2: Experimental test section and instrumentation (Horwood *et al*, 2019)

6.2 Experimental Results

Presented here are experimental measurements and CFD computations, taken in the annulus and upstream wheel-space. It must be noted, the computations were made by Joshua Horwood, whose predicted results were required to validate against the experimental data. The results include distributions of steady and unsteady pressure, swirl and concentration effectiveness. Section 6.2.1 compares experiments with time-averaged computations which include pressure coefficient ($C_{p,a}$) in the annulus, pressure coefficient ($C_{p,s}$). Section 6.2.2 provides results for the variation of swirl ratio and sealing flow effectiveness in the wheel-space. The final Section 6.2.3 compares experiments and computations of unsteady pressure data acquired at a location near the rim seal clearance.

6.2.1 Distribution of Pressure in the Annulus and Wheel-Space

Measurements for the non-dimensional pressure coefficient ($C_{p,a}$), is plotted in Figure 6-3, across four vanes pitches. The static pressure was measured in the circumferential and radial locations, on the vane platform and wheel-space (Figure 6-2), respectively. The computational and experimental results clearly show the expected pressure asymmetry caused by the presence of the vanes. Both experiments and computations show good agreement for a non-dimensional sealing flow-rate of 0.075. The CFD was able to accurately capture the circumferential pressure distribution on the vane platform. Although not plotted on Figure 6-3, other sealing flow-rates were tested, and similar pressure distributions were captured, for both experiments and computations. Previous publications have shown that there is a second-order effect of Φ_0 on distribution of $C_{p,a}$ known as the *spoiling effect*, (Da Soghe *et al*. (2016) and Sangan *et al*. (2013).

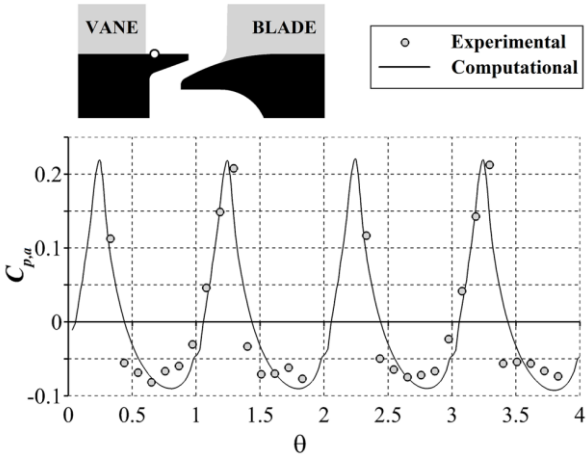

Figure 6-3: Circumferential distribution of pressure over four vane pitches (Φ_0=0.075). By Horwood *et al.* (2019)

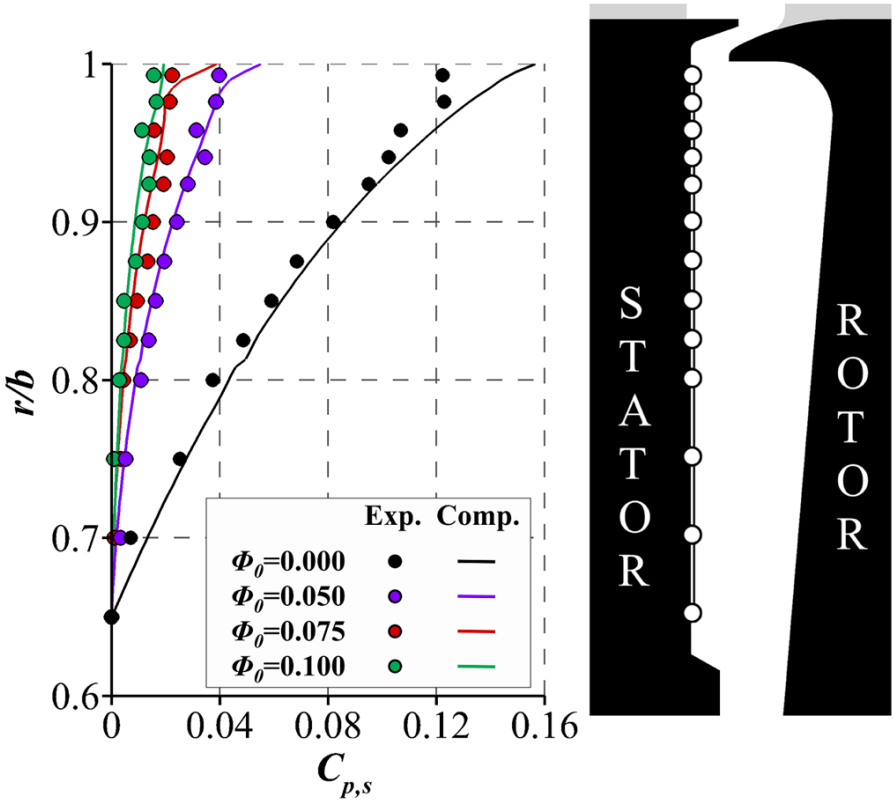

Figure 6-4: Radial distribution of pressure for four sealing flowrates. Horwood *et al.* (2019)

Figure 6-4 shows the radial distribution of pressure coefficient ($C_{p,a}$), along the stator wall in the wheel-space. The measurements were taken at four sealing flow rates, Φ_0=0,0.05,0.075 and 0.1. The sealing flow rate is controlled by an automated mass flow controller, and zero sealing flow rate is achieved when the valve is fully closed. The results demonstrate that, with no sealing flow applied to the wheel-space, the radial variation of pressure is large, however when sealing flow is introduced the variation of pressure decreases. The results also suggest that the tangential velocity throughout the wheel-space must be supressed with increasing sealing flow-rate, in order to decrease the radial pressure gradient. Section 6.2.2 discusses the radial distribution of swirl in the wheel-space.

6.2.2 Distribution of Swirl and Effectiveness in the Wheel-Space

To complement the results in Figure 6-4, experimental and computational measurements of radial distribution of swirl are presented in Figure 6-5. The data were taken in the wheel-space, for a range of turbulent flow (λ_T) parameter values, 0, 0.055, 0.083 and 0.111. The sealing flow rate is controlled by an automated mass flow controller, and zero sealing flow rate is achieved when the valve is fully closed. The turbulent flow parameter, λ_T, is a function of the sealing flow rate (Equation 2-3), therefore λ_T is zero when the valve is closed, and no sealing flow is allowed. Owen (1989) discusses the turbulent flow parameter and identify it as the driver for the boundary layers in rotor-stator systems. Once again, the CFD has accurately captured the fluid dynamics in the wheel-space and the swirl results show good agreement between experiment and computation. As expected, Figure 6-5 clearly shows the tangential velocity throughout the wheel-space becomes supressed with an increasing sealing flow rate, this is consistent with the swirl results by Horwood *et al.* (2018).

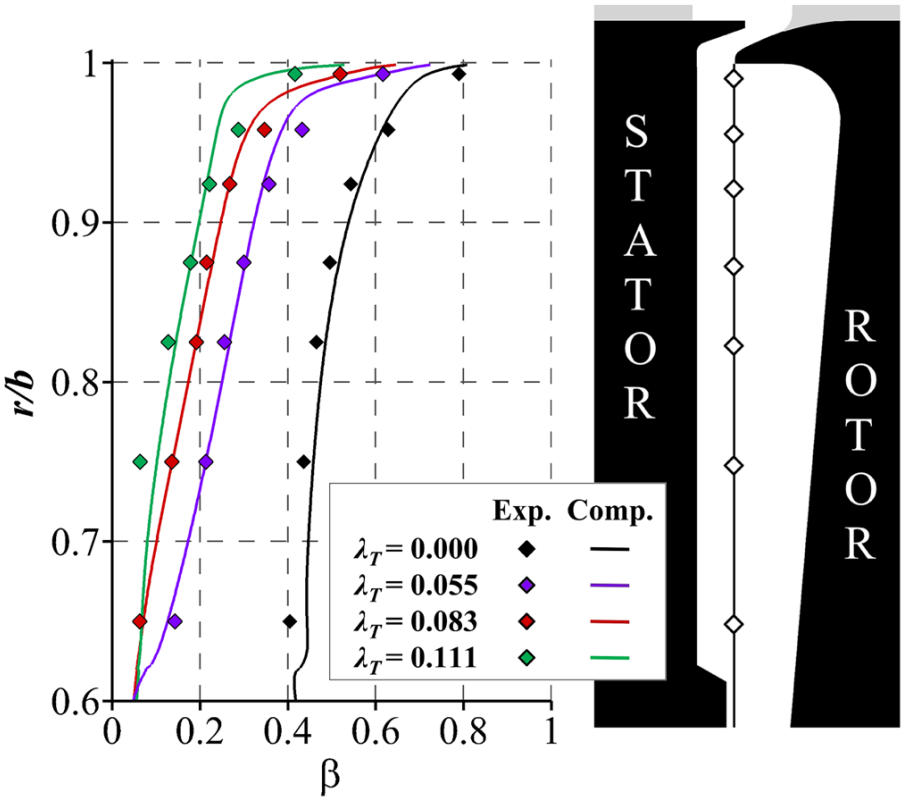

Figure 6-5: Distribution of swirl in the wheel-space at four sealing flowrates (Horwood *et al*, 2019)

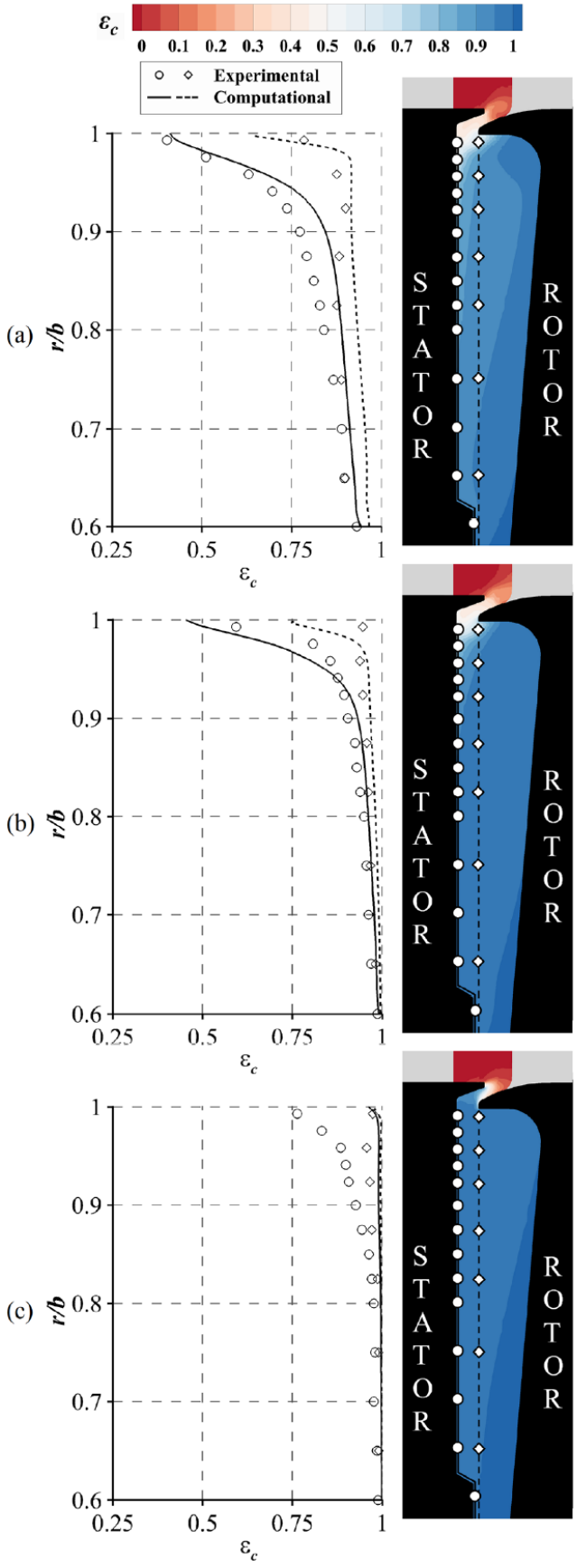

Figure 6-6: Radial distribution of effectiveness, for experiments and computations at sealing flowrates of Φ_0 = 0.050, 0.075 and 0.100 (Horwood *et al*, 2019)

Radial distributions of concentration (CO_2) effectiveness is presented in Figure 6-6 (a-c), on the stator wall (circles for experiments and solid lines for CFD) and rotating core (diamonds for experiments and dashed lines for CFD). The sealing flow rates tested were; Φ_0 = 0.050, 0.075 and 0.100. The experiments and computations were carried out at Re_Φ=1.3x10^6. The chute seal silhouettes (right hand of Figure 6-6) are geometrically aligned with the *r/b* axis (left hand side). The silhouettes also include superimposed contours of radial effectiveness (ε_c), computed in the wheel-space.

The results in Figure 6-6 (a-b) show that the lower sealing flow rates, Φ_0 = 0.050 and 0.075, exhibit good agreement, between the experiments and computations, both on the stator wall and in the core. The contours of effectiveness in the wheel-space demonstrate a sharp rise across the chute seal, near the free-stream where ε_c is virtually zero; at *r/b*=1 the effectiveness is ~0.35 but then sharply increases to ~0.85 at *r/b*=0.8. In contrast to the results on Chapter 4 (section 4.2.4), the sharp rise in effectiveness demonstrates unconventional behaviour in the wheel-space. Patinios *et al.* (2016) showed that the flow structure is less discontinuous, without steep gradients, but for a different seal configuration. This suggests the geometry of the chute seal has an impact on effectiveness. The Batchelor-type flow structure suggests that the stator boundary layer creates an invariant distribution of effectiveness along the stator wall, without sharp gradients. Therefore, the behaviour found in Figure 6-6 (a-b) departs from conventional Batchelor-type flow. The large mixing region in the wheel-space is caused by sealing flow being pumped up the rotor boundary layer, with higher concentration, resulting in differences between the core and the stator effectiveness. The contours suggest that the shape of the chute seal influences the rotor boundary layer to impose and impinge directly on the stator wall. The computed contours also suggest that deeper into the wheel-space at *r/b* < 0.8 the gradient in radial effectiveness is significantly suppressed, hence the stator wall and core has virtually the same levels of effectiveness.

The experimental data in Figure 6-6 (c) shows the same trend as Figure 6-6 (a-b), with a strong gradient in radial effectiveness seen near the chute seal. However, quantitatively the experiments and computations do not have a good agreement at the high sealing flow-rate, Φ_0 =0.100. The mismatch in effectiveness, between the experiments and computations, is discussed further in Figure 6-7.

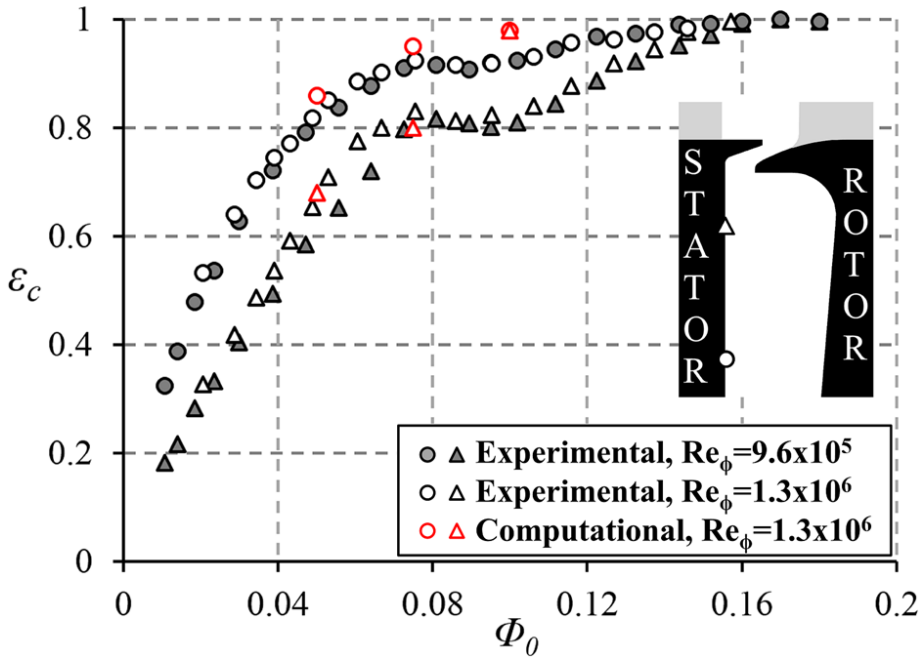

Figure 6-7: Distribution of effectiveness with non-dimenasional sealing parameter (Φ_0). By Horwood *et al.* (2019)

The distribution of sealing effectiveness with non-dimensional sealing flow parameter is shown in Figure 6-7; computations are labelled in open red symbols and included for comparison. The measurements were taken at *r/b* = 0.958 and 0.85, in the wheel-space. In general, sealing effectiveness curves typically exhibit an increasing effectiveness with sealing flow-rate, ultimately sealing the wheel-space and preventing ingestion. The experiments were conducted at two rotational speeds and were independent of Reynolds number, whilst the computations were conducted at only one rotational speed.

Experiments and computations agree well for values of Φ_0 below 0.08, however, an inflexion is seen in the experimental measurements between Φ_0 =0.06 and 0.12. This discrepancy is also shown in Chapter 5, and reported by Hualca *et al.* (2019), Horwood *et al.* (2018), Clark *et al.* (2017), Boudet *et al.* (2015) and Gentilhomme *et al.* (2003). The experimental data also shows that the degree of inflexion measured at *r/b* = 0.958 is affected by the Reynolds number, producing a larger inflexion at Re_Φ=1.3x10^6. This is not captured by the computations, however, which explains the mismatch in radial effectiveness seen in Figure 6-6 (c). Hualca *et al.* (2019) and Horwood *et al.* (2018) connected the inflexions in the sealing effectiveness curves to the strong unsteady pressure structures (large-scale structures) near to the rim seal. In Chapter 5 (section 5.2.3) it was shown that the unsteadiness and inflexion vanish when the blades are removed and therefore it is speculated that the blades are causing this phenomenon.

6.2.3 Unsteady Pressure in the Wheel-Space

This section presents measurements of unsteady pressure over a range of sealing flow-rates. The effect of sealing flow rate on unsteady pressure was investigated. In Chapter 5, unsteady pressure results were presented but for a generic stage (seal, vanes and blades). The FFTs in chapter 5 showed that the number of flow structures varied between $22 < N < 28$ with a bladed rotor configuration but increased to $34 < N < 40$ for a bladeless rotor. The results presented here are for an engine realistic stage and at higher operating flow conditions (Table 3-3). Experiments were conducted and CFD was computed at identical flow conditions which simulated the experimental 1.5-stage turbine test rig. The CFD was computed with a sector model of 30° (Horwood *et al.* 2019). Figure 6-8 compares CFD (left column) and experiments (right column) for unsteady pressure data, at four sealing flow-rates; $\Phi_0 = 0$, 0.05, 0.075 and 0.1.

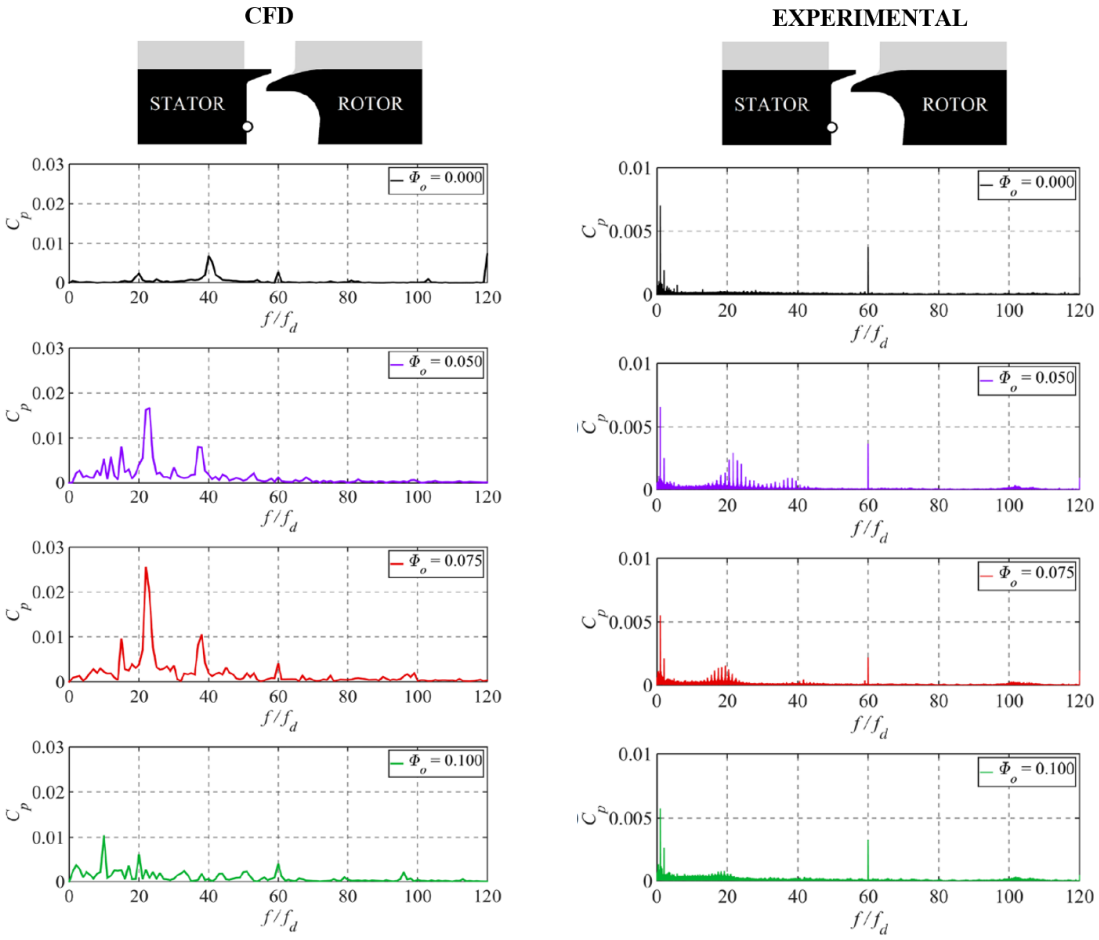

Figure 6-8: Fast Fourier Transforms of computational (left hand side) and experimental (right hand side) data at Re_Φ=1.3x10^6. By Horwood *et al.* (2019)

A phase analysis was performed, as introduced in Chapter 5 (Section 5.2.4). Two pressure transducers were placed 11.25° apart (α) in the azimuthal direction. The computations were sampled over one disc revolution; the experiments were sampled over ~860 revolutions, offering higher resolution for the experiments FFTs.

Comparing results in Figure 6-8, demonstrates that at f/f_d = 60 there is a clear spike of unsteady activity which corresponds to the blade passing frequency, for both, experiments and computations. Furthermore, the results also show that other distinct frequencies below the blade passing frequency exist, and that the amplitude of these frequencies are dependent on sealing flow-rate. The frequencies of the experiments and computations match but the amplitudes (C_p) do not. The difference in amplitudes between the experiments and computations is linked to the RANS turbulence modelling. Greater viscosity in the turbulence model can produce more steady flow structures and therefore produce clearer and higher amplitudes.

Consider first the sealing flow-rate Φ_0 = 0. The experiments show an almost unnoticeable peak at f/f_d = 40, but the computations show a more pronounced peak for the same frequency, which corresponds to N = 36 structures. These structures rotate at ω/Ω ~ 1.11 (Table 6-1). Now consider the higher sealing flow-rates Φ_0 = 0.05 and 0.075, the frequency f/f_d = 40 has decreased to 23 which gives N = 24 structures, rotating at ω/Ω ~ 0.96. However, at the maximum sealing flow-rate (Φ_0 = 0.100) the pressure signals decrease in amplitude and the frequency reduces to f/f_d = 10 for CFD and 19 for the experiments. Table 6-1 summarises all the values for N and ω/Ω, for a range of sealing flow rates.

Table 6-1: Number (N) and rotational speed of large-scale flow structures

Case	Non-dimensional Sealing Parameter (Φ_0)	Approximate number of structures (N)	Rotational speed of structures (ω/Ω)
Comp. (30°)	0.000	36	1.11
Comp. (30°)	0.050	24	0.96
Comp. (30°)	0.075	24	0.92
Comp. (30°)	0.100	12	0.83
Comp. (60°)	0.050	30	1
Comp. (90°)	0.050	28	0.98
Comp. (360°)	0.050	29	0.95
Exp.	0.000	N.A	N.A.
Exp.	0.050	21	1.03
Exp.	0.075	21	0.92
Exp.	0.100	N.A	N.A.

The experiments and computations consistently capture unsteady activity at the blade passing frequency. The weak unsteady activity in the experiments for $\Phi_0 = 0$ is speculated to be a consequence of the low sealing flow rate not producing a strong enough shear gradient between annulus and wheel-space. Horwood *et al.* (2019) showed computationally that a strong shear gradient in swirl exists across the seal, for the highest sealing flow rate ($\Phi_0 = 0.1$), Figure 6-9. On the other hand, at the maximum sealing flow-rate, $\Phi_0 = 0.1$, the weak unsteady activity observed in the experiments could be a result of the egress dominating the fluid dynamics and therefore expelling the largescale flow structures.

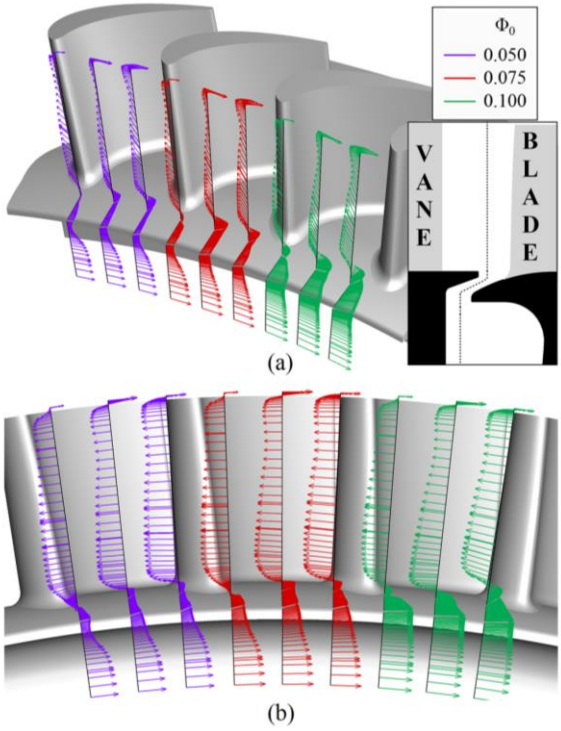

Figure 6-9: Velocity vectors through the seal (rotational frame of reference) at three levels of sealing flow (Horwood *et al,* 2019)

Quantitatively and qualitatively, the computations and experiments compare well. Furthermore, both experiments and computations capture the blade passing frequency and show the dominant peaks occurring at almost the same frequencies, for all sealing flow-rates. Interestingly the absolute amplitudes of the experiments are significantly lower than those computed. The discrepancy in absolute amplitudes between the experiments and computations is believed to be a result of RANS turbulence modelling. Horwood *et al.* (2019) stated that, greater viscosity or the treatment of turbulence in the RANS turbulent model, could influence the structures to become more stable, and hence produce clearer and higher amplitudes.

Despite this, the overall behaviour of the CFD is encouraging and provides clear insight into the unsteady fluid dynamics.

6.3 Summary

An engine realistic stage was studied, to investigate the fluid dynamics of ingress. Time accurate computations, and time-averaged experiments were measured, as well as unsteady RANS computations. Both, the experiments and computations demonstrated good qualitative and quantitative agreement, for steady and unsteady pressure measurements, as well as swirl and sealing effectiveness. The results suggest that flow through the rim-seal is subjected to high shear, this behaviour is related to the two most common hypotheses for the formation of large-scale structures, Taylor-Couette or Kelvin-Helmholtz instabilities.

Unsteady pressure measurements and computations were conducted, for an engine representative chute seal. Unsteady pressure results in Chapter 5 showed that the number of flow structures varied between $22 < N < 28$, for a bladed rotor, but increased to $34 < N < 40$ for a bladeless rotor. However, unsteady pressure results for the engine-realistic chute seal, revealed flow structures that ranged from $12 < N < 36$, for both, experiments and computations. The structures rotated at just below the disc speed and their strength reduced with increasing sealing flow rate.

The results support the hypothesis of flow instabilities being driven by shear gradients near the seal clearance region. The evidence suggests that these structures influence ingress. The CFD results (Figure 6-9) show that the introduction of sealing flow increases the strength of shear gradients and encourage the flow structures to move radially outward. Above a critical sealing flow rate egress dominates and the flow structures are blown out from the seal clearance.

In contrast to the sealing effectiveness results in Chapter 4 and 5, where a generic stage was tested, the wheel-space flow structure (Figure 6-6) showed unconventional behaviour. This demonstrates that flow behaviour in the wheel-space is dependent on wheel-space and seal geometry.

Chapter 7: Re-Ingestion into the Downstream Wheel-space

This chapter investigates re-ingestion of upstream egress. Hot combustion gases leave the combustion chamber, and a portion gets ingested into the wheel-space of first stage. Therefore it is critical to cool down the first stage. However other stages also need to be cooled down, and recent computational studies suggest that re-ingestion could enhance cooling. This study aims to experimentally demonstrate that re-ingestion of upstream egress has the potential to strongly reduce the effect of ingress in the downstream wheel-space since the upstream egress is significantly cooler than the mainstream flow.

Re-ingestion was measured, and a theoretical mixing model was developed by Prof. Owen, which was validated by the experimental measurements. This is the first time an experimental procedure and theoretical model has been developed to quantify re-ingestion into downstream wheel-space. Seeding was injected into the upstream and downstream wheel-spaces and measurements of CO_2 concentration were made. The experiments were conducted using radial-clearance rim seals at incompressible flow conditions.

7.1 Experimental Set-up

Experiments were conducted at two operating points under sub-sonic flow conditions, presented in Table 3-4. The speed of sound, density and air viscosity were calculated using the static temperature and pressure measured on the stator wall inside the upstream and downstream wheel-spaces at r/b = 0.958. A radial-clearance rim seal was installed in the upstream and downstream wheel-space, with dimensions given in Table 3-6. The test section was instrumented with static and total pressure probes as well as fast-response pressure transducers. The stationary disc included 32 stacked vanes and the rotor disc comprised of 48 turned blades (Figure 7-1). Siemens provided the blade and vane geometry; they were designed especially for one of their experimental engines.

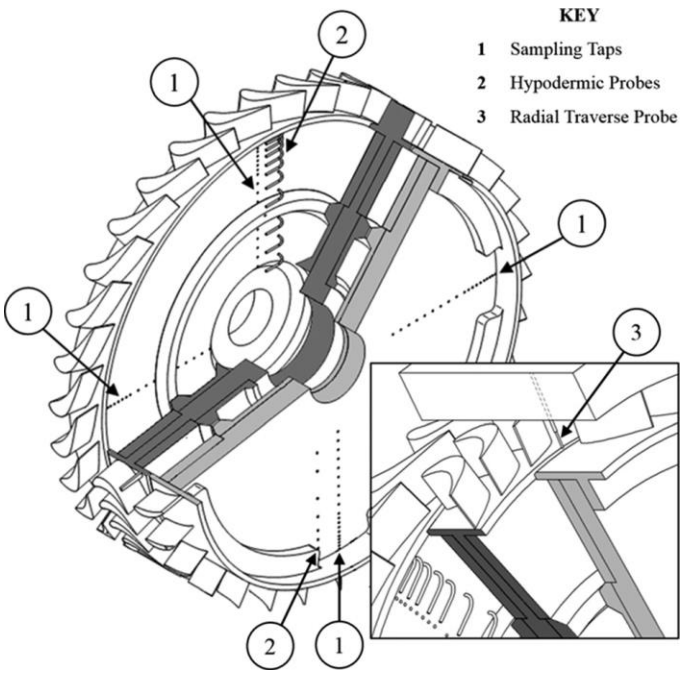

Figure 7-1: Experimental test section and instrumentation (Scobie *et al,* 2018)

7.2 Interpretation of Re-Ingestion

Consider a disturbance effect on the flow field downstream of the blades, near the rim seal mixing plane, caused by an unseeded egress flow. Unseeded means that, the upstream sealing flow has no seed (CO_2), therefore the CO_2 concentration of the annulus and egress flow are identical. If the downstream sealing flow is seeded, this scenario can be considered a purely fluid-dynamic effect since only the egress flowrate flow would affect the downstream flow field and not concentration (CO_2). This disturbance effect has the potential to affect ε_d and $c_{a,d}$ as unseeded flow would dilute the downstream CO_2 concentration, but if the upstream flow is seeded it should only affect $c_{a,d}$ and not ε_d. Once the flow crosses the downstream mixing plane, it is expected to be fully mixed, therefore no variance in ε_d . Symbols ε_d and thus $c_{a,d}$ can be found in the nomenclature. The subscripts a, *u* and *d* represent, annulus, upstream and downstream wheel-spaces.

Now consider a carry-over effect. This occurs when the upstream egress has not completely mixed with the annulus flow, resulting in $c_{a,d} > c^*_{a,d}$; parameters denoted with the superscript '*' correspond to cases where the upstream sealing flow was not seeded. A scenario where the flow is not fully mixed implies that the carry-over of upstream egress increases the concentration of the ingested fluid in the downstream wheel-space. A carry-over of upstream egress could be considered beneficial as it implies that the downstream wheel-space would benefit from re-ingestion, as it would get extra cooling. However, if there is complete mixing

between the upstream egress and the annulus flow then $c_{a,d} = c^*_{a,d}$; this implies that there is not carry-over of upstream egress, therefore the downstream wheel-space does not benefit from re-ingestion. In order to distinguish the carry-over and disturbance effects, two sets of experiments were conducted for a range of upstream and downstream sealing flow rates. The first set of experiments consisted of seeded sealing flow and the second set of experiments consisted of unseeded sealing flow to the upstream wheel-space. In this chapter these experiments are referred to as the upstream-unseeded and upstream-seeded tests.

Section 7.4 presents results for the mass fraction (χ) of re-ingested upstream egress, measured as a function of the downstream sealing flow rate. The analogy used for the balance between the fluid carried over and the ingress into the downstream wheel-space is, the analogy between heat and mass transfer. The analogy assumes turbulent flow in the boundary layers and similar molecular weight between the mainstream and seed (CO_2). Under these conditions the analogy states that the turbulent Prandtl number (governs heat transfer) and the turbulent Schmidt number (governs mass transfer) are virtually identical at all locations in the flow. At sea level conditions, the Prandtl and Schmidt number, for air and CO_2, is approximately 0.75 and 0.79, respectively. Here the mass-concentration flux, $\dot{m}' c_{e,u}$, is assumed to be analogous to the enthalpy flux, $\dot{m}' h_{e,u}$. In a real gas turbine, it is expected that the heat transfer to the carry-over fluid, in the blade passage, will reduce the benefit of any re-ingestion.

7.3 Results

Results are presented here for the re-ingestion of upstream egress. Concentration measurements were taken in the upstream and downstream wheel-spaces. For the seeded tests the upstream sealing flow was seeded with 3% CO_2 ($c_{0,u}$ = 0.03) and the upstream annulus flow ($\dot{m}_a$) was unseeded. In this study all experiments were conducted with the radial-clearance seal shown in Figure 3-6.

- Section (7.4.1) sets the scene for re-ingestion, it includes results for the variation of concentration effectiveness, $\varepsilon_{c,u}$, with seeded upstream sealing flow $\Phi_{0,u}$. Furthermore, the variation of non-dimensional ingress and egress flow-rate is compared to the $\varepsilon_{c,u}$ curve.
- Section (7.4.2) presents results for the variation of effectiveness across the annulus height and demonstrates how the seeded upstream egress migrates radially, downstream of the blade passage.
- Section (7.4.3) introduces the first set of re-ingestion measurements regarding the disturbance effect. The results in this section involve upstream-unseeded tests but with the downstream sealing flow seeded with a tracer gas.
- The final Section (7.4.4) presents measurements of re-ingestion that involve a carry-over effect. The results in this section are for upstream-seeded and downstream-seeded sealing flows. The tracer gas used for these experiments was the same as the one used for the disturbance effect tests.

7.3.1 Variation of Concentration in the Upstream Wheel-Space

The baseline results for the re-ingestion experiments are shown in Figure 7-2. The results show the variation of concentration effectiveness ($\varepsilon_{c,u}$), the ratio of ingress flowrate to minimum sealing flowrate ($\Phi_{min,u}$), and the ratio of egress flowrate to minimum sealing flowrate. The concentration measurements were taken in the upstream wheel-space, on the stator wall at r/b = 0.958, as shown on the silhouette. The tests were conducted at three sealing flow-rate conditions; these conditions were also matched in the re-ingestion experiments, which correspond to, $\Theta_{0,u} = \Phi_{0,u}/\Phi_{min,u}$ = ½, 1 and 2. Evidently $\varepsilon_{c,u}$ increases with increasing $\Phi_{0,u}$, as expected. The wheel-space becomes fully sealed and reduces ingress across the seal clearance. The experimental data are complimented by a theoretical effectiveness curve fit (Equation 2-9). Both the experiments and the theoretical curve show good agreement. The ratio $\Phi_{0,u}/\Phi_{min,u}$ is based on the theoretical fit and is plotted on the secondary x-axis.

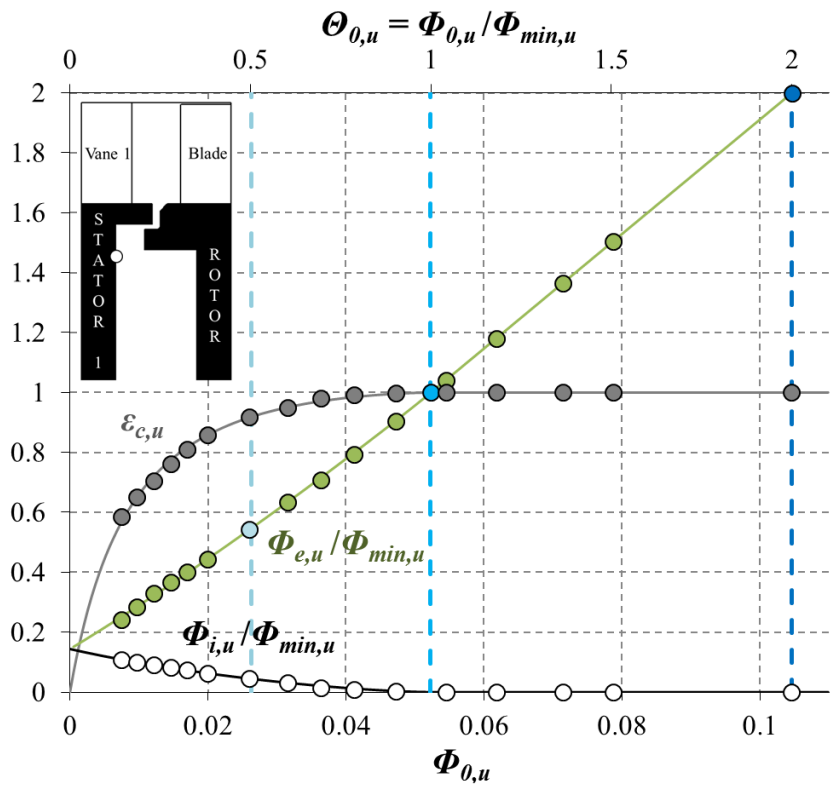

Figure 7-2: Distributions of concentration effectiveness, ingress and egress flow ratios with non-dimensional sealing flow rate in the upstream wheel-space (Symbols denote data; lines are theoretical orifice-model fits). By Scobie *et al.* (2018)

Three vertical, blue dashed lines, can be seen on the secondary x-axis in Figure 7-2, intersecting with the sealing effectiveness, ingress and egress curves. At the intersection, when $\Phi_{0,u}/\Phi_{min,u} =$ ½, ingress occurs and $\varepsilon_{c,u} \approx 0.95$, the ratio of egress is approximately 0.55 and the ratio of ingress is around 0.05. At $\Phi_{0,u} = \Phi_{min,u} = 1$ the wheel-space is fully sealed; hence the ratio of ingress becomes zero and all the sealing flow exits the wheel-space as egress. At $\Phi_{0,u}/\Phi_{min,u} =$ 2 the egress leaves with twice the flow-rate of the fully sealed case and with the same concentration. By definition (Equation 4-1) $\varepsilon_{c,u}$ cannot reach a value greater than 1.

7.3.2 Effect of Upstream Sealing Flow in the Downstream Wheel-Space

The concentration profiles shown in Figure 7-3 represent the radial migration of upstream egress in the downstream annulus, for three sealing flow ratios, $\Phi_{0,u}/\Phi_{min,u} =$ ½, 1 and 2. The results demonstrate a radial migration of upstream egress that increases with sealing flow momentum. As expected, the concentration for the sealing flow ratio $\Phi_{0,u}/\Phi_{min,u} =$ ½ is lower than the higher sealing flow ratios, since egress concentration ($c_{e,u}$) decreases with decreasing $\Phi_{0,u}$. For the high sealing flow ratios, $\Phi_{0,u}/\Phi_{min,u} \geq 1$, the egress concentration increases only across the blade passage but will be unchanged at the boundary layer on the platform, so that

$c_{e,u} = c_{0,u}$ for any fluid entrained into the downstream ingress, across the downstream seal clearance. This is shown by the two blue curves for $0.995 < r/b < 1.055$.

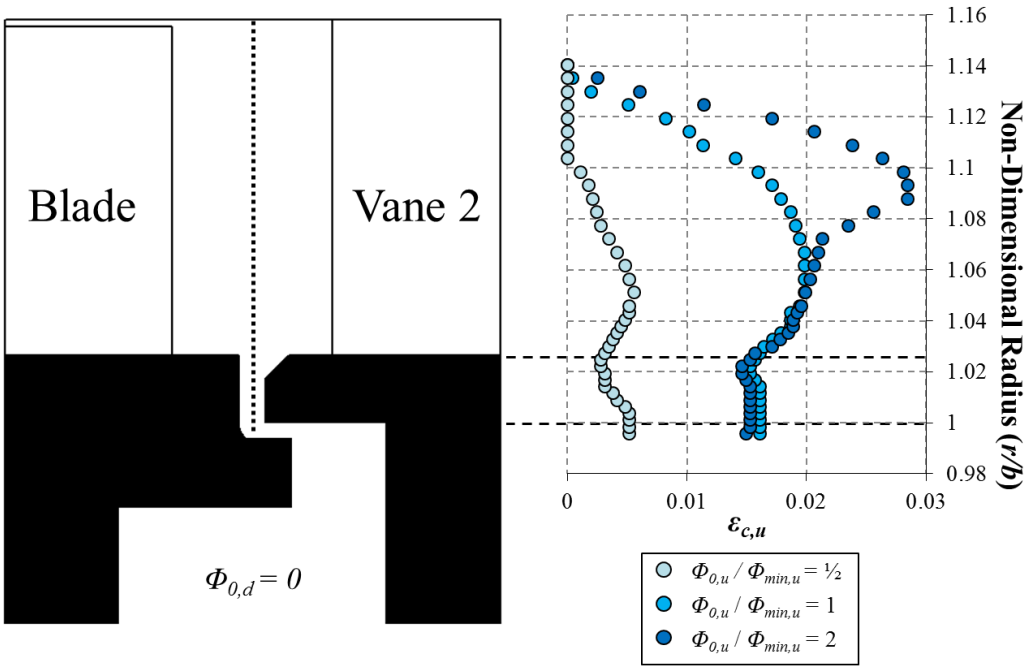

Figure 7-3: Influence of upstream egress rate on radial distribution of re-ingestion in the downstream annulus and rim seal region for $\Phi_{0,d} = 0$. By Scobie *et al.* (2018)

7.3.3 Disturbance Effect of Re-Ingestion

The results presented in this section are for upstream-unseeded tests. The sealing flow in the downstream wheel-space was seeded with a tracer gas and the measurements were taken in the downstream wheel-space on the stator wall at r/b = 0.958, as shown on the silhouette (Figure 7-4). The derivations for $\varepsilon^*_{c,d}$ and $\varepsilon_{c,d}$ can be found in Section 2.4. Figure 7-4 shows the variation of effectiveness with downstream sealing flow, for the baseline case, that is without upstream sealing flow ($\Phi_{0,u}$= 0). Furthermore, the ratio of ingress to $\Phi_{min,d}$ and the ratio of egress to $\Phi_{min,d}$ is shown on the same figure. Similarly to Figure 7-2, the wheel-space becomes pressurised with increasing sealing flow and $\varepsilon_{c,d}$ increases with $\Phi_{0,d}$; a theoretical effectiveness curve was fitted to the experimental data. The results are consistent with Figure 7-2 and there is good agreement with the experiments. When $\Phi_{0,d}$ = 0 there is no sealing flow present in the wheel-space and the ingress that enters the wheel-space leaves as egress, $\Phi_{i,d}$ = $\Phi_{e,d}$. However, when the wheel-space is fully sealed, $\Phi_{0,d}$ = $\Phi_{min,d}$, and ingress no longer penetrates through the rim seal; all sealing flow leaves the wheel-space as egress.

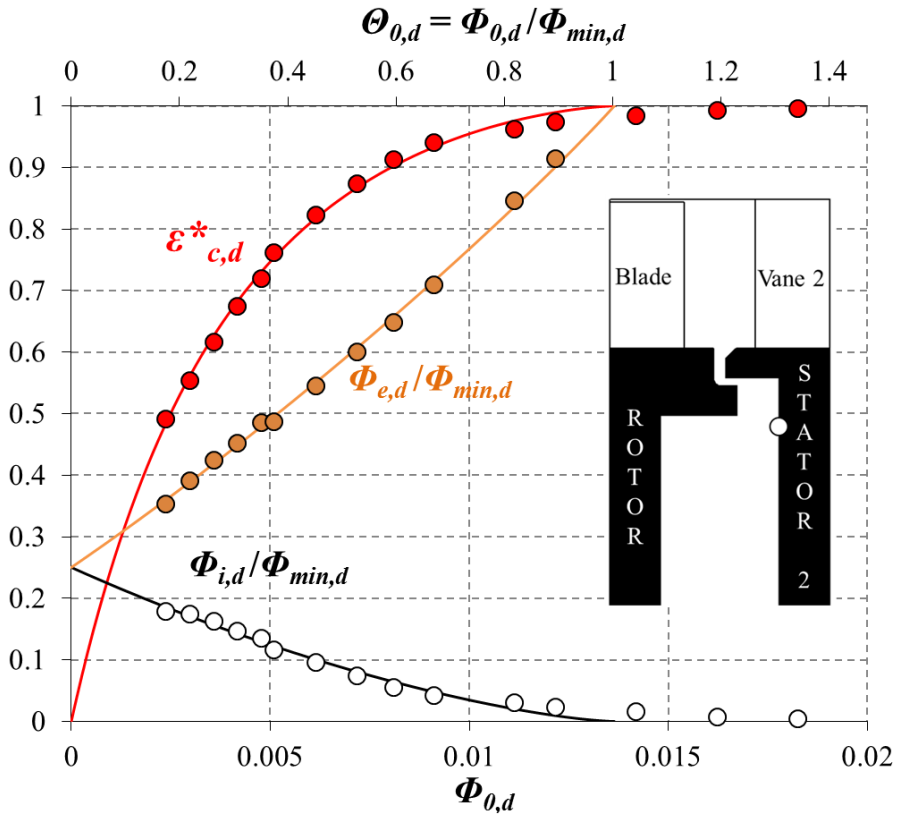

Figure 7-4: Distributions of downstream concentration effectiveness, ingress and egress flow ratios for the datum case without upstream sealing flow (Symbols denote data; lines are theoretical orifice-model fits). By Scobie *et al.* (2018)

The sealing effectiveness curve in Figure 7-4 has been reproduced in Figure 7-5, to compare the disturbance effect. The results demonstrate that the variation of effectiveness for three upstream-unseeded flow conditions: $\Phi_{0,u}/\Phi_{min,u}$ = ½, 1 and 2 does not differ from the reproduced curve at $\Phi_{0,u}/\Phi_{min,u}$ =0 . Clearly the increase of unseeded upstream sealing flow rate does not create a disturbance effect, therefore the results fall onto a single curve.

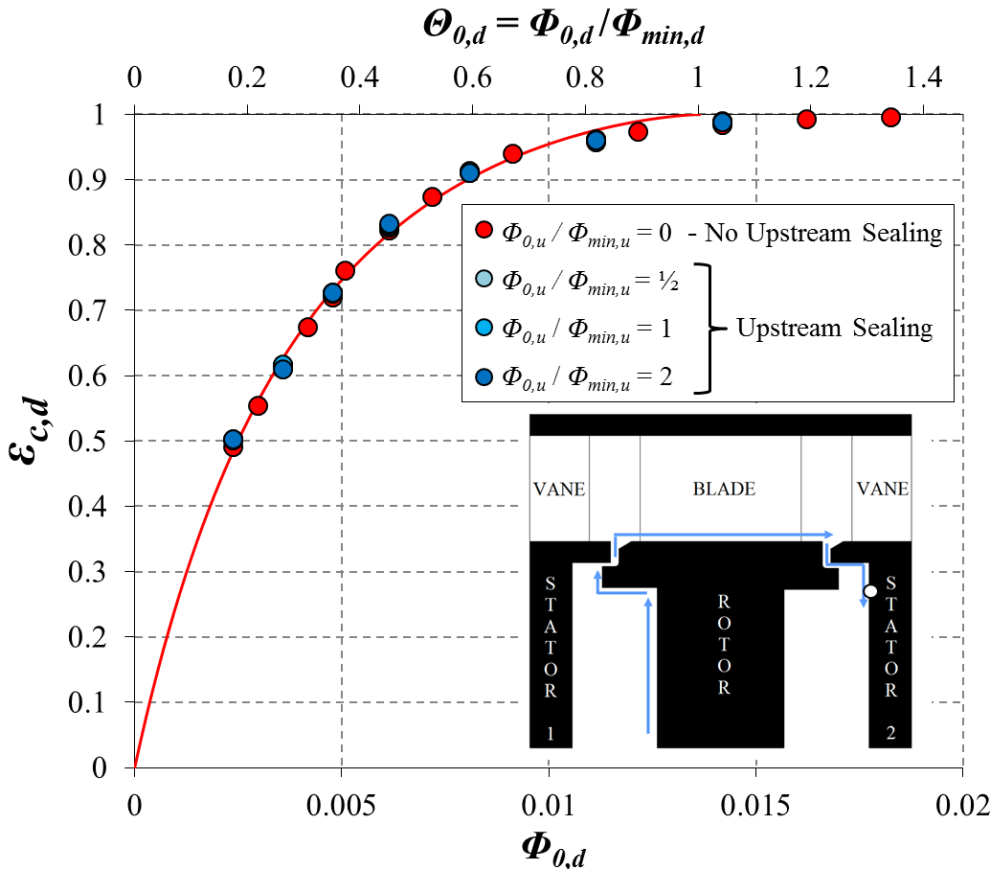

Figure 7-5: Downstream measurements of concentration effectiveness with sealing flow rate for four values of *unseeded* upstream sealing flow (Symbols denote data; line is theoretical orifice-model fit). By Scobie *et al.* (2018)

7.3.4 Carry-Over Effect of Re-Ingestion

The results presented in this section are for the upstream-seeded tests. The downstream sealing flow was also seeded. The data in Figure 7-6 compares the effectiveness distribution for the baseline case, that is without upstream sealing flow ($\Phi_{0,u}$= 0) as described in section 7.4.3, with cases where egress is re-ingested into the downstream wheel-space, $\Phi_{0,u}/\Phi_{min,u}$ = ½, 1 and 2. The results demonstrate an increase in effectiveness relative to the baseline case.

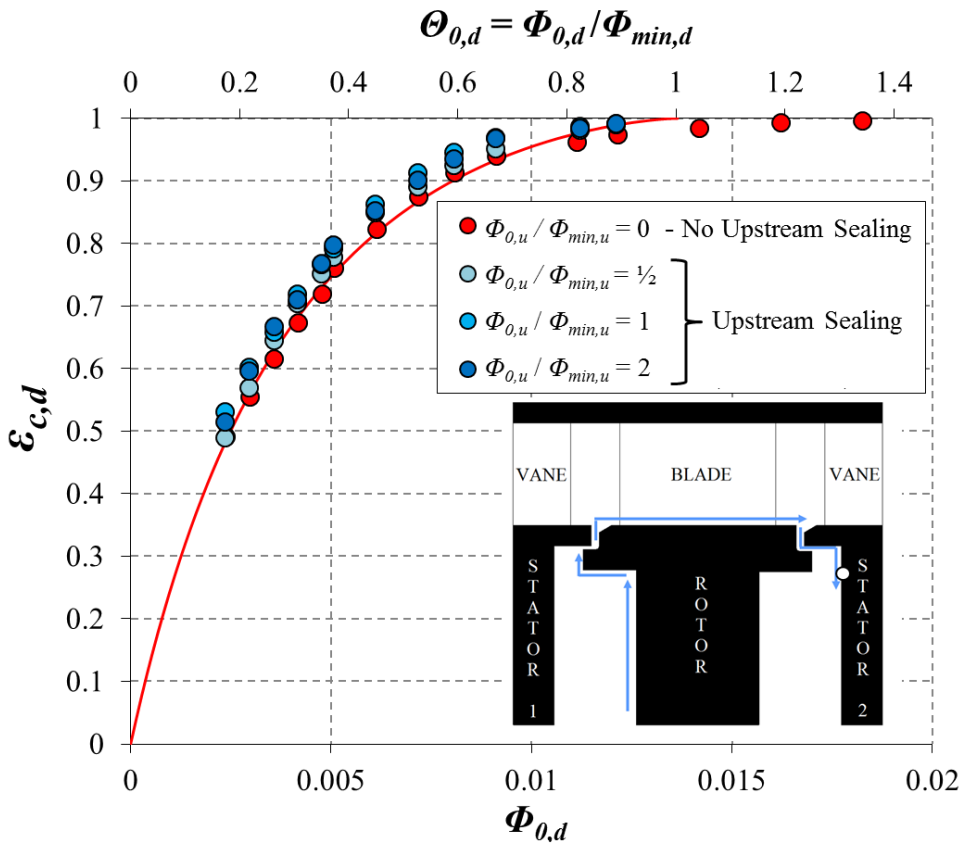

Figure 7-6: Downstream measurements of concentration effectiveness with sealing flow rate for four values of *seeded* upstream sealing flow (Symbols denote data; line is theoretical orifice model fit). By Scobie *et al.* (2018)

The mass fraction (χ) of re-ingested upstream egress was evaluated and plotted against $\varepsilon_{c,d}$, as shown in Figure 7-7. It is important to first explain the physical meaning of χ, the carry-over fraction. When $\Phi_{0,d}$ = 0 (and $\varepsilon_{c,d} \rightarrow 0$), ingress and χ reach a maximum and minimum point, respectively. As $\Phi_{0,d} \rightarrow \Phi_{min,d}$ (and $\varepsilon_{c,d} \rightarrow 1$) the flow ingested into the downstream wheel-space experiences an increased fraction of upstream egress , making $\chi \rightarrow 1$.

Consider the case when $\Phi_{0,u}/\Phi_{min,u}$ = 1 and $\Phi_{0,u}/\Phi_{min,u}$ = ½. χ produces lower values when $\Phi_{0,u}/\Phi_{min,u}$ = ½. The concentration $c_{e,u}$ decreases as ingestion takes place in the upstream wheel-space, this is consistent with Figure 7-2. When $\Phi_{0,u}$ reaches or exceeds $\Phi_{min,u}$, the egress

concentration cannot exceed the sealing flow concentration, i.e., $c_{e,u} = c_{0,u,}$. Surprisingly when the sealing flow is twice $\Phi_{min,u}$ ($2x\Phi_{min,u}$), there is no significant change on χ, this contradicts the original hypothesis that stated that the mass flow of egress entrained into the downstream ingress would increase as $\Phi_{e,u}$ increases. Considering Figure 7-3, near the blade platform the effectiveness concentration does not increase further once $\Phi_{e,u} > \Phi_{min,u}$, therefore it is possible that the carry-over fluid emerges from the boundary layer on the blade platform where the concentration does not change.

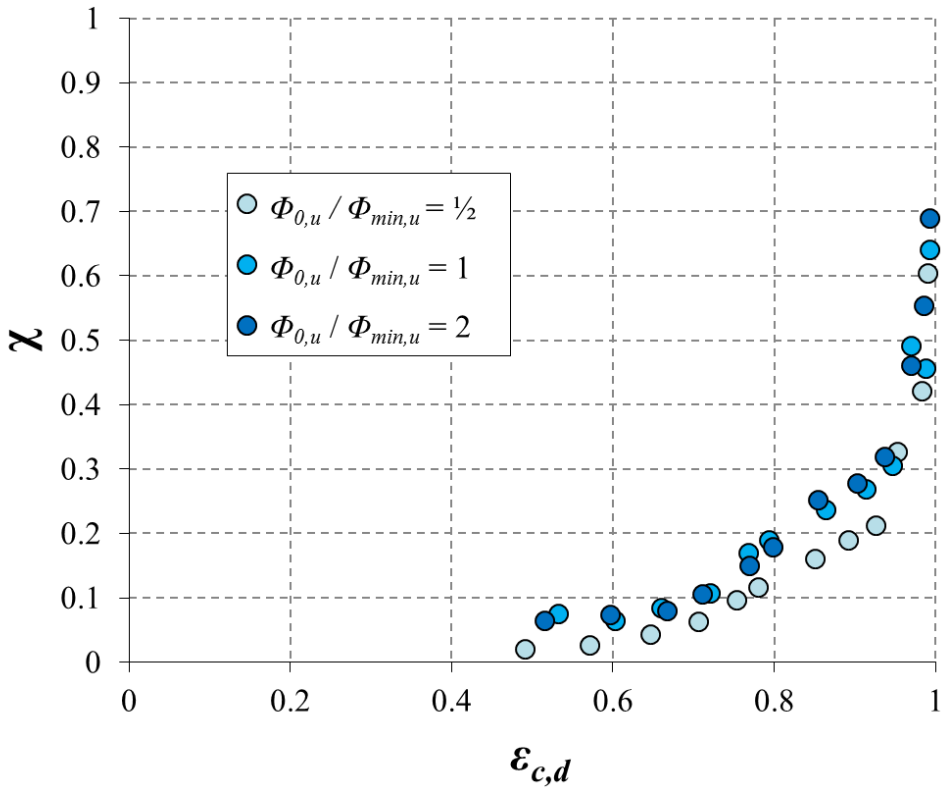

Figure 7-7: Measured variation of χ with non-dimensional downstream concentration effectiveness for three values of upstream sealing flowrate (Scobie *et al*, 2018)

In general, real engines operate at sealing flowrate conditions that produce approximately 95% sealing efficiency. Considering Figure 7-7, when the effectiveness is 0.95 (95%), χ is approximately 0.33 or 1/3. Equation 2-15 can be expressed as;

$$\frac{\dot{m}'}{\dot{m}_{i,d}} = \frac{1}{3} \qquad \textbf{Equation 7-1}$$

therefore,

$$\dot{m}' = \frac{\dot{m}_{i,d}}{3} \qquad \textbf{Equation 7-2}$$

The equation above (Equation 7-2) suggests that one-third of the mass flow ($\dot{m}_{i,d}$) that gets ingested into the downstream wheel-space, is carry-over fluid of the upstream egress. According to the mass-transfer analogy, the enthalpy balance from the entrained upstream egress of cooler temperature suggests that the downstream wheel-space would significantly benefit from re-ingestion.

7.4 Summary

Re-ingestion was thoroughly studied in a 1.5-stage gas turbine rig. Gas concentration measurements were made, with and without seeded sealing flow, in the upstream and downstream wheel-spaces. A concentration probe was traversed across the annulus and through the seal clearance, to study the annulus flow field and the interaction between the egress and annulus flow. A model was developed by Prof. Mike Owen, to evaluate the re-ingested fraction of carry-over fluid, from the upstream egress.

The results showed that the upstream egress does not influence the fluid dynamics in the downstream region, but partially mixes with the mainstream at a region near the seal mixing plane. The evidence suggests that upstream egress gets re-ingested with the emerging flow from the boundary layer on the rotor platform. Re-ingestion was evaluated for a range of sealing flow-rates. It was shown that χ increases with increasing downstream sealing flow rate, and approximately 33% could represent a typical re-ingestion of carry-over, in a real engine. The intense mixing between the upstream egress and mainstream, suggests a film-cooling benefit on the rotor platform, but with potential aerodynamic losses near the blade leading edge.

Chapter 8: Conclusions

A comprehensive study on ingestion was carried out in a 1.5-stage turbine rig. Various turbine stage geometries and engine conditions were tested. A novel experimental technique was developed in order to study the interaction between egress and mainstream flow. Furthermore, this unique methodology enabled traverse concentration measurements, the first of their kind, to map out the flow structure in the annulus and wheel-spaces.

Upstream of the blades, a strong circumferential variation of pressure produced different levels of ingestion. This encouraged asymmetry on concentration effectiveness, and the effect penetrated down across the seal clearance, for the two seal geometries. Furthermore, a region of intense mixing exists across the seal clearance, which varies circumferentially. Downstream of the blades, the asymmetry is less pronounced as the circumferential variation of pressure is weaker. The concentration and pressure measurements were not affected by different rotational Reynolds number.

Measurements of steady pressure, over a vane pitch, were precisely captured by CFD. The non-dimensional pressure change ($\Delta C_{p,a}$) decays axially from the trailing edge of the vane. Both, experiments and computations, showed that the rotor blades do not have a significant impact on $\Delta C_{p,a}$. The axial decay in $\Delta C_{p,a}$, measured on the upstream stator vane platform, is dependent on vane position but not on the presence of rotor blades.

Measurements of swirl on the inner wheel-space were not affected by vane position or presence of blades. However, in the outer wheel-space a pronounced inflexion appeared, over the critical sealing flow-rate range, $0.03 < \Phi_0 < 0.08$. The magnitude of inflexion changed with vane position but not rotational Reynolds number, furthermore, it disappeared in the absence of rotor blades.

Analysis of unsteady pressure revealed the existence of large-scale flow structures, for a generic and an engine-realistic stage. For the generic stage, the number of structures ranged from $22 < N < 28$ and slightly depended on vane position and sealing flow rate. A pronounced magnification of spectral activity occurred at precisely half the number of blades, for a purge rate of $\Phi_0 = 0.05$. In the absence of blades the pressure structures still existed, however, the structures rotated slower and occurred in greater number. For the engine-realistic stage, both, experiments and computations of steady and unsteady pressure, showed good agreement, as well as with swirl and sealing effectiveness. Large-scale flow structures were identified and ranged from $12 < N < 36$, they rotated close to the disc speed and were strongly affected by sealing flow rate. Both experiments and computations captured this effect. Regardless of the

stage geometry, the results suggest that these flow structures are initiated by shear gradients near the seal clearance, resulting in a direct influence on ingress. High sealing flow rates strengthens these shear gradients, however, above a certain threshold, the structures get expelled into the annulus and vanish. There is enough evidence to suggest that the amount and strength of these large-scale flow structures, is linked to the presence of blades, specifically at the inflexion region.

Flow structures were studied with a bladed, bladeless disc and different seal geometries. The results show that these structures exist regardless of stage geometric features. However, the number and speed of the structures are influenced by the stage geometric features and sealing flow rate.

Re-ingestion of egress was experimentally studied for the first time and validated with a theoretical model. The Upstream egress does not negatively influence the fluid dynamics downstream of the blades but does provide cooling benefits to the downstream wheel-space. The evidence suggests a potential cooling benefit but with added aerodynamic losses.

The mass fraction of re-ingested carry-over fluid, χ, increases with increasing downstream sealing flow rate. A typical gas turbine provides a sealing flow effectiveness of 95%, which corresponds to a χ value of approximately 0.33 (33%). Therefore it is expected that the second stage (downstream wheel-space) of a typical engine would benefit from 33% of re-ingestion, in the form of extra cooling. The results suggest that, re-ingested fluid from the upstream egress would prove highly beneficial to downstream stages and could reduce the negative impact of ingress.

8.1 How Can Engine Designers Benefit from the Results?

It was found that there is an asymmetry of circumferential effectiveness, upstream and downstream rotor platform, caused by the circumferential pressure distribution. And an intense mixing region occurred, due to the interaction between egress and mainstream. This finding can help engine designers choose better sealing flow rates, to minimise secondary losses, near the end-wall of the rotor disc. As the egress flow exits the seal clearance, it flows along the blade end-wall leading edge and across the blade passage. At the blade root leading edge, superfluous egress can produce aerodynamic losses. Furthermore, the results suggest a potential cooling benefit, on the rotor platform, but with added aerodynamic losses. These results inform engine designers that egress flow does not all bad news, it can provide great benefits if the sealing flow rate is optimised, in order to balance out the aerodynamic losses with cooling benefits.

Inflexions on the sealing effectiveness curves, occurred, over a critical sealing flow rate range, $0.03 < \Phi_0 < 0.08$, for two different stage geometries. At a non-dimensional sealing flow rate, 0.08, the equivalent sealing efficiency is approximately 92%, for a Reynolds number of the order 10^6. Commercial engines typically operate at an ideal sealing flow effectiveness of 95%. Furthermore, unsteady pressure data showed that flow structures exist within the critical sealing range. A distinctive frequency occurred within the critical range, at a non-dimensional sealing flow rate of 0.05, this sharp frequency and any inflexion disappeared, when the rotor blades were removed. A critical interaction between the blade and egress flow, is believed to be the cause of this distinct frequency, but the inflexions are believed to be a consequence of the flow structures. It is believed these flow structures also play a role in ingress. These findings inform engine designers that for a given blade profile, a critical sealing flow rate exists, where the sealing effectiveness is significantly reduced. This can help engine designers understand better, engine sealing efficiency, at non-ideal sealing flow rates.

Re-ingestion was experimentally measured and evaluated using a theoretical model. Re-ingestion of upstream egress flows across the blade passage and into the downstream wheel-space. Upstream egress has a relatively low temperature compared to the mainstream; therefore any levels re-ingestion would result in extra cooling to the downstream stages. Re-ingestion was evaluated for a range of sealing flow rates. For a sealing efficiency of 95%, approximately 33% of the upstream egress gets re-ingested. A typical gas turbine operates at a sealing flow effectiveness of 95%, therefore it is speculated that a real engine would also experience 33% of upstream egress re-ingestion. This finding informs engine designers, how much extra cooling they can expect from re-ingestion.

8.2 Future work

The experimental work conducted in a new 1.5-stage turbine rig has provided results that enhance the fundamental knowledge on ingestion in gas turbines. Although this study has answered many questions, some still remain unanswered, such as: what is the effect of introducing sealing flow at high radius in the wheel-space? And what effect does the degree of reaction have on ingress. The future work will aim to answer these important questions.

Effect of sealing flow at high radius

A typical gas turbine uses nozzle guide vanes to condition the flow. Flow leakage exists across the roots of these guide vanes. This problem is commonly known as, chordal hinge leakage flow. Leakage paths exist throughout the engine's architecture and they are impossible to prevent. The aim is to study ingress in the presence of leakage flow, at high radius, near the periphery of the wheel-space. Measurements of CO_2 gas concentration, static pressure and total pressure will be carried out. The Bath 1.5-stage turbine rig will be modified to introduce leakage flows through the stator disc. To the author's knowledge this study will be carried out for the first time in a 1.5-stage turbine rig. Two questions arise from this problem;

1) Are chordal hinge leakage flows detrimental to the efficiency of the turbine?
2) Can we use these leakage flows to our advantage?

The effect of degree of reaction on ingress

The degree of reaction of a turbine stage is the fraction of the fluid static enthalpy drop, which occurs across the stage. The degree of reaction is used as a design parameter since it gives an indication of the stage efficiency. It is envisioned to conduct unsteady and steady pressure measurements as well as CO_2 gas concentration measurements. The present thesis provides experimental data mainly from the upstream wheel-space; however, these future measurements will be conducted mainly in the downstream wheel-space. It is speculated that the downstream wheel-space will be affected the most by the degree of reaction. Two questions arise from this problem;

1) What effect will the degree of reaction have on ingress?
2) Does a change in degree of reaction improve or worsen the sealing effectiveness?

References

Adolf, M. 1939, The Combustion Gas Turbine: Its History, Developtment, and Prospects, Brown, Journal and Proceedings of the Institution of Mechanical Engineers, 197-222.

Abe, T., Kikuchi, J. and Takeuchi, H., 1979. “An Investigation of Turbine Disk Cooling (Experimental Investigation and Observation for Hot Gas Flow into a Wheel Space)”. CIMAG – 13th International Congress on Combustion Engines.

Alstom, 2007. “The World’s First Industrial Gas Turbine Set at Neuchatel (1939)”. ASME International Historic Mechanical Engineering Landmark, H135.

Batchelor, G.K., 1951, "Note on a Class of Solutions of the Navier-Stokes Equations Representing Steady Rotationally-Symmetric Flow", *The Quarterly Journal of Mechanics and Applied Mathematics*, 4(1), 29-41.

Bayley, F.J. and Owen, J.M., 1970, "The Fluid Dynamics of a Shrouded Disk System With a Radial Outflow of Coolant", *Journal of Engineering for Power*, 92(3), 335-341.

Beard, P.F., Chew, J.W., Gao, F. and Chana, K.S., 2016, "Unsteady Flow Phenomena in Turbine Rim Seals", *ASME Paper No. GT2016-56110*.

Bohn, D., Johann, E. and Kruger, U., 1995, "Experimental and Numarical Investigations of Aerodynamic Aspects of Hot Gas Ingestion in Rotor - Stator Systems with Superimposed Cooling Mass Flow", *ASME Paper 95-GT-143*.

Bohn, D., Rudzinski, B., Surken, N. and Gartner, W., 1999, "Influence of Rim Seal Geometry on Hot Gas Ingestion into the Upstream Cavity of an Axial Turbine Stage", *ASME Paper 99-GT-248*.

Bohn, D., Rudzinski, B., Surken, N. and Gartner, W., 2000, "Experimental and Numerical Investigation of the Influence of Rotor Blades on Hot Gas Ingestion Into the Upstream Cavity of an Axial Turbine Stage", *ASME Paper No. 2000-GT-0284*.

Bohn, D. and Wolff, M., 2003, "Improved Formulation to Determine Minimum Sealing Flow – Cw, min – for Different Sealing Configurations", *ASME Paper N0. GT2003-38465*.

Bohn, D.E., Decker, A., Ma, H. and Wolff, M., 2003, "Influence of Sealing Air Mass Flow on the Velocity Distribution in and Inside the Rim Seal of the Upstream Cavity of a 1.5-Stage Turbine", *ASME Paper 00-GT-284*.

Bohn, D.E., Decker, A., Chew , N. and Jakoby, R., 2006, "Influence of an Axial and Radial Rim Seal Geometry on Hot Gas Ingestion Into the Upstream Cavity of a 1.5-Stage Turbine", *ASME Paper No. GT2006-90453*.

Boudet, J., Autef, V.N.D., Chew, J.W. and Hills, N.J., 2006, "Numerical Simulations of Rim Seal Flows in Axial Turbines", *The Aeronautical journal No. 2915*.

Boudet, J., Chew, J.W. and Hills, N.J., 2006, "Numerical Simulation of the Flow Interaction Between Turbine Main Annulus and Disc Cavities", *ASME Paper No. GT-2006-90307*.

Chew, J. W., 1991. “A Theoretical Study of Ingress for Shrouded Rotating Disk Systems with Radial Outflow”. ASME *J. Turbomach.*, 113(1), pp. 91-97.

Chew, J.W., Green, T. and Turner, A.B., 1994, "Rim Seling of Rotor - Stator Wheelspaces in the Presence of External Flow", *ASME Paper 94-GT-126*.

Childs, P.R.N., 2011. *Rotating Flow.* Oxford: Butterworth-Heinemann.

Clark, K., Barringer, M. and Thole, K., 2016, "Using a Tracer Gas to Quantify Sealing Effectiveness for Engine Realistic Rim Seals", *ASME Paper No. GT-2016-58095*.

Dadkhah, S., Turner, A.B. and Chew, J.W., 1992, "Performance of Radial Clearance Rim Seals in Upstream and Downstream Rotor–Stator Wheelspaces", *Journal of Turbomachinery,* 114(2), 439-445.

Daniels, W.A., Johnson, B.V., Graber, D.J. and Martin, R.J., 1992, "Rim Seal Experiments and Analysis for Turbine Applications", *Journal of Turbomachinery,* 114(2), 426-432.

Dietrich Eckard, 2014, Gas Turbine Powerhouse: The Development of the Power Generation Gas Turbine at BBC-ABB -Alstom. Oldenbourgh Wissenschafts Verlag GmbH.

Eastwood, D., Core, D. D., Long, C. A., Atkins N. R., Childs, P. R. N., Scanlon, T. J. and Guijarro-Valencia, A., 2012. “Experimental Investigation of Turbine Stator Well Rim Seal, Re-Ingestion and Interstage Seal Flows Using Gas Concentration Techniques and Displacement Measurements”. ASME *J. Turbomach.,* 134, pp. 082501.

Feiereisen, J., Paolillo, R. & Wagner, J., 2000, “UTRC Turbine Rim Seal Ingestion and Platform Cooling Experiments,” AIAA Paper No. AIAA-2000-3371.

Friedunder, S., 1980, An Introduction to the Mathematical Theory of Geophysical Fluid Dynamics, Volume 41, North Holland Publishing Company

Gentilhomme, O., Chew, J.W., Hills, N.J. and Turner, A.B., 2003, "Measurement and Analysis of Ingestion Through a Turbine Rim Seal", *Journal of Turbomachinery,* 125(3), 505-512.

Graber, D.J., Daniels, W.A. and Johnson, B.V., 1987. *Disc Pumping Test.* Air Force Wright Aeronautical Laboratories, (Report No. AFWAL-TR-87-2050).

Green, T. and Turner, A.B., 1994, "Ingestion Into the Upstream Wheelspace of an Axial Turbine Stage", *Journal of Turbomachinery,* 116(2), 327-332.

Gregory, N., Stuart, J.T., Walker, W.S., 1955, On the Stability of Three-Dimensional Boundary Layers with Application to the Flow due to a Rotating Disc, Volume 248- Issue 943, The Royal Society.

Hills, N.J., Chew, J.W. and Turner, A.B., 2002, "Computational and Mathematical Modeling of Turbine Rim Seal Ingestion", *Journal of Turbomachinery*, 124(2), 306-315.

Hills, N.J., Green, T. and Turner, A.B., 1997, "Aerodynamics of Turbine Rim-Seal Ingestion", *ASME Paper No. 97-GT-268*.

Jakoby, R., Zierer, T., Lindblad, K., Larsson, J., deVito, L., Bohn, D.E., Funcke, J. and Decker, A., 2004, "Numerical Simulation of the Unsteady Flow Field in an Axial Gas Turbine Rim Seal Configuration", *ASME paper No. GT2004-53829*.

Owen, J.M., 2011a, "Prediction of Ingestion Through Turbine Rim Seals Part 1: Rotationally-Induced Ingress", *Journal of Turbomachinery, Vol-133/ 031005-1*.

Owen, J.M., 2011b, "Prediction of Ingestion Through Turbine Rim Seals Part 2: Externally-Induced and Combined Ingress", *Journal of Turbomachinery, Vol-133/ 031006-1*.

Owen, J.M., Kunyuan, Z., Pountney, O., Wilson, M. and Lock, G., 2010a, "Prediction of Ingress Through Turbine Rim Seals Part 1: Externally-Induced Ingress. ", *ASME Paper GT2010-23346*.

Owen, J.M. and Rogers, R.H., 1989. *Flow and Heat Transfer in Rotating-Disc Systems*. Taunton, Somerset, England: Research Studies Press Ltd.

Patinios, M., Scobie, J.A., Sangan, C.M., Owen, J.M. and Lock, G., 2016, "Measurements and Modelling of Ingress in a New 1.5-Stage Turbine Research Facility", *ASME Paper No. GT2016-57163*.

Phadke, U.P. and Owen, J.M., 1983. "The Effect of Geometry on the Performance of 'Air-Cooled' Rotor-Stator Seals," *International Council on Combustion Engines (CIMAC), 15th Congress.* Paris, pp. 335-360.

Phadke, U.P. and Owen, J.M., 1988a, "Aerodynamic Aspects of the Sealing of Gas-Turbine Rotor-Stator Systems: Part 1: The Behavior of Simple Shrouded Rotating-Disk Systems in a Quiescent Environment", *International Journal of Heat and Fluid Flow*, 9(2), 98-105.

Phadke, U.P. and Owen, J.M., 1988b, "Aerodynamic Aspects of the Sealing of Gas-Turbine Rotor-Stator Systems: Part 2: The Performance of Simple Seals in a Quasi-Axisymmetric External Flow", *International Journal of Heat and Fluid Flow*, 9(2), 106-112.

Phadke, U.P. and Owen, J.M., 1988c, "Aerodynamic Aspects of the Sealing of Gas-Turbine Rotor-Stator Systems: Part 3: The Effect of Nonaxisymmetric External Flow on Seal Performance", *International Journal of Heat and Fluid Flow*, 9(2), 113-117.

Picha, K. G. and Eckert E.R.G., 1958. “Study of the Air Flow between Coaxial Discs Rotating with Arbitrary Velocities in an Open or Closed Space”. *Proceedings of the 3rd U.S. National Congress of Applied Mechanics*, pp. 791-798.

Popovic, I., Hodson, H.P., 2013, "Improving Turbine Stage Efficiency and Sealing Effectiveness Through Modifications of the Rim Seal Geometry", *Journal of Turbomachinery, Vol-135/ 061016-1*.

Rabs, M., Benra, F.-K., Dohmen, H.J. and Schneider, O., 2009, "Investigation of Flow Instabilities Near the Rim Cavity of a 1.5-Stage Gas Turbine", *ASME Paper No. GT2009-59965*.

Roy, R.P., Paolillo, R.E., Feng, J. and Narzary, D., 2005, "Experiment on Gas Ingestion Through Axial-Flow Turbine Rim Seals", *Journal of Engineering for Gas Turbines and Power*, 127(3), 573-582.

Sangan, C.M., Pountney, O.J., Scobie, J.A., Wilson, M., Owen, J.M. and Lock, G.D., 2012, "Experimental Measurements of Ingestion Through Turbine Rim Seals-Part III: Single and Double Seals", *Journal of Turbomachinery-Transactions of the Asme*, 135(5), 051011.

Sangan, C.M., Zhou, K.Y., Owen, J.M., Pountney, O.J., Wilson, M. and Lock, G.D., 2012, "Experimental Measurements of Ingestion Through Turbine Rim Seals. Part 1: Externally-Induced Ingress", *ASME Journal of Turbomachinery*, 135, 021012.

Sangan, C.M., Pountney, O.J., Zhou, K.Y., Owen., Wilson, M., and Lock, G.D., 2013, "Experimental Measurements of Ingestion Through Turbine Rim Seals. Part 1I: Rotationally-Induced Ingress", *ASME Journal of Turbomachinery*, 135, 021013.

Schlichting, H, 1955, Boundary Layer Theory, 1st Edition, Pergamon Press.

Savov, S.S., Atkins, N.R. and Uchida, S., 2016, "Comparison of Single and Double Lip Rim Seal Geometry", *ASME paper No. GT2016-56317*.

Scobie, J.A., Teuber, R., Sheng Li, Y., Sangan, C.M., Wilson, M. and Lock, G.D., 2015, "Design of an Improved Turbine Rim-Seal", *Journal of Engineering for Gas Turbines and Power*, 138(2), 022503-022503.

Scobie, J.A., Hualca, F.P., Sangan, C.M. and Lock, G.D., 2017, "Egress Interaction Through Turbine Rim Seals", *ASME Paper No. GT2017-64632*.

Scobie, J., Hualca Tigsilema, F. P., Patinios, M., Sangan, C., Owen, J., & Lock, G. (2017). Re-Ingestion of Upstream Egress in a 1.5-Stage Gas Turbine Rig. *Journal of Engineering for Gas Turbines and Power: Transactions of the ASME*, *140*(7), [072507].

Soares, C. 2015, Gas Turbines: A Handbook of Air, Land and Sea Applications, Elsevier.

Stewartson, K., 1953, "On the Flow Between Two Rotating Coaxial Disks", *Mathematical Proceedings of the Cambridge Philosophical Society*, 49(02), 333-341.

Wang, C.-Z., Mathiyalagan, S.P., Johnson, B.V., Glahn, J.A. and Cloud, D.F., 2013, "Rim Seal Ingestion in a Turbine Stage From 360 Degree Time-Dependent Numerical Simulations", *Journal of Turbomachinery*, 136(3), 031007-031007.

Wang, C.-Z., Jong, F., Johnson, B.V. and Vashist, T.K., 2007, "Comparison of Flow Characteristics in Axial-Gap Seals for Close- and Wide Spaced Turbine Stages", *ASME Paper GT2007-27909*.

Zhou, D.W., Roy, R.P., Wang, C.Z. and Glahn, J.A., 2010, "Main Gas Ingestion in a Turbine Stage for Three Rim Cavity Configurations", *Journal of Turbomachinery*, 133(3), 031023.